

**IMPACT & PENETRATION STUDIES: SIMPLIFIED MODELS
AND MATERIALS DESIGN FROM AB INITIO METHODS**

A Ph.D. Thesis
Presented to
The Academic Faculty

by

Tianci Jiang

In Partial Fulfillment of the
Requirements for the Degree
Doctor of Philosophy
In the School of Aerospace Engineering

Georgia Institute of Technology
Atlanta, Georgia 30332
May 2006

Copyright © 2006 by Tianci Jiang

**IMPACT & PENETRATION STUDIES: SIMPLIFIED MODELS
AND MATERIALS DESIGN FROM AB INITIO METHODS**

Approved by:

Dr. Sathya V. Hanagud, Advisor
School of Aerospace Engineering
Georgia Institute of Technology

Dr. Xia Lu
School of Aerospace Engineering
Georgia Institute of Technology

Dr. Massimo Ruzzene
School of Aerospace Engineering
Georgia Institute of Technology

Dr. George Kardomateas
School of Aerospace Engineering
Georgia Institute of Technology

Dr. George Simitzes
School of Aerospace Engineering
Georgia Institute of Technology

Dr. Ravindra Annigeri
Lead Engineer
General Electric, Inc.

Date Approved: Jan 13, 2006

ACKNOWLEDGEMENTS

I would like to express my sincere gratitude to Dr. Sathya V. Hanagud, my thesis advisor, for his close guidance during my Ph.D. study at Georgia Tech, and his reviewing and correcting my entire thesis manuscript. I would like to express my deep appreciation to Dr. George Kardomateas, my previous advisor during my Master study at Georgia Tech, for many inspiring discussions and encouragement, as well as for the knowledge that he shared with me during my years at Georgia Tech. If I could have a chance to extend my career in research, I wish I could become an excellent professor like him. Specially, I would like to express my deep appreciation to Dr. Xia Lu, for her day-by-day reviewing my research progress and day-by-day encouragement, which impel and help me to overcome countless difficulties during my Ph.D. study. She is like a mirror in front of me, by which I can examine myself and overcome shortcomings. I would like to thank Dr. George Simitzes for his many highly valuable suggestions and recommendations on my thesis direction and improvements. I would like to thank Dr. Massimo Ruzzene and Dr. Ravindra Annigeri for their time in serving on my thesis committee and providing many highly valuable suggestions to improve the thesis.

In the recent years, I have been also working in General Electric, Inc, simultaneously. I would like to express my heartfelt respect to the chairman of Aerospace Engineering department, Dr. Jeff Jagoda, for his great attention to my Ph.D. study and his

help on complicated policies related to registration and tuition waiver while I was co-operating with GE.

I would like to express my deep appreciation to Debbie Harper who, prior to March 2005, was the international advisor at Georgia Tech. She never hesitated to take the time to help me sort through the complicated policies related to my registration and visa situation.

From August 2001 to present, I have been working at General Electric Inc. During these years, Mr. Bob Johnston has been my manager and Mr. Ted Fisher has been my team leader. Looking back over the past years, it is very difficult to count how many times Bob and Ted helped me out of all kinds of trouble (e.g. financial support, tuition reimbursement, working authorization, security background check, time needed for qualifying exam, proposal, defense, etc.). This kind support has been deeply hidden in my heart and impels me to be a diligent person, a responsible person, a noble-minded person. The most important thing is, from their rigorous work approach, I have learned how to respect my career. At this moment, I would like to express my deep respect and appreciation to Bob and Ted.

I would like to show my heartfelt gratitude to Mr. Thomas Freeman, the technical leader of F-class and Contractual Services in GE application engineering group, for his precious time to edit and correct my manuscript. And I also want to express my deep appreciation to Thomas Freeman, Anastasia Harris, Emily Hu and Renhua Wang, my co-workers, for their great encouragement when I totally lost hope and confidence.

I also want to thank my dear friends, Ying Yang, Derek Reding, Zhibo Wu, Dr. Xiaolan Song, and Leslie Tong for sharing their knowledge with me and morally supporting me through the years.

I am very grateful for my dear mother, Prof. Jinwen An, who is a well-known professor in the area of automatic flight control at Northwestern Polytechnical University in China. I am very grateful for her love, her moral support through the years and her inspiring discussions related to my Ph.D. study.

Finally, I wish to express my deepest affection and memories of my dear father, Prof. Guanglun Jiang, who was also an excellent professor in the area of automatic flight control and the Dean of the graduate school at the Northwestern Polytechnical University in China. At this moment, while greatly missing my dearest father, for his voice and face, I am very proud to fulfill a cherished desire of my parents to become the third Ph.D. from Georgia Tech in the family.

TABLE OF CONTENTS

ACKNOWLEDGEMENTS	iii
LIST OF TABLES	x
LIST OF FIGURES	xii
SUMMARY	xvii
CHAPTER 1 INTRODUCTION	1
CHAPTER 2 BACKGROUND	4
2.1 Penetration Mechanics	4
2.1.1 Impact & Penetration	4
2.1.2 Erosion Mechanisms	7
2.1.3 Penetration Models	9
2.2 Alloys	21
2.2.1 Analysis of Alloys	26
2.2.2 EOS for Steels and Alloys	37
2.3 Ab Initio Methods	41
2.3.1 Schrödinger Equation and Wave Function	41
2.3.2 Born-Oppenheimer Approximation	42
2.3.3 Density Functional Theory [Kohn & Sham--1965]	42
2.3.4 Approximations in the Density Functional Theory	43
2.4 Studies of Iron from First Principles	47

2.5	Scope of the Thesis	53
CHAPTER 3 OBJECTIVES & THESIS TASKS		55
3.1	Reduced Models for Studies of High-Velocity Impact and Penetration	55
3.2	Material Characterization of Projectile Materials from First Principles	56
CHAPTER 4 REDUCED MODELS FOR PENETRATION MECHANICS		58
4.1	Hypothesis and Conservation Equations	60
4.1.1	Hypothesis of Sequence of Events Leading to Nose Erosion	61
4.2	1-D Impact and Penetration Problem	63
4.2.1	Formulation of 1-D problem with varying cross section area	63
4.2.2	Reduced Model with Changing Cross-Section Area in the Nose Region	68
CHAPTER 5 EOS, MAGNETISM AND PHASE TRANSITION FOR IRON		82
5.1	Material Characterization by using Ab Initio Methods	83
5.1.1	Ab initio EOS for a Crystalline Solid	83
5.1.2	Phase transitions & EOS	86
5.2	Approximations & Convergences in Ab Initio Methods	87
5.3	Results & Discussions	91
5.3.1	Studies of Bcc, Fcc, Hcp Iron and Their Magnetic Phases	91
5.3.2	Phase Transitions for Iron	113
5.3.3	Equation of State for Iron	115
5.3.4	Discussions	116
CHAPTER 6 EOS AND MAGNETIC PROPERTIES FOR STEEL ALLOYS		121
6.1	Binary Alloy $Fe_{1-x}Ni_x$ by Using the SQS Method	122
6.2	Interstitial Disordered Ternary Alloy $Fe_{1-x-y}Ni_xC_y$	129

6.3	Approximations & Convergences	132
6.4	EOS and Magnetic Properties	134
6.4.1	Binary Alloy $\text{Fe}_{1-x}\text{Ni}_x$	135
6.4.2	Ternary Alloy $\text{Fe}_{1-x-y}\text{Ni}_x\text{C}_y$	140
6.4.3	EOS of Binary Alloy $\text{Fe}_{1-x}\text{Ni}_x$ and Ternary Alloy $\text{Fe}_{1-x-y}\text{Ni}_x\text{C}_y$	140
6.4.4	Thermodynamical EOS for the Binary Alloy $\text{Fe}_{1-x}\text{Ni}_x$ and the Ternary Alloy $\text{Fe}_{1-x-y}\text{Ni}_x\text{C}_y$	142
6.4.5	Effects of Nickel and Carbon as Constituents	145
CHAPTER 7 CONCLUSION & FUTURE WORK		147
7.1	Conclusions	147
7.2	Future Work	148
CHAPTER 8 APPENDIX		149
8.1	Ising Models	149
8.1.1	1-D Ising Model	149
8.1.2	2-D square lattice – Bethe’s approximation	154
8.1.3	3-D Ising Model – Simple Cubic Lattice	155
8.2	Procedures to Construct the Substitutional Disordered Alloy	157
8.2.1	Genstr	157
8.2.2	Corrdump	160
8.2.3	Gensqs	163
8.3	Procedures For Cold Curve Calculation By Using VASP	165
8.3.1	For Iron calculations	165
8.3.2	For $\text{Fe}_{14}\text{Ni}_2$ calculations	166

8.3.3	For $\text{Fe}_{14}\text{Ni}_2\text{C}_1$ calculations	167
8.4	Procedures For Lattice Thermal Calculation By Using PHONON	169
8.4.1	Steps for the PHONON calculations	169
	REFERENCES	175
	VITA	189

LIST OF TABLES

Table 2-1. Chemical composition(mass%).	24
Table 5-1. Energy comparison based on KPOINT at the fixed setting ENCUT=267.907ev, EDIFF=E-07 & EDIFFG=E-06 (PW91_PAW).	88
Table 5-2. Energy comparison based on KPOINT at the fixed setting ENCUT=267.907ev, EDIFF=E-04 & EDIFFG=E-03 (PW91_PAW).	89
Table 5-3. Parameters used in the calculations.	90
Table 5-4. The summary of the investigations on approximations.	99
Table 6-1. Correlation functions of a random binary alloy A_xB_{1-x} with $x = 0.125$.	123
Table 6-2. Pair correlation functions of four SQS-8 structures. (The numbers inside of the brackets [] indicate the degeneracy factors of the corresponding figures).	126
Table 6-3. Pair correlation functions for five SQS-16 structures.	127
Table 6-4. Ideal SQS-16 structure for alloy $Fe_{1-x}Ni_x$.	127
Table 6-5. Equilibrium SQS-16 structure for $Fe_{1-x}Ni_x$ with NM order, relaxed by using PBE and PAW.	128
Table 6-6. Predicted densities for $Fe_{1-x}Ni_x$ ($x = 0.125$).	128
Table 6-7. Parallelograms and O-sites in the SQS-16 structure of $Fe_{1-x}Ni_x$ with $x = 0.125$.	131
Table 6-8. Relaxed supercell $Fe_{14}Ni_2C_1$ of NM order.	132
Table 6-9. Accuracy and convergence comparison to EDIFF & EDIFFG at KPOINT=6 & ENCUT=400.	134
Table 6-10. NM accuracy and convergence comparison for ENCUT at KPOINT=6 and EDIFF= 10^{-4} & EDIFFG= 10^{-3} .	134
Table 6-11. NM accuracy and convergence test for KPOINT at ENCUT=450ev and EDIFF= 10^{-4} & EDIFFG= 10^{-3} .	134
Table 8-1. Probabilities of appearance of configurations of a bond [Kikuchi--1951].	150

LIST OF FIGURES

Figure 1-1. Nose erosion of the 20.3 mm diameter, 4340 Rc 45 projectiles striking into concrete targets, and deviation of penetration by Jerome et al. 2000 [Jerome--2000].	2
Figure 2-1. Centerline velocities versus time [Walker—1995].	6
Figure 2-2. On the penetration velocity dependence of the L/D effect [Mont--1976].	8
Figure 2-3. Deformation of the rod and target shortly after impact [Tate--1986].	9
Figure 2-4. Hardness Contours after punching into annealed copper [Bishop—1945].	10
Figure 2-5. Dynamic cavity expansion problem for a locking elastic-plastic material [Hanagud--1971].	12
Figure 2-6. Idealized stress-strain curves for a locking elastic-plastic material [Hanagud--1971].	12
Figure 2-7. Comparison between results of deep penetration theories and experimental data [Hanagud--1971].	12
Figure 2-8. Simple Theoretical Model of Flat-ended projectile fired at speed U at flat target [Taylor--1947].	14
Figure 2-9. The geometry relation of the deceleration rate and plastic wave propagation rate [Walker--1995].	18
Figure 2-10. Axial velocity profile along projectile/target centerline obtained from numerical simulation [Walker--1995].	19
Figure 2-11. Comparison of penetration (nose) and tail velocities vs. depth of penetration from numerical [Walker--1995].	20
Figure 2-12. Binary alloy. (a). Substitutional; (b). Interstitial.	22
Figure 2-13. Order and Disorder.	23
Figure 2-14. Fictitious spin variables are assigned.	29
Figure 2-15. Figures (pairs, triplets and quadratics) in a two dimensional lattice.	30

Figure 2-16. PAW method and its decomposition.	46
Figure 2-17. Plane waves and PAWs.	46
Figure 2-18. Total energy/atom and magnetic moment of NM, FM and AFM phases of bcc and fcc iron [Wang--1985].	50
Figure 2-19. GGA pressure-volume relations for bcc (dashed line), fcc (dotted line) and hcp (solid line).	52
Figure 2-20. Calculated GGA and LDA pressure-volume relations for hcp Fe compared with room-temperature static compression data of [Mao--1990].	52
Figure 4-1. The projectile impacts and penetrates into the target.	59
Figure 4-2. Nose erosion mechanisms.	61
Figure 4-3. Schematic view of a differential element in Eulerian coordinate system.	64
Figure 4-4. Schematic view of a differential element (Δx) in Eulerian coordinate system.	65
Figure 4-5. 1D model of changing cross-section area in the nose region during the initial stages of penetration (lock density is constant ρ_l).	71
Figure 4-6. Shock wave front. Left side is elastic wave; right side is plastic wave. c_p is the plastic wave propagation speed.	75
Figure 4-7. Time variations of the penetration velocity $v_A(t)$ for the steel projectile into aluminum target.	77
Figure 4-8. Time variations of the penetration velocity $v_A(t)$ for tungsten projectile into steel target.	77
Figure 4-9. Time variations of the penetration velocity $v_A(t)$ for steel projectile into ($Mg_{0.92}, Fe_{0.08}$) SiO_3 Perovskite target.	80
Figure 4-10. The time variations of the phase transition profile for steel projectile into ($Mg_{0.92}, Fe_{0.08}$) SiO_3 Perovskite target. (a) Mass fraction of phase 2 as a function of x & t ; (b) Time variations of mass fraction of phase 2 at locations $x=x_A$ & $x_A - 0.5mm$; and (c) Profile of mass fraction of phase 2 at $t = 0.055$ and $12 \mu s$.	81
Figure 5-1. Bcc conventional unit cell and magnetic orientation [001]. CUC=Conventional Unit Cell.	92
Figure 5-2. Ground state energies of bcc iron vs. density (by PBE with PAW).	93
Figure 5-3. Magnitude of the magnetic moments of bcc iron vs. density (by PBE with PAW).	93

Figure 5-4. Ground state energies of bcc iron vs. density (by PW91 with PAW).	96
Figure 5-5. Magnitude of the magnetic moments of bcc iron vs. density (by PW91 with PAW).	96
Figure 5-6. Ground state energies of bcc iron vs. density (by PW91 with PAW and Hubbard_U [U=4.5 & J=1]).	97
Figure 5-7. Magnitude of the magnetic moments of bcc iron vs. density (by PW91 with PAW and Hubbard_U [U=4.5 & J=1]).	97
Figure 5-8. Ground state energies and magnetic moments at T=0K for bcc FM iron at various U (Hubbard_U).	98
Figure 5-9. Collinear magnetic orders in [001] for fcc iron.	100
Figure 5-10. Ground state energies of fcc iron vs. density (by PBE with PAW).	103
Figure 5-11. Magnitude of the magnetic moments of fcc iron vs. density (by PBE with PAW and Hubbard_U [U=4.5 & J=1]).	103
Figure 5-12. Ground state energies of fcc iron vs. density (by PW91 with PAW).	104
Figure 5-13. Magnitude of the magnetic moments of fcc iron vs. density (by PW91 with PAW).	104
Figure 5-14. Ground state energies of fcc iron vs. density (by PW91 with PAW and Hubbard_U [U=4.5 & J=1]).	105
Figure 5-15. Magnitude of the magnetic moments of fcc iron vs. density (by PW91 with PAW and Hubbard_U [U=4.5 & J=1]).	105
Figure 5-16. NM Hcp lattice structure (A/B/A/B).	106
Figure 5-17. FM hcp and AFM hcp lattice structures and magnetic orders.	106
Figure 5-18. Ground state energies of hcp iron vs. density (by PBE with PAW).	107
Figure 5-19. Magnetic moments of hcp iron vs. density (by PBE with PAW).	107
Figure 5-20. Ground state energies of hcp iron vs. density (by PW91 with PAW).	110
Figure 5-21. Magnetic moments of hcp iron vs. density (by PW91 with PAW).	110
Figure 5-22. Ground state energies of hcp iron vs. density (by PW91 with PAW and Hubbard_U [U=4.5 & J=1]).	111
Figure 5-23. Magnitude of the magnetic moments of hcp iron vs. density (by PW91 with PAW and Hubbard_U [U=4.5 & J=1]).	111

Figure 5-24. Ground state energies and magnetic moments at T=0K for hcp FM iron at various U (Hubbard_U).	112
Figure 5-25. Phase diagram of iron [Jephcoat-1986].	113
Figure 5-26. Phase Transition from Bcc FM to Hcp NM.	114
Figure 5-27. EOS of iron with phase transitions from bcc FM to hcp NM at P = 9.8 GPa and comparison with experimental data [Jonathan et al. 1997].	115
Figure 5-28. Energy comparison of bcc FM, fcc AFM, and hcp NM (by PBE and PAW).	118
Figure 5-29. Energy comparison of bcc FM, fcc AFM, and hcp NM (by PW91 and PAW).	119
Figure 5-30. Energy comparison of bcc FM, fcc AFM, and hcp NM (by PW91 and PAW with U=4.5 and J=1).	120
Figure 5-31. EOS of iron with phase transitions from bcc FM to hcp NM at P = 9.8 GPa and comparison with experimental data [Jonathan et al. 1997].	120
Figure 6-1. The errors of all the structures of N=16 atoms per unit cell and with x = 0.125.	126
Figure 6-2. O-sites in the bcc conventional unit cell.	129
Figure 6-3. O-site in the bcc primitive unit cell.	129
Figure 6-4. (a) Ground state energies of bcc Fe _{1-x} Ni _x vs. density (by PBE with PAW). (b) Ground state energies of bcc Fe _{1-x} Ni _x vs. pressure (by PBE with PAW).	136
Figure 6-5. Magnetic moment of bcc Fe _{1-x} Ni _x vs. density (by PBE with PAW).	137
Figure 6-6. Ground state energies of bcc Fe _{1-x} Ni _x vs. density (by PW91 with PAW).	138
Figure 6-7. Magnetic moment of bcc Fe _{1-x} Ni _x vs. density (by PW91 with PAW).	138
Figure 6-8. Ground state energies of bcc Fe _{1-x-y} Ni _x C _y vs. density (by PBE with PAW).	139
Figure 6-9. Ground state energies of bcc Fe _{1-x-y} Ni _x C _y vs. density (by PW91 with PAW).	139
Figure 6-10. EOS of bcc Fe, Fe _{1-x} Ni _x and Fe _{1-x-y} Ni _x C _y vs. relative volume (by PW91 with PAW).	141
Figure 6-11. EOS calculated (at T=0K) vs. experimental data [Biswajit--2005].	142
Figure 6-12. EOS for the binary alloy Fe _{1-x} Ni _x at T=0K and T=300K.	144
Figure 6-13. EOS for the ternary alloy Fe _{1-x-y} Ni _x C _y at T=0K and T=300K.	145

Figure 6-14. Magnetic moments of bcc Fe and $\text{Fe}_{1-x}\text{Ni}_x$ vs. relative volume (by PBE with PAW & PW91 with PAW).	146
Figure 8-1. An ensemble of linear lattices [Kikuchi--1951].	149
Figure 8-2. An intermediate stage of constructing a linear Ising Lattice [Kikuchi--1951].	151
Figure 8-3. spin selection tree(1)	152
Figure 8-4. spin selection tree(2).	153
Figure 8-5. 2-D Ising Model [Kikuchi--1951].	154
Figure 8-6. An intermediate stage of constructing a simple cubic lattice [Kikuchi--1951].	155
Figure 8-7. Procedures to construct the substitutional disordered alloy.	157
Figure 8-8. An input file named "Lat.in".	158
Figure 8-9. Ising-like model. A & B are atom species.	158
Figure 8-10. Procedures and pseudocode of <i>genstr</i> .	159
Figure 8-11. str_A.out to provide the atom information for structure A.	160
Figure 8-12. Procedures and Pseudocode of <i>Corrdump</i> .	161
Figure 8-13. The file Torr.out obtained from <i>Corrdump</i> .	161
Figure 8-14. The file Clusters.out from <i>Corrdump</i> .	162
Figure 8-15. Special quasirandom structure is generated by <i>Gensqs</i> .	163
Figure 8-16. All correlation functions from <i>Corrdump</i> on these structures with the desired figure of Clusters.out.	164
Figure 8-17. Substitutional Disordered Binary Alloy $\text{Fe}_{1-x}\text{Ni}_x$ (x=12.5%).	165
Figure 8-18. Input files and output files for VASP calculations.	165
Figure 8-19. Procedure for PHONON calculation and interaction with VASP [Parlinski-2004].	169

SUMMARY

Many engineers and scientists have studied the impact and penetration mechanics of high-speed metallic projectiles into hard targets. Most studies on penetration mechanics were mainly concentrated on the determination of the ballistic limit, the penetration depth, the time variation of the penetration velocity and the target resistance. The studies have also identified many physical properties of the projectile materials that play important roles in penetration mechanics. These mechanical properties of projectile materials that are very often made of steel alloys, are currently obtained from experiments. To design new alloys that can provide the desired penetration characteristics, it is necessary to understand the thermomechanical properties of the alloys as functions of the constituents of the alloy, defects and heat treatments. However, most of the experiments that are needed to determine the mechanical properties at high strain rates require equipment like a gas gun. Tests and the instrumentation are expensive and time intensive. An alternate procedure, to understand the thermo-mechanical properties and design new alloys for projectiles, is to use ab initio methods. However, most current ab initio research on physical properties of the materials is concentrated on determining the equation of state (EOS), magnetic properties of simple crystal structures. The physical property studies like the EOS of disordered alloys are rather underdeveloped. It is because extensive density functional theory (DFT) calculations are needed to consider a large number of the configurations of the alloys. The

characterization of the physical properties of the alloys is an open research area in physics, engineering and materials science.

Need for additional research that is related to impact and penetration mechanics was also emphasized by results of recent impact and penetration mechanical tests. In these tests, steel projectiles were impacted into targets like concrete, with projectiles made of high strength steel (AISI 4340 steel alloys with appropriate heat treatment) and striking velocities (or the velocities prior to impact) in the range of 1200 to 1500 meters per second. Results indicated a material removal from the nose of the projectile, phase changes of the projectile materials, a reduction in the length of the projectile, and a blunting of the nose shape. Moreover, a significant deviation of the penetration path from its intended path was observed in some cases. These observations cannot be explained by current theories and numerical integration code that are used to study impact and penetration mechanics.

Thus, the objectives of the thesis research are to (a) formulate and characterize the mechanisms responsible for the material erosion of the impacting projectile and the mass loss from the nose region; and (b) to determine the physical properties of alloy steels that are important to penetration mechanics from ab initio methods. The results can be used to design new projectile materials that can provide the desired penetration characteristics.

These objectives are accomplished by investigating two related problems. The first problem is to formulate simplified models that can explain the penetration mechanics. Usually theoretical impact and penetration studies require the integration of nonlinear partial differential equation that represents finite deformation elastic-plastic behavior of materials. The simple models that are formulated do not require numerical integration of

a set of partial differential equations. The new models include changes of yield stress behind the shock wave and high strain rate phase transitions. Nose erosion effects, and time-dependent penetration path can be determined by integrating ordinary differential equations. The simplified one-dimensional model, with varying cross sectional area in the nose region, are formulated to include a conical nose shape of the projectile, finite deformations, increasing yield stress behind the shock front and high strain rate phase transition. A cavity-locking expansion theory model is used to obtain the target resistance that is responsible slowing and deforming the penetrating projectile.

The second problem concerns the determination of the constitutive relations from ab initio methods where only information from the periodic table is used. The equation of state and magnetic moments for alloy steels are investigated by using a special quasirandom technique and ab initio methods. Specifically, equations of state for an interstitial disordered alloy $\text{Fe}_{1-x-y}\text{Ni}_x\text{C}_y$ is developed. The alloy constituents include some of the constituents of AISI4340. First, the equation of state of iron and phase transition of iron are studied and validated with available analytical results and experiments. Then, other alloying elements are considered to investigate the disordered alloy. The challenge is to develop constitutive equation for the disordered alloy with interstitial alloying element of carbon and the substitutional alloying elements of iron and nickel, with very low concentrations of nickel and carbon. These investigations will form foundation for future work involving new projectile with steel nose and shank made of multifunctional structural energetic materials.

CHAPTER 1

INTRODUCTION

During the past few years, several impact and penetration tests have been conducted, with striking velocities in the range of 1200 to 1500 meters per second [Jerome—2000, Martineau—2004]. Steel projectiles were impacted into selected concrete targets. At these striking velocities, impact and penetration of high strength steel projectiles into concrete targets resulted in a significant mass loss of the projectile from the nose region, a reduction in length of the projectile, observable changes of the nose shape of the projectile, and a deposition of melted steel on the nose and shank of the projectile. In the basic studies of the projectile, it has been found that the nose shape can have a significant effect in penetration mechanics [Wilkins—1978, Hill—1980, Batra—1987 & Walker--1995]. Similarly, the change in length of the projectile can have an effect on the penetration efficiency [Aöler—1984 & Charks--1995]. Even when the impact was normal to the surface, the trajectory of the projectile, through the target, deviated from the intended straight trajectory (Figure 1), in some cases.

Thus it can be inferred that changes in the nose shape due to thermomechanical deformation alters the magnitude and the direction of the resulting force due to the target resistance. This can cause both projectile failures and a deviation of the projectile path deviation from the intended path. With increasing striking velocities (up to 2500 – 3000 m/sec), the nose erosion will become more important. The nose erosion can also change force acting on the shank of the projectile. For an improved performance, it is necessary

to understand the thermomechanical deformation in penetration mechanics and design projectiles that are penetration resistant. Thus, it is necessary to design alloys that are penetration resistant. One option is to design these alloys from first principles – ab initio methods.

To design erosion resistant projectiles from first principles, it is necessary to develop methods that can be used to determine the physical properties of alloys that can be used in the nose of the projectiles. Equation of state of the alloy steel is a part of constitutive equation that is important in the high-velocity impact and penetration studies. Other important characteristics are the thermomechanical that are phase transition.

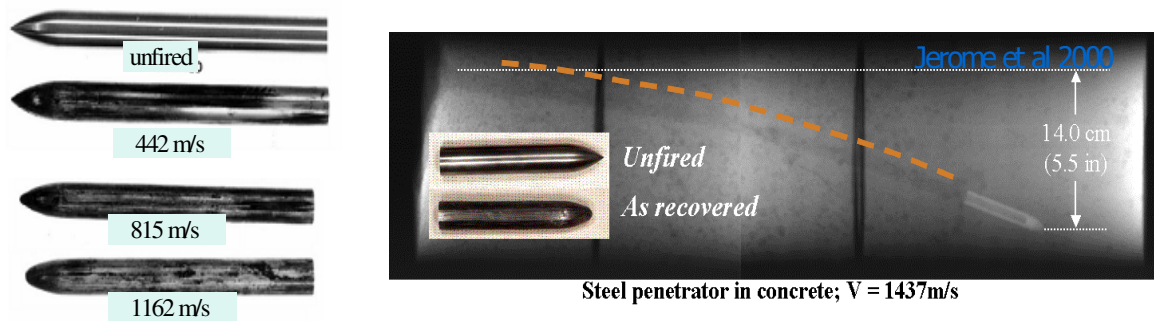


Figure 1-1. Nose erosion of the 20.3 mm diameter, 4340 Rc 45 projectiles striking into concrete targets, and deviation of penetration by Jerome et al. 2000 [Jerome--2000].

Thus, the first goal of this study is to understand the penetration mechanisms responsible for the nose erosion of a kinetic energy projectile at high striking velocities, and develop theoretical models for impact and penetration that can be used to study penetration events, with nose erosions; A second goal is to characterize the thermomechanical properties of the penetrator materials from first principles. Such a procedure can be used to design erosion resistant alloys. Solutions to these problems will

form foundation to design a new class of projectile with an erosion resistant nose and a shank that can be made of dual functional energetic material motivation.

CHAPTER 2

BACKGROUND

2.1 Penetration Mechanics

The penetration mechanics, also known as the impact and penetration mechanics, is an interdisciplinary subject. A comprehensive discussion of the relevant background would be quite extensive. However, studies in this thesis focus on the nose erosion scenario, which occurs during a short duration after impact. Therefore, the relevant issues are discussed in this chapter.

2.1.1 Impact & Penetration

Since Taylor discussed his impact tests [Taylor-1947] and derived a simplified analytical model, penetration mechanics has been extended in many different directions. The main research areas are focused on the ballistic limit, the penetration depth, the threshold of penetration velocity, the erosion of the projectile, the target resistance forces and the plastic flow in projectile and the target. Eichelberger and Gehring [Eichelberger--1962] and Christman and Gehring [Christman—1966] suggested that impact and penetration process involves four phases. These phases are identified as Transient, Primary, Secondary and Recovery phases. The transient phase is a short duration phase after impact. Elastic and plastic waves are generated right after impact, in the projectile and target. In this phase, waves propagate in the projectile and have not yet reached the

rear end of projectile. The next phase identified, as the primary phase of the penetration process, corresponds to the quasi-steady-state penetration. In this phase, the elastic wave has reflected many times from the rear end of the projectile and the elastic-plastic interface. The third phase that is some times identified as the secondary phase of the penetration process occurs after the projectile has been completely deformed or has essentially lost most of its kinetic energy. The fourth phase or “After-flow”, called by Pack and Evans [Pack—1951], is also known by the term “secondary penetration” for the extra penetration when a dense rod projectile penetrated a less dense target. The final recovery phase of the penetration process is estimated to be small for most armor materials [Tate—1986].

Nose Shape Effects: It has long been known that the nose shape can have a significant influence on the projectile performance while penetrating into targets. In 1978 Wilkins [Wilkins—1978] presented the types of target failures for thin plates that depended on nose shape of the projectile. Hill [Hill--1980] in 1980 showed that the resistant force for certain types of “smooth” ogives was independent of the nose shape, but nose shape was directly related to the critical velocity for cavitation. He also showed that the resistant force, affecting the penetration and the extent of cavitation were both sensitive to the nose shape. Batra [Batra--1987] showed that the nose shape had a significant effect on the deformation of the target material around the interface between the projectile and the target. The axial resistance forces were found to be higher for a blunt nose, compared to the ellipsoidal nose. Walker [Walker--1995] used a numerical integration program known as the wavecode CTH to numerically investigate the initial transient behavior of three different nose shapes: a blunt nose, a hemispherical nose and a

conical nose of angle 45°. Largest differences, at the initial impact stage, were the high pressures in the target, with the projectile that had a blunt nose shape. The larger pressure with the blunt nose shape changes the material flow zone in the target.

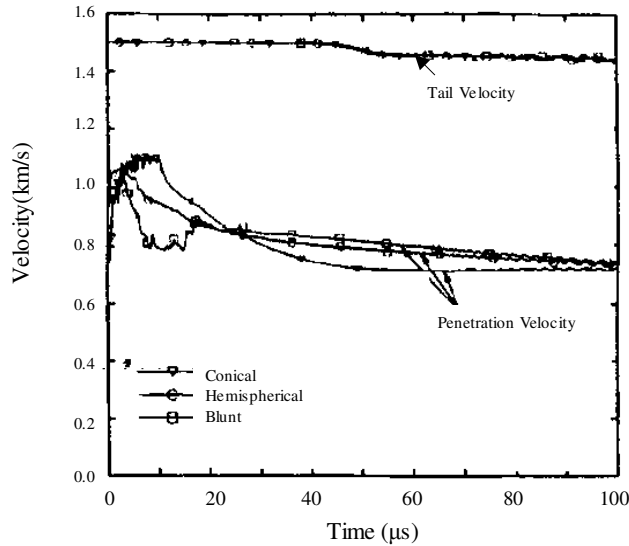


Figure 2-1. Centerline velocities versus time [Walker—1995].

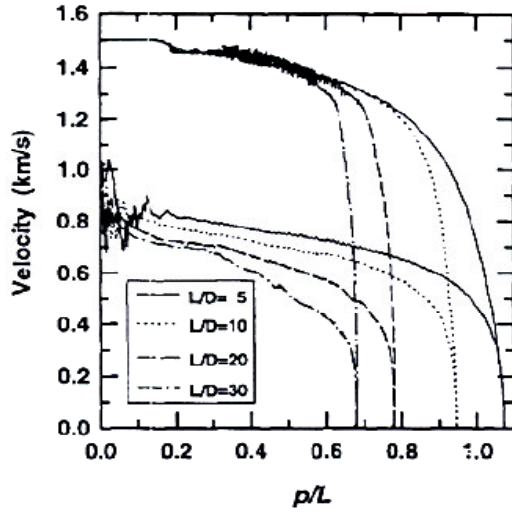
L/D effects: One of the measurements of the penetration efficiency is δ/L , where δ is the depth of penetration into a semi-infinite target and L is the original length of the projectile. L/D ratio (where D is the diameter of the projectile) has a significant effect on the penetration efficiency. In general, L/D effect is examined at different ranges of striking velocities. In classification the striking velocity, the range of 1.0-1.8km/s is called as the ordnance velocity [Charles--1995]. From the 1960s to the mid of 1990s, studies concerned with L/D were concentrated in the range of ratios of 1 to 10. Hohler and Stilp [Hohler--1984] considered the ratio of 32. However, the explanation for the cause of the higher L/D effect was not provided. In a parallel research, to supplement L/D effect in Tate's model, which is mainly based on a modified hydrodynamic theory,

Anderson and Walker [Charles--1995][Charles--1996], in 1995 and 1996, used numerical integration to study the L/D effects at different ranges of velocity from 1.8km/s to 4.5km/s. They suggested that at ordnance velocities, the L/D effect mainly depended on a decay of the penetration velocity in the steady-state stages (primary phase). At higher velocities, no L/D effect is seen in the steady-state region and the L/D effect was mainly important in the terminal transient phase of non-eroding rod penetration.

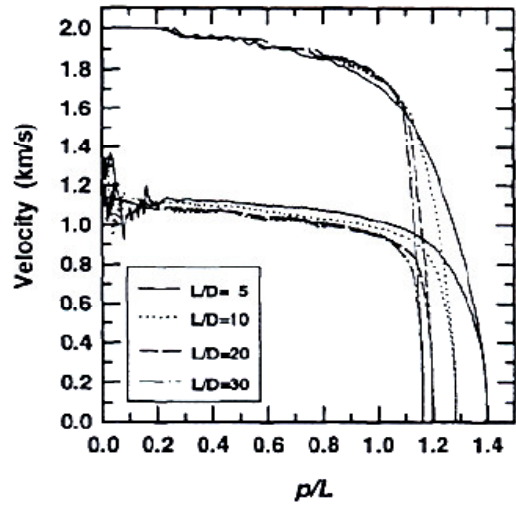
The Figure 2-2 displays that at the ordnance velocities 1-1.9km/s, L/D plays an important role in the steady-state and terminal transient phases.

2.1.2 Erosion Mechanisms

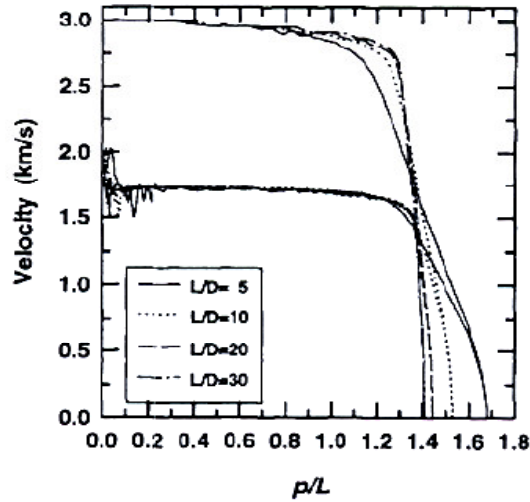
Erosion has long been studied as an important research area in penetration mechanics. Various empirical models that are based on friction were proposed. Montgomery [Mont--1976] presented test results on the wear of projectile rotating bands in gun tubes. One of his conclusions was that the melting of the surface of the projectile was responsible for the observed abrasion or wear of the projectile.



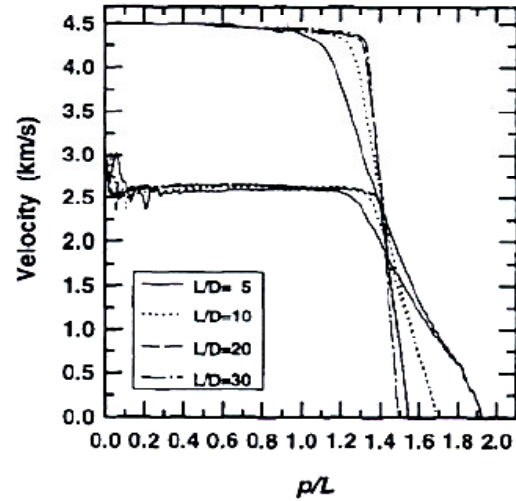
(a). Penetration and tail velocities versus depth of penetration: 1.5km/s



(b). Penetration and tail velocities versus depth of penetration: 2km/s



(c). Penetration and tail velocities versus depth of penetration: 3km/s



(d). Penetration and tail velocities versus depth of penetration: 4.5km/s

Figure 2-2. On the penetration velocity dependence of the L/D effect [Mont--1976].

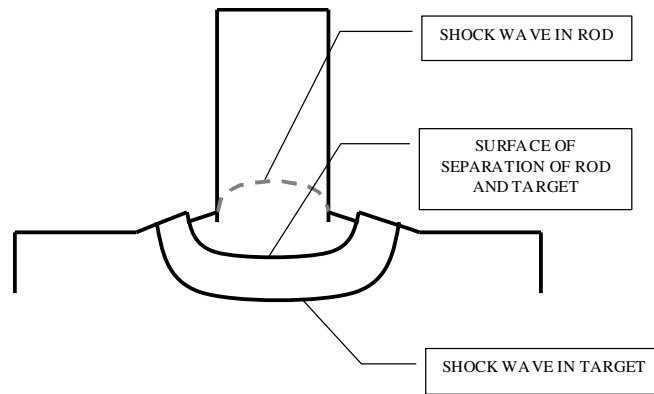


Figure 2-3. Deformation of the rod and target shortly after impact [Tate--1986].

2.1.3 Penetration Models

Currently, many impact and penetration studies use computer codes that integrate partial differential equations. The computer programs are known as “hydrocodes”. Many simplified models have been developed to understand the fundamental mechanisms of impact and penetration. These simplified models are developed on the basis of certain assumptions and thus avoid the use of “hydrocode”. Some of those models are discussed in this section.

2.1.3.1 Cavity Expansion Theory

One of the early studies of deep penetration problem is based on the theoretical studies of Bishop, Hill and Mott [Bishop--1945] in the 1940s for the quasistatic punch indentation process. In this work, solutions to the static expansion of cylindrical and spherical cavities in an infinite medium were sought. Experiments verified the work showing that the load will not increase to a maximum value until the base of the cone has penetrated into the copper block about 4-5 times the diameter of the projectile [Bishop--

1945]. The load is recorded as P_0A , where P_0 is found to be 5 times the yield stress “ P_s ” under quasi-static punch and A is the area of the cross-section of the punch. Bishop developed a theoretical model to calculate P_c and P_s that are required to enlarge a cylindrical or a spherical hole in any strain hardening material.

Following Bishop’s theory, Hill and Hopkins [Hopkins--1960] developed a dynamic cavity-expansion model for an incompressible elastic-plastic target material and a rigid projectile. In this study, it was assumed that cavities are formed in solids due to high explosive charges, and a large amount of plastic deformations accompanied by shock waves occur near the cavity surface. In 1980s, Hill [Hill—1980] summarized some of his work conducted at Fort Halstead during the Second World War. He applied the dynamic cavity expansion theory to investigate rigid projectiles penetrating into selected deformable armors. The dynamic cavity-expansion equations were derived and developed, by making the following assumptions [Bishop—1945]:

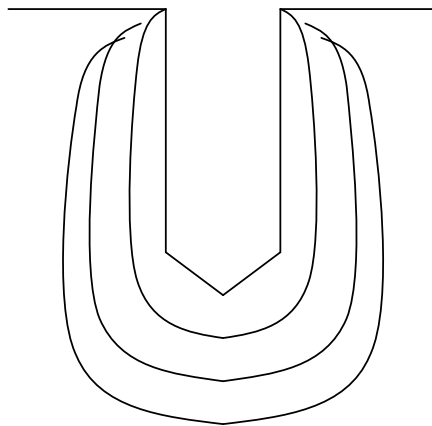


Figure 2-4. Hardness Contours after punching into annealed copper [Bishop—1945].

- The motion is spherically-symmetric;
- The motion of a Gas bubble followed by shock waves is uniform and adiabatic;

- The target material is incompressible and obeys (a) Hooke's law, (b) Tresca's yield condition and ideal plasticity.

Goodier [Goodier --- 1964] applied Hopkins' dynamic cavity expansion theory to penetration problems of a hypervelocity impact and resulting penetration into a semi-infinite target. Goodier also introduced strain hardening effects in the target. However, when Goodier's results were applied to the study the penetration of steel projectiles into targets of aluminum alloys, the curve of penetration depth versus impact velocity was always above the experimental data. This indicated that the penetration resistance was underestimated. Hanagud and Ross [Hanagud--1971] investigated the causes for the underestimation of penetration resistance and relaxed the assumption of incompressibility in Goodier's study concerning the target material, both in elastic and plastic regions. They developed a cavity-locking expansion theory (Figure 2-5), based on spherical locking waves [Hanagud--1966]. The theory introduced the target compressibility through an idealized locking approximation to modify the finite deformation theory of Goodier. They determined the appropriate locking densities (Figure 2-6) through a consideration of the Hugoniot curves for the target materials. This theory showed that the curve of the penetration depth versus the impact velocity agreed more accurately with the experimental data (Figure 2-7). In all these studies [Hill, Hopkins, Goodier, Hanagud & Ross], the projectile was always considered to be rigid.

In 1988, Forrestal also developed an analytical model for the elastic-plastic response of a compressible material for the target under the assumption of a spherically symmetric cavity.

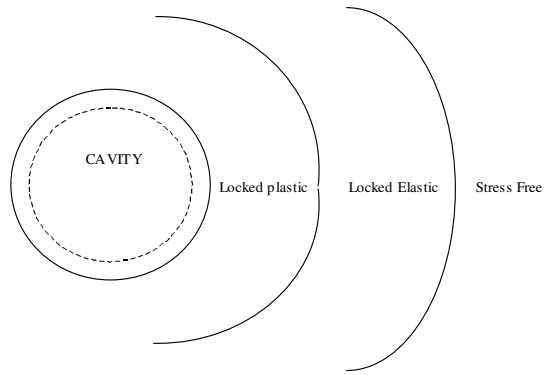


Figure 2-5. Dynamic cavity expansion problem for a locking elastic-plastic material [Hanagud--1971].

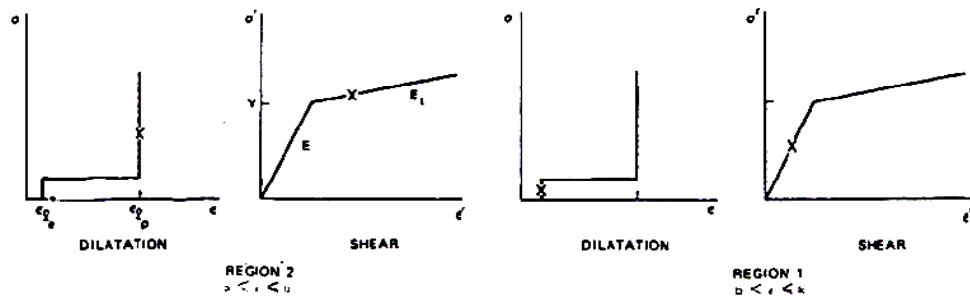


Figure 2-6. Idealized stress-strain curves for a locking elastic-plastic material [Hanagud--1971].

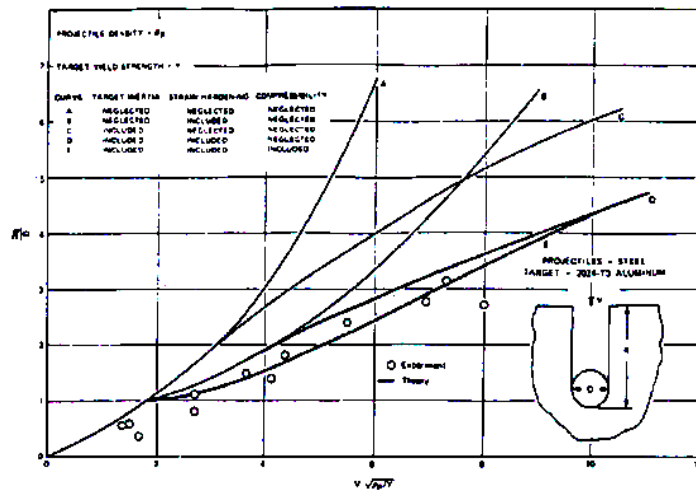


Figure 2-7. Comparison between results of deep penetration theories and experimental data [Hanagud--1971].

2.1.3.2 Time-Dependent Penetration Models and Deformable Projectiles

Deformable projectiles: Starting from Taylor's model for impact in 1947 to determine the dynamic yield stresses of the projectiles, many simplified models have been proposed. In 1967, Tate [Tate--1967] proposed his modified hydrodynamic model to solve the steady-state penetration problem. Tate incorporated the strength factors R_t and Y_p into the model, where R_t is the target yield strength and Y_p is the projectile yield strength. Later in 1986, Tate estimated R_t from a spherical cavity expansion theory. Roseberg [Roseberg--1990] contributed an expression for R_t from the expansion of a cylindrical cavity in an infinite medium in his paper of 1990. In 1988 Forrestal [Forrestal--1988] and Longcope determined the quasi-static pressure R_t , where R_t is the pressure required to open a spherical cavity from zero initial radius in a ceramic target material. Wright [Wright--1983] and Pidsley [Pidsley--1984] pointed out that there are some limitations in the modified Bernoulli model.

In 1995, Walker and Anderson [Walker--1995] assumed a velocity profile in the target on the basis of results from the numerical simulations and integrated in the linear momentum balance equation about the central line. Walker and Anderson [Walker--1995] determined the penetration path. This model provided a good approximation to the entire penetration process for a blunt cylindrical projectile with elastic and ideal plastic behavior. No other nose shape is considered.

Other developments are the Ravid-Bodner models [Ravid--1983] for penetration of projectiles in metallic plates that are currently used in the ballistics community. The Ravid-Bodner model uses the upper bound theorem of plasticity theory with modifications to include dynamic effects. They assumed flow fields in their penetration

model for different regions of the target. Their model considers a finite-thickness of the metallic target. Failure modes in Ravid-Bodner model are used to determine the perforation of targets. Some numerical simulations show that the projectile continues to erode for a few microseconds after target failure [Ravid—1983]. Chocron and Anderson [Chocron—2003] combine the Walker-Arderson and Ravid-Bodner models and formulated a “blended model” to solve multiple-plate penetration problems. In a related work, Walker used an energy-rate balance equation to predict depth of penetration [Walker—2001].

2.1.3.2.1 Equations of Taylor’s Impact Model for Projectile Deformation

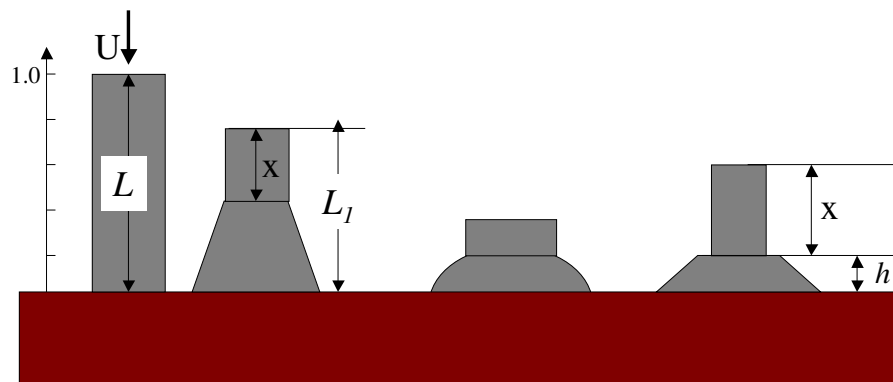


Figure 2-8. Simple Theoretical Model of Flat-ended projectile fired at speed U at flat target [Taylor--1947].

In this section, some details of the deformable projectile models are discussed. Taylor [Taylor--1947] discussed a simple model in his paper to theoretically determine dynamic yield stress of projectile materials. In Figure 2-8, a cylindrical specimen made of a metal is assumed to impact a rigid target. The original length of the specimen is assumed to be L . When the specimen strikes the target at a velocity U , the stress at the impact end is assumed to reach immediately the elastic limit. Following the impact, an elastic compression wave is generated and travels along the rod towards to the rear end. If

the material behaves like an elastic-plastic material, a plastic wave is generated. At a given location, the plastic wave encounters the reflected elastic tension wave. In the region where plastic wave has traveled, the length is (L-x); the variable x represents the length of the portion that has not been plastically compressed. The low case v is used to denote the particle velocity in the plastic region. At the moment when the reflected elastic wave has just reached the plastic boundary, the velocity of material in elastic area is $U - 2S/\rho c$, where S is the yield stress of the material, ρ is the density, and c is the longitudinal elastic wave propagation velocity, but it is stress free. It is similar to a new specimen with striking velocity $U - 2S/\rho c$ instead of U. Of course, the length has changed to a shorter length. Based on the description, Taylor formulated the basic differential relations:

$$\begin{aligned}\frac{dh}{dt} &= v \\ \frac{dx}{dt} &= -(u + v) \\ \frac{du}{dt} &= -\frac{2S}{2x\rho} = -\frac{S}{x\rho}\end{aligned}\tag{2.1.3-1}$$

where (Figure 2-8) h is the distance of the plastic boundary from the target, u is the velocity of the rear end of projectile, the v is the interface velocity of elastic-plastic of projectile. It is obvious that the number of equations in (2.1.3-1) is not enough to determine the variables h, v, x and u. Taylor suggested a simplified model that is shown in Figure 2-8. He also gave a set of equations to simply the penetration model. Besides (2.1.3-1), additional two equations were added with an additional unknown A.

Continuity equation

$$A_0(u + v) = Av\tag{2.1.3-2}$$

Momentum equation

$$\rho A_0 (u + v)u = S(A - A_0) \quad (2.1.3-3)$$

Taylor's simplified the 1-D impact model and found a procedure to determine the dynamic yield stress. However, his model needed improvements for many practical applications. For example, he assumed that the plastic-elastic boundary moved along the rod at a uniform velocity from the impact end, and the target to be a rigid body. Possible phase transition that may result from plastic work is not considered in the model. There are many studies that have followed Taylor's work to improve the Taylor's studies with deformable projectile. Most of these studies are primarily focused on identifying dynamic yield stress.

2.1.3.2.2 *Equation of Tate's penetration model for Projectile Deformation*

Tate [Tate--1967] developed a model for a deformable long-rod penetration by using a hydrodynamic approximation. Prior to this work, most penetration mechanics models assumed rigid projectiles. The projectile and the target were both treated as fluids with some modifications. The Bernoulli Equation was modified to consider the yield strengths of the projectile and the target. The modified hydrodynamic theory was introduced to penetration mechanics. In his paper, Tate explained penetration mechanism from the point of view of the shock wave propagation and the hydrodynamic phase. This analysis can be regarded as the steady-state phase in the penetration process. He modified the Bernoulli's equation to include the strength of the target and the projectile:

$$\frac{1}{2} \rho_t u^2 + R_t = \frac{1}{2} \rho_p (v - u)^2 + Y_p \quad (2.1.3-4)$$

In this equation, R_t is the target resistance in the one-dimensional formulation, Y_p is the projectile strength, ρ_t is the target density, ρ_p is the projectile density, v is the penetration velocity, and u is the impact velocity.

$$Y_p = -\rho_p l \frac{dv}{dt} \quad (a)$$

$$\frac{dl}{dt} = -(v-u) \quad (b)$$
(2.1.3-5)

The deceleration rate and the erosion rate of the projectile are discussed on the basis of the values of Y_p and R_t . Here (2.1.3-5a) is used to denote the deceleration rate, and (2.1.3-5b) is used to denote the erosion rate of the original length L of the projectile. For the case $Y_p < R_t$, a critical velocity is given by $[2(R_t - Y_p)/\rho_p]^{1/2}$. For the impact velocity below this value, the projectile will not stop eroding until it comes to rest. For the case $Y_p > R_t$, another critical velocity is given by $[2(Y_p - R_t)/\rho_p]^{1/2}$ and the erosion will not occur for the impact velocity below this value. In other words, the projectile will behave like a rigid body for impact velocity below this value.

Tate [Tate--1967] suggested that a plastic region exists in the projectile and only the length of elastic region of the projectile should be counted in the evolution of the deceleration of the rear end of the projectile. According to Walker, Tate's model predicts that the rear of the projectile decelerates too late and too rapidly at the very end of penetration [Walker--1995]; the projectile is nearly fully eroded in his prediction [Tate--1967]. In 1995, Walker [Walker--1995] presented his penetration model based on a velocity profile assumed on the basis of results of selected numerical simulations.

2.1.3.2.3 Walker's model for Projectile Deformation

Walker made several assumptions:

The target and the projectile are both considered to be axisymmetric. The projectile is a circular cylinder without a blunt nose. A velocity profile is assumed along the centerline from the rear end of the projectile to the infinite distance into the target. The back end of the projectile is decelerated by elastic waves. The elastic wave has reached the rear end of the projectile and reflected off the rear end. Also the elastic wave reflects off the plastic zone.

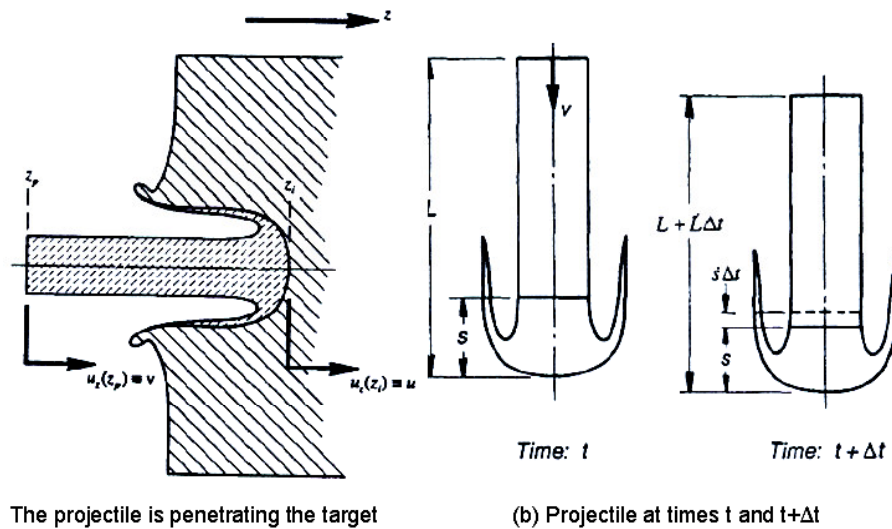


Figure 2-9. The geometry relation of the deceleration rate and plastic wave propagation rate [Walker--1995].

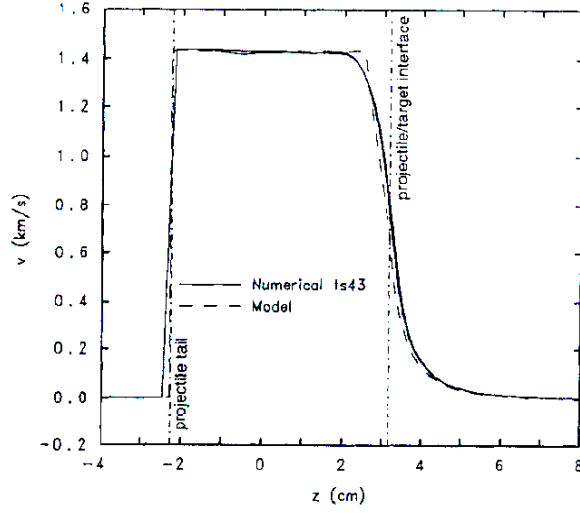


Figure 2-10. Axial velocity profile along projectile/target centerline obtained from numerical simulation [Walker--1995].

Walker assumed a particle velocity profile along the penetration path as follows:

$$u_z(z) = \begin{cases} u - \frac{v-u}{s}(z-z_i) & (z_i - s) \leq z < z_i \\ v & z_p \leq z < (z_i - s) \end{cases} \quad (2.1.3-6)$$

The z-direction Eulerian momentum equation is

$$\rho \left(\frac{\partial u_z}{\partial t} + u_x \frac{\partial u_z}{\partial x} + u_y \frac{\partial u_z}{\partial y} + u_z \frac{\partial u_z}{\partial z} \right) = \frac{\partial \sigma_{xz}}{\partial x} + \frac{\partial \sigma_{yz}}{\partial y} + \frac{\partial \sigma_{zz}}{\partial z} \quad (2.1.3-7)$$

Integrating equation (2.1.3-7) along the central line from the rear end of the projectile to an infinite distance into the target,

$$\rho_p \int_{z_p}^{z_i} \frac{\partial u_z}{\partial t} dz + \rho_t \int_{z_i}^{\infty} \frac{\partial u_z}{\partial t} dz + \frac{1}{2} \rho_p (u^2 - v^2) - \frac{1}{2} \rho_t u^2 - 2 \int_{z_p}^{\infty} \frac{\partial \sigma_{xz}}{\partial x} dz = 0 \quad (2.1.3-8)$$

In the equation (2.1.3-8), stress distributions for both the projectile and the target and velocity profile in the target are needed. The projectile is assumed to have two zones,

elastic and plastic. The stress in elastic zone is considered to obey Hooke's law and the plastic model is assumed to be perfect plastic. The velocity in the target is assumed to be obtained from the curl of a vector potential. Walker obtained the penetration velocity history which has a reasonable agreement with experimental results and numerical simulations.

For application to impact and penetration of steel projectiles into concrete or rock targets, at high striking velocities, several modifications of the Walker's model are needed. Improvements should consider the effect of the nose shapes, possible heating of the projectiles due to plastic work, possible phase changes, changes of yield stress behind the shock wave and the mechanisms of conversion of plastic work into heat.

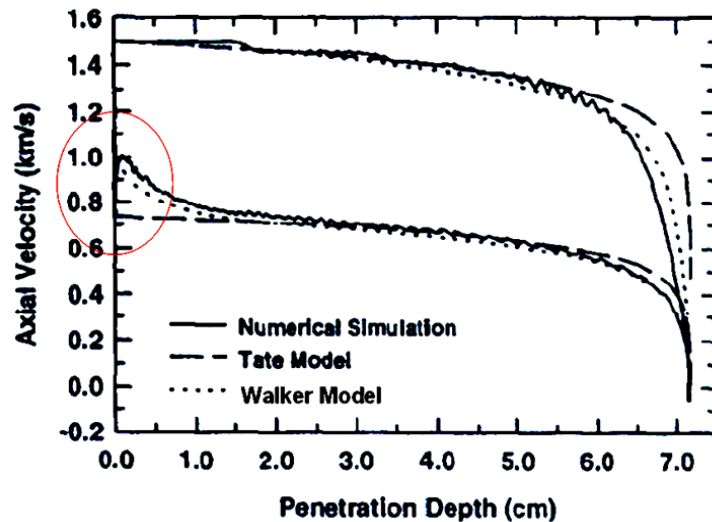


Figure 2-11. Comparison of penetration (nose) and tail velocities vs. depth of penetration from numerical [Walker--1995].

2.2 Alloys

As discussed in this chapter, the mechanical properties of the projectile and the target play important roles in the penetration mechanics and penetration performance. The deformation and erosion of the projectile depends on the projectile material. For an improved performance, an appropriate projectile material is needed. Currently most of the projectile materials are made of alloys. An alloy that is common is steel. To design an alloy, it is necessary to understand the constitutive equations, including phase transitions as a function of the different elements and the concentration of elements in the alloy.

An alloy is usually defined as any combination of two or more elements. Alloys have metallic properties. An alloy with two components is called a binary alloy, A_xB_{1-x} , one with three is a ternary alloy, $A_xB_yC_{1-x-y}$. Based on their combination, alloys can be divided into two basic types: solution and compound.

In Chemistry, a homogeneous mixture of at least one substance (solute) dissolved in another substance (solvent) is called solution. When a solute is dissolved into a solvent, the atoms or molecules of solute are surrounded by the atoms or molecules of the solvent. As the result, a structure is formed. In alloy, the host is like the solvent, which should have dominant occupation in the lattice and the lattice structure will perform like the host. The atoms of the solute gets into the lattice of the host and the lattice structure of the host will still be kept as one of the lattice structures which the host may have. In a microscopic analysis, it can be seen that some atoms of the solute occupy the positions of the atoms of the host and substitute the atoms of the host. The alloy produced in this way is called substitutional alloy (Figure 2-12-a). If the two metal atoms are of almost the

same size and the same crystallographic structure, then they may form a solid solution, such as Brass. Some atoms of the solute stay at the interstitial positions of the lattice of the host. The alloy produced in this way is called an interstitial alloy (Figure 2-12-b).

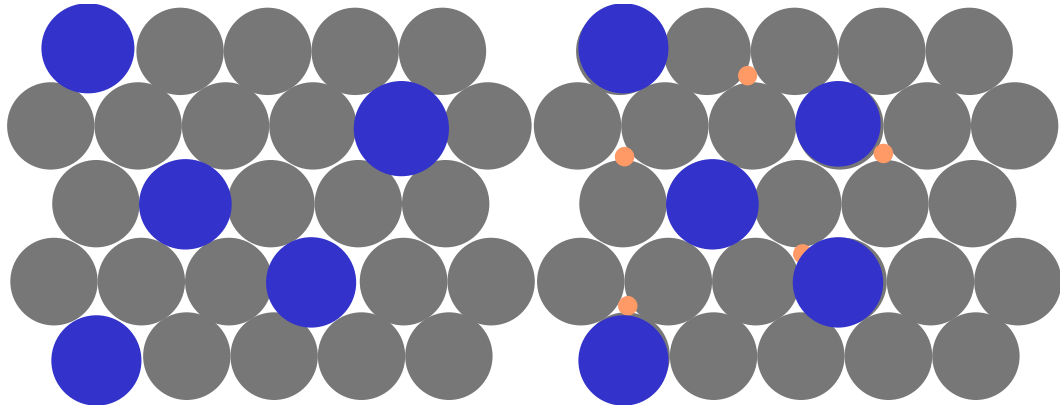
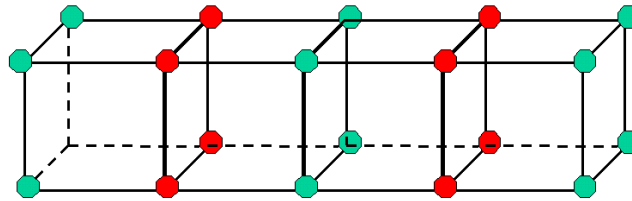


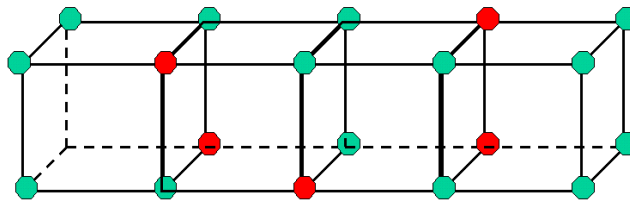
Figure 2-12. Binary alloy. (a). Substitutional; (b). Interstitial.

In contrast, a compound is a type of chemical substance formed by a chemical reaction. There is a fixed ratio that determines the composition. Such a fixed ratio, unlike an alloy, cannot be arbitrarily selected, instead. For example, sodium chloride (NaCl) with fixed ratio of composition everywhere is considered to be an ionic compound.

Alloys can be ordered or disordered. A compound is a perfectly ordered structure, while random alloys are disordered structures. Ordered structures, like crystals, usually have unit cells that can be repeated periodically along the lattice vectors. The disordered structures do not have the spacial periodicity. See the Figure 2-13. The order can be short-ranged or long-ranged. A definition of correlation for “figures” or “configurations” is used to characterize the order of structure. A figure or configuration is a type of the atom arrangement patterns that can be determined from the Ising Models.



(a). Ordered Structure



(b). Disordered Structure

Figure 2-13. Order and Disorder.

Steels are ferrous alloys, which consist of iron as the host constituent. There are many types of steels. Some examples are as follows.

Carbon steels:

- *Low Carbon Steel (<0.2%C):* Compared to other carbon steel, low carbon steel contains less carbon and is easier to cold-work because of their soft and ductile nature. Such as AISI1015, AISI1018 and AISI1020 etc.

- *Medium Carbon Steel (0.2%C~0.5%C):* A medium carbon steel has more carbon percentage compared to low carbon steel and can be heat treated to have a good balance of ductility and strength, like AISI1541~1552, etc.

- *High Carbon Steel (>0.5%):* When more percentage carbon is added in, the nature of the carbon steel would become more strong and brittle, such as AISI1561~1572.

Alloy steels: Regarded as the combination of two or more metals in addition to low percentage carbon, alloy steel may have many types due to different metals and proportions of the constituents. For example, the following table gives the concentration lists of some alloy steel [Nakajima--2003].

Table 2-1. Chemical composition(mass%)

Element	C	Si	Mn	P	S	Cu	Ni	Cr	Mo	Fe
AISI1345	0.43-0.48	0.15-0.3	1.6-1.9	0.035	0.04					
AISI3140	0.4-0.5		0.5-0.8				1.0-1.5	0.45-0.75		
AISI4340	0.38	0.30	0.76	0.018	0.014	0.08	1.72	0.75	0.15	Bal.

Stainless steels: Stainless steel was developed as the alloy that resists corrosion by the addition of chromium to iron. Over the years, it has been found that after the addition of other elements such as nickel, titanium, other particular characteristics of the alloys could be improved.

In this thesis, alloy steels, which can be used in the projectiles for high-velocity impact and penetration, will be studied. The physical properties, EOS (Equation of State), and associated magnetic properties, will be investigated on these alloys. The objective is to systematically study the effects of other components on the host material iron. We will start with two mostly used components: Ni and C. Specifically, we are interested in a disordered ternary alloy $Fe_{1-x-y}Ni_xC_y$. We consider a host disordered binary alloy of $Fe_{1-x}Ni_x$ [Ramos—2003 & A.Van De Walle--2002] with C as interstitial impurity, which is used to simulate steel in the application of impact and penetration.

As listed in Table-1, alloy steels like AISI4340 have Ni as the major second metal species. So we would like first to select it to investigate. Fe-Ni alloys have caught many attentions due to their properties. The structure of Fe_xNi_{1-x} can be classified into three

types. In the Ni-rich alloy (Fe concentrations <60 at. %), the system has a fcc structure and is ferromagnetic. These alloys have properties of nearly zero thermal expansion, called Invar alloys [ASM Specialty Handbook]. For iron concentrations between 60 and 80 at. %, the alloy's average magnetic moment decreases drastically. There is a structural phase transition from fcc to bcc. For Fe concentrations above 80 at. %, the system is ferromagnetic and bcc.

Most experimental and theoretical studies focus on the first and second categories. However, for steel alloys of high strength that are used in high-velocity impact and penetration, the Ni concentrations are low (e.g. AISI4340 Ni 1.72 wt. %). Therefore, in this thesis, the third category of Fe-Ni alloys, which has bcc structure and are ferromagnetic are considered.

Carbon is one of the most important constituents in the steel. Carbon may be substitutional or interstitial impurity [Venezuela--2004]. In recent papers, systematic ab initio theoretical investigations of the carbon impurity properties in the binary alloy system $A_{1-x}B_x$ are presented. In 2004, Venezuela [Venezuela--2004] investigated the carbon impurity in a Si_xGe_{1-x} alloy with $x=0.5$ and $x=0.85$. He concluded that the interstitial carbon has important contributions to the properties, because carbon migrates in Si in those interstitial sites. Related to this research area, deep level transient spectroscopy is used to show that proton and electron irradiation may generate interstitial impurities in the binary alloy Si_xGe_{1-x} [Monakhov—1997, Leevad—1999 & Larsen--2001]. As an improvement, Venezuela claimed that the local configuration of interstitial carbon atoms with pure Si atoms at their nearest neighborhood in Si_xGe_{1-x} , is the most favorable. It was shown that for higher concentration of Si, at the nearest-neighbor sites

of the carbon impurity, the formation energies are lower for both substitutional and interstitial carbon cases. This conclusion will be applied to the alloy $\text{Fe}_{1-x-y}\text{Ni}_x\text{C}_y$.

EOS for steels is very important in their applications in high-velocity impact and penetration. Traditionally, EOS is obtained by experimental measurements. However, due to a large span of design parameters, theoretical prediction in EOS for steels will be very beneficial in designing new materials (alloys) by addition and distribution of other materials for projectiles. The systematic investigations on the effects of design parameters, like species and their concentrations, will eventually lead to ab initio based procedures to design alloys with erosion resistance. The theoretical prediction on EOS of steels, in the published literature, is not complete because of a large number of alloying elements in steels and difficulties of theoretical modeling of disordered steel systems with a wide range of variations of concentrations of various species. It is necessary to systematically investigate this subject. For example, one can first introduce Ni and C, two most commonly used species in materials used in steel projectiles, $\text{Fe}_x\text{Ni}_{1-x}$ and $\text{Fe}_{1-x-y}\text{Ni}_x\text{C}_y$. The regular EOS and phase transition characteristics, from first principles, are not available for these alloys.

2.2.1 Analysis of Alloys

2.2.1.1 Mean Field Approach

The early work on modeling steel, by first principles for disordered alloys, is based on the mean field approach. The general idea of the mean field approach is to replace the

random distribution of the atoms by their average occupations of lattice sites. The idea comes from the statistical mechanics. The representative approach is the coherent potential approximation (CPA) [Gyorffy—1972, Mookerjee—1993, Raze—1990~1993, Johnson--1987]. The main idea is to represent the average occupations of lattice sites occupied by all atoms by the weighted combination of individual average occupations of A atoms and B atoms. Such a total average occupation can be thought as a configuration. This approach is applied to substitutional disordered binary system $A_{1-x}B_x$ to describe the average occupation. It is also used in Screened Korringa-Kohn-Rostoker [Raze—1990~1993] (SKKR) or the Tight-Binding Linearized Muffin-Tin Muffin-Tin Orbital (TB-LMTO) method. The limitation of the mean field approach is due to the use of only averages. The effect of the local environments around the atoms is not accurately considered. In reality, the local environments will definitely affect many characteristics, such as the interaction and the charge transfer. Such significant effects are found in some experimental observations [Mikkelsen--1982].

2.2.1.2 Direct Sampling Method

An alternative method to analyze disordered alloys is to use a statistical ensemble over all the possible configurations or simplified ensembles over a simplified set of representations of the structure.

First consider a binary substitutional alloy $A_{1-x}B_x$. If there are N atoms occupying at the N sites, then the possible different atomic arrangements will be 2^N . Each possible atomic arrangement is called a configuration, marked as σ . Each configuration σ has its own physical properties, such as total energy, band gap, etc. Such properties can be

denoted by $E(\sigma)$. Statistically, the measurable property $\langle E \rangle$ that represents the ensemble average over all configurations has the expression:

$$\langle E \rangle = \sum_{\sigma=1}^{2^N} \rho(\sigma) E(\sigma) \quad (2.2.1-1)$$

In this equation, $\rho(\sigma)$ is the weight function to count the probability of finding σ in an ensemble of systems. Assuming spatial ergodicity, all possible finite environments are realized in a sample as $N \rightarrow \infty$. In practical computations, only a small value of N is used. Even for a finite value of N , 2^N configurations lead to a very large number. It involves a large number of different configurations (e.g. 10^6 in Monte Carlo [Muller—2001 & Ozolins-1998]) or large cell sizes (10^3 atoms [Ozolins—1998, Wolverton—1995, Silverman—1995, Lake—1992]).

2.2.1.3 *Cluster Expansions*

Substitutional A/B systems, in solid state, are described by the occupation of A and B atoms, at the sites of a crystal lattice, in different patterns. These include $A_{1-x}B_x$ random alloys. In theoretical approaches, scientists seek ground state configurations or finite temperature thermodynamic averages of such systems. In principle, this requires a sampling of 2^N possible configurations when N lattice sites are considered, theoretically, $N \rightarrow \infty$. In practice, a large value N is considered. When more than two atoms A and B are considered, the challenge is to find methods that can sample such a large number. As is well known, today, quantum-mechanical total energy calculations increase rapidly with the number of atoms in the unit cell. Thus, the recent calculations, very often, are limited to few assumed crystal structures that are selected by intuition as “expected likely

configurations” (ELC) for the stable ground state. By plotting the total energy versus volume of the configuration, one selects a possible ground state among these ELCs. Most of the current research is to seek more accurate and systematic approach to obtain accurate ground state and finite temperature thermodynamic average by considering as few configurations as possible.

In further discussions, we assume that N is finite. Different configurations are denoted by “ σ ”. Then, fictitious spin variables are assigned to each of the possible N sites as \hat{S}_i , $\hat{S}_i = +1$ if it is occupied by B and $\hat{S}_i = -1$ if it is occupied by A [Wei & Zunger--1990].

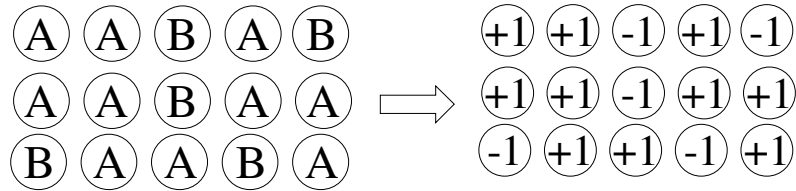


Figure 2-14. Fictitious spin variables are assigned.

For each configuration “ σ ” the total energy (electronic and nuclear) is denoted by $E_{\text{direct}}(\sigma) = E_d(\sigma)$. It is assumed that $E_d(\sigma)$ can be mapped into an Ising-like series [Wei & Zunger--1990].

$$E_d \approx E_{CE} = J_0 + \sum_i J_i \hat{S}_i(\sigma) + \sum_{j < i} \sum_i J_{ij} \hat{S}_i(\sigma) \hat{S}_j(\sigma) \quad (2.2.1-2)$$

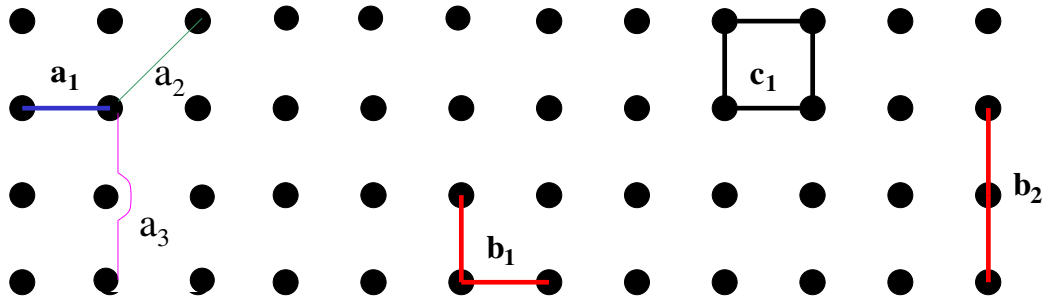


Figure 2-15. . Figures (pairs, triplets and quadratics) in a two dimensional lattice.

The quantities J are defined as “interaction energies”. The first term on right of the above equation is over all lattice sites. The second term is over all pairs of sites. The third is over all triplets. Similarly higher order terms in the series can be defined. Each one of these is defined as the basic “figures” of the considered lattice. In a two dimensional lattice a_1, a_2 and a_3 are examples of 1st, 2nd and 3rd pairs. Similarly b_1 and b_2 are 3 site triplets. “ c_1 ” represents a four-site $ijkl$ site. It is also to be noted that J 's in equation (2.2.1-2) are the same for all configurations “ σ ”. Thus if J 's are known, $E_{CE} \approx E_d$ can be calculated by simply summing the spins products.

With reference to Figure 2-15, a_1, a_2 and a_3 are all pair figures, similarly both b_1 and b_2 are triplet figures. Thus for each selected configuration of “ $\hat{S}_{1m} \dots \hat{S}_{im}$ ”, it is possible to define ND_F symmetry-equivalent figures “ F ”. A figure F is defined by the number k of atoms, located on its vertices, the order m of neighbor distance separating them, and by the position l of the figure in the lattice (see Ising models [Kikuchi--1951]). $k=1, 2, 3$, etc. indicates sites, pairs, triplets, etc.; $m=1, 2$, etc. are first, second neighbors, etc; l also includes the orientation.

Then a new function known as the “correlation function” is defined as $\bar{\Pi}_F(\sigma)$. If D_F is the number of figure of cluster per site,

$$\bar{\Pi}_F(\sigma) = \frac{1}{ND_F} \sum_F (\hat{S}_{i1}(\sigma), \dots, \hat{S}_{im}(\sigma)) \quad (2.2.1-3)$$

Then, equation (2.2.1-2) is rewritten as

$$E_{CE}(\sigma) = N \sum_F D_F J_F \bar{\Pi}_F(\sigma) \quad (2.2.1-4)$$

Then, the configuration average energy

$$\langle E_{CE} \rangle = N \sum_F D_F J_F \langle \bar{\Pi}_F \rangle \quad (2.2.1-5)$$

Then, the goal is to find J_F and the $\langle E_{CE} \rangle$. The ensemble average over all the configurations is

$$\langle E \rangle = N \sum_F D_F \langle \bar{\Pi}_F \rangle J_F \quad (2.2.1-6)$$

Where $\langle \bar{\Pi}_F \rangle$ is defined as the correlation functions of a figure. J_F is the effective cluster properties that are needed to be calculated by either ab initio method or other methods. Theoretically if all the figures are included, the above equation gives the accurate prediction of the physical property E for alloys. In practice, only few (30~50) preselected figures are used to approximate ensemble average in equation (2.2.1-6).

Cornolly and Williams Approach to find J_F

First step is to select N_σ configurations. The excess energy of a configuration σ in comparison to $A_{1-x}B_x$ at volume V is defined as

$$\Delta E(\sigma, V) = E(\sigma, V) - [(1-x)E(A, V_A) + xE(B, V_B)] \quad (2.2.1-7)$$

$E(A, V_A)$ and $E(A, V_B)$ are energies of A and B solids at their equilibrium volumes V_A and V_B . Thus

$$E_d(\sigma) = \text{Min}_V \Delta E(\sigma, V) \quad (2.2.1-8)$$

This minimum is obtained by minimizing a weighted function

$$\hat{F} = \sum E_d(\sigma) \left| w_\sigma - N \sum_F^{N_F} D_F J_F \bar{\Pi}_F(\sigma) \right|^2 \quad (2.2.1-9)$$

Where $N_\sigma = N_F$, the minimization was solved by Singular value Decomposition [Connolly & William] to obtain

$$D_F J_F = \sum_\sigma \left[\bar{\Pi}_F(\sigma') \right]^{-1} E(\sigma') \quad (2.2.1-10)$$

σ' and σ are two different sets of configurations of comparable sizes.

2.2.1.4 Special Quasirandom Structures (SQS)

In the mean field approaches, the limitation of early electronic structure theories in describing the alloy is not structural. In VCA (virtual crystal approximation) and SCPA (site coherent potential approximation), all A's average occupations and all B's average occupations are assumed. Wei and Zunger suggested the restriction of the VCA is valence-only electronic structure methods and that of the SCPA is electronic structure methods using atom-anchored representations [Wei & Zunger—1990].

On the other hand, direct sampling method and cluster expansion method are all based on statistically ensemble average over a large set of configurations or figures, respectively. large computation efforts are needed to calculate the physical properties for each configuration or figure.

Another alternative way to analyze a substitutional disordered structure of the $A_{1-x}B_x$ alloy is to construct a large supercell, and the A and B atoms are randomly placed [Martensson—1978]. This approach would require huge supercells to adequately simulate the statistics of the random alloy. Obviously, density functional method is very difficult to use in this approach because it is always constrained by the number of atoms in the unit cell. A method known as the special quasirandom (SQS) method is proposed [Wei & Zunger--1990] to avoid this limitation, with some approximations. SQS method is to construct supercells of varying sizes that can be reasonably handled by available ab initio method and current computational power. The supercell is designed to mimic the statistical characteristics of random alloys to a controllable accuracy. In other words, the correlation functions of the constructed SQS supercells can match the correlation functions of a random alloy with a selected error control.

In SQS, the same definition of figure F is used. To denote the number of atom located on the vertices of figure F, an index, $k=1,2,3,\dots$, is defined.

$k=1$ means all sites or simple site;

$k=2$ means pairs;

$k=3$ means triplets;

To distinguish different possible pair a_1 , a_2 and a_3 or different possible triplets b_1 and b_2 , an index m is introduced. In pairs,

$$a_1: m=1;$$

$$a_2: m=2;$$

$$a_3: m=3;$$

The D_F is the number of equivalent figure per lattice site and there are N lattice sites. If a location l of the lattice site is selected, the correlation function $\bar{\Pi}_F(\sigma)$ is defined

$$\bar{\Pi}_F(\sigma)\Big|_l = \frac{1}{ND_F} \sum_l \Pi_F(l, \sigma) \quad (2.2.1-11)$$

If ϵ_F is the configuration of figure F at the location l to a desired physical property, like E (energy), is

$$E(\sigma) = \sum_{F,l} \Pi_F(l, \sigma) \epsilon_F(l) \quad (2.2.1-12)$$

It can be shown [Wei & Zunger—1990] that $\Pi_F(l)$ forms a complete set of orthonormal functions. Then,

$$\sum_{\sigma} \Pi_F(l, \sigma) \Pi_{F'}(l, \sigma) = 2^N \delta_{F,F'} \delta_{l,l'} \quad (2.2.1-13)$$

Then,

$$\epsilon_F(l) = 2^N \sum_{\sigma'} \Pi_F(l, \sigma) E(\sigma) \quad (2.2.1-14)$$

or

$$E(\sigma) = N \sum_F D_F \bar{\Pi}_F(\sigma) \epsilon_F \quad (2.2.1-15)$$

$$\langle E \rangle = N \sum_F D_F \langle \bar{\Pi}_F \rangle \epsilon_F \quad (2.2.1-16)$$

Only difference, thus far, is to replace sum over 2^N into sum over all cluster properties ϵ_F . The equations in (2.2.1-13) and (2.2.1-14) are not approximate but exact as long as the terms are not truncated in the series. It should be noted that, for a random infinite alloy R, the correlation functions [Wei & Zunger--1990] can be expressed as follows

$$\bar{\Pi}_F(R) = \bar{\Pi}_{k,m}(R) = \langle \bar{\Pi}_{k,m} \rangle_R = (2x-1)^k \quad (2.2.1-17)$$

It is to be noted that these expressions are the same expressions obtained by minimizing ΔE (equation 2.2.1-8) [Wei & Zunger--1990] as long as ϵ_F is interpreted appropriately in terms of J_F . Wei and Zunger describe procedures to obtain the correlation functions to a random infinite alloy R in the appendix of their paper [Wei--1990].

The central idea of practical $\langle \bar{\Pi}_{k,m} \rangle$ application of SQS approximation is to find or design a single “N-atom per cell periodic structure --- S”, whose distinct correlation function $\bar{\Pi}_{k,m}(S)$ best matches the average of the random alloy. If $\langle E \rangle$ is the ensemble average of “the random alloy”, then the errors of a statistically ensemble average with respect to a random alloy can be represented by [Wei & Zunger--1990]

$$\langle E \rangle - E(S) = \sum_{k,m} D_{k,m} [(2x-1)^k - \bar{\Pi}_{k,m}(S)] \epsilon_{k,m} \quad (2.2.1-18)$$

The objective is to find S that minimizes the error. There are many procedures that have been developed to find such “S”. The approximations that are introduced come from

truncating the series of the right hand side of the equation (2.2.1-18). For example, the 1st neighbor correlation function of SQS_8(BCC) is equal to 2nd neighbor correlation function, as well as to 6th and 9th. However, N=64 is needed to account for 3rd neighbors. Thus, the convergence is not uniform in terms of few atoms of the structure S.

To minimize the errors, the minimization is over either the summation of

$$\sum_{k,m} D_{k,m} [(2x-1)^k - \bar{\Pi}_{k,m}(S)] \epsilon_{k,m}$$

in the cluster expansion theory, or to minimize the summation of difference of correlation functions $[(2x-1)^k - \bar{\Pi}_{k,m}(S)]$ as in the SQS method.

With SQS method, one starts to seek a single configuration with large number N, which can be used to approximate the true random alloy structure. For a random infinite alloy R, we have the standard deviation

$$\eta_{k,m}(N) = (D_{k,m} N)^{-\frac{1}{2}} \quad (2.2.1-19)$$

For the approximated lattice structure, the standard deviation will be

$$\eta_{k,m}(N) = \left| \left\langle \bar{\Pi}_{k,m}^2 \right\rangle \right|^{\frac{1}{2}} \quad (2.2.1-20)$$

Benefits of SQS are as follows. Because SQS are periodic structures, that equilibrium geometry, electronic densities and total energy can be obtained from first principles techniques like the density functional theory to the same degree of accuracy as a crystal. In addition to the approximation, due to the representation of exchange-correlation functions and pseudopotential, the error of truncation of the series in equation (2.2.1-18) and the number of atoms in S constitute additional approximation.

2.2.2 EOS for Steels and Alloys

In recent years, the first-principles are successfully applied to study the phase stability of simple crystal structures and their superstructures. However, even for simple crystal structures, there are still important issues that should be addressed in the study of phase stability [Chen--2002] [Colinet--2000] [Zhang--2003]. On the other hand, there are very few published papers on the effect of pressure on the thermodynamic properties and the phase diagram [Sluiter—1990, 1996 & 2001]. For steel alloys that are used as projectile materials, theoretical predictions of their thermomechanical properties, like the equation of state (EOS), phase transition including melting, plastic effects including dislocation evolution, are not developed. Theoretical methods that are currently used for EOS of steel are discussed in section 2.2.2.1 and 2.2.2.2. As will be noted the generalized mixing model (2.2.2.2) is applied only for Ni-Al alloys.

2.2.2.1 *Mixing Model*

The prevalent approximated model used to calculate EOS to study stiffness of materials is called the mixing model, or volume-addition model [Jing—1999, Xu—1986, Meyers--1994]. The basic assumption is the summation of equilibrium volume of each constituent under some pressure P will give the volume of alloys under the pressure P , ie.

$$V(P) = \sum_i n_i v_i(P) \quad (2.2.2-1)$$

where n_i is the concentration and $v_i(P)$ is the equilibrium volume of the i^{th} component at the pressure P . The total internal energy is given by

$$E(P) = \sum_i n_i \varepsilon_i(P) \quad (2.2.2-2)$$

and the enthalpy is

$$H = \sum_i n_i (\varepsilon_i(v_i) + P v_i) = \sum_i n_i H_i(v_i) \quad (2.2.2-3)$$

The limitation of this mixing model is that the thermodynamic quantities are assumed to be the arithmetic average of each constituent, therefore the structure-dependence of these quantities are ignored.

2.2.2.2 *Generalized Mixing Model on the Cluster Expansion (CE) Method*

Due to the constraints of the mixing model, a more general EOS model based on the cluster expansion (CE) method is proposed by Geng in 2004. Avoiding using the arithmetic average of each constituent, he suggested that the cluster expansion method (CEM) is a natural choice for the mixing model corresponding to the point approximation of CEM, where the convergence can be guaranteed under the assumption of the short-range interaction.

The internal energy and pressure are separately written as $E = E_x + E_v + E_e$ and $P = P_x + P_v + P_e$, where x corresponds to the cold curve energy, v corresponds to the thermal contribution from the lattice vibrations, and e corresponds to the thermal contribution from the electrons. The effects of temperature and compression on ionization are neglected. With the cluster expansion methods, the cold curve free energy can be expressed by means of correlation functions as [Connolly--1983]

$$E_x(V) = \sum_n v_n(V) \xi_n \quad (2.2.2-4)$$

The free energy of thermal vibrations [Garbulsky--1994] can be written as

$$F_v(V, T) = \sum_n w_n(V, T) \xi_n \quad (2.2.2-5)$$

where ξ is the cluster correlation function as defined in (2.2.2-5) [zhang--2003]. The thermal contribution of the electrons is represented by an integration involving the configurational electronic density of state $n_\sigma(E)$:

$$F_e(\sigma, T) = \int_0^{\mu(T)} n_\sigma(E) [Ef(E) + k_B T [f(E) \ln f(E) + (1 - f(E)) \ln(1 - f(E))]] dE \quad (2.2.2-6)$$

where E is the energy level, $f(E)$ is the Fermi-Dirac distribution. Therefore, for any configuration,

$$F_e(V, T) = \sum_n \lambda_n(V, T) \xi_n \quad (2.2.2-7)$$

can be obtained by using CEM. v_n , w_n and λ_n can be provided from either ab initio calculations or fitting to experimental data. The thermodynamic properties and equilibrium state can be calculated by using the cluster variation method [Kikuchi--1951]. With the above expressions and known values,

$$F_e(V, T) = \sum_n \lambda_n(V, T) \xi_n \quad (2.2.2-8)$$

v_n , w_n and λ_n can be provided from either ab initio calculations or fitting to experimental data. The thermodynamic properties and equilibrium state can be calculated by the cluster variation method (CVM) [Kikuchi--1951]. With these expressions and known values, pressure can be obtained by

$$P_x = -\frac{\partial E_x}{\partial V} \quad (2.2.2-9)$$

$$P_T = -\left(\frac{\partial F_T}{\partial V}\right)_T \quad (2.2.2-10)$$

The generalized EOS model can be constructed as follow

$$P_x(V) = -\sum_n \frac{\partial v_n(V)}{\partial V} \xi_n \quad (2.2.2-11)$$

$$P_v(V, T) = -\sum_n \frac{\partial w_n(V, T)}{\partial V} \xi_n \quad (2.2.2-12)$$

$$P_e(V) = -\sum_n \frac{\partial \lambda_n(V, T)}{\partial V} \xi_n \quad (2.2.2-13)$$

Geng investigated the EOS of Ni-Al alloys by using this generalized mixing model and density functional calculations at the ground state. It is one of the very few works on the investigation in EOS of alloys. He also obtained a good agreement with experimental data [Simmons—1971, Freeman—1992, Pearson—1958, Kittel—1976, Stassis—1981, Otto--1997]. The GGA approximation and LDA method are used in the calculations.

2.2.2.3 *EOS for Crystalline Structure: Alloys based on SQS method*

As is discussed, SQS method can be used to construct a virtual structure or an approximate supercell that can represent the statistical correlation functions of random alloys. Therefore, this reduced size of system represented by SQS structure can then be used in the first principle calculations to obtain EOS. A virtual periodic structure is constructed by using the supercell. This means that an alloy can be treated as a crystalline structure with SQS supercell as its unit cell. Then, the physical properties of alloys can be predicted based on this virtual crystalline structure. For a crystalline structure, a

procedure and formulations to obtain its EOS are discussed in Chapter 5 [Lu & Hanagud—2005].

2.3 Ab Initio Methods

A solid can be viewed as a collection or a system of interacting positively charged nuclei and negatively charged electrons. Theoretically, this system can be solved exactly by solving the many-body Schrödinger's equations including the degrees of freedom of interacting nuclei and electrons.

2.3.1 Schrödinger Equation and Wave Function

The many-body Schrödinger's equation governing a system of interacting nuclei and electrons can be written as follows.

$$\hat{H}\Phi(\vec{x}_1, \vec{x}_2, \dots, \vec{x}_N, \vec{R}_1, \vec{R}_2, \dots, \vec{R}_M) = E\Phi(\vec{x}_1, \vec{x}_2, \dots, \vec{x}_N, \vec{R}_1, \vec{R}_2, \dots, \vec{R}_M) \quad (2.3.1-1)$$

Where \hat{H} is the Hamilton operator for a molecular system. R_I is the nuclei coordinate, r_i is the electron coordinates, N is the number of electrons and M is the number of nuclei in the absence of magnetic or electric fields. E is the total energy of the system. Theoretically the system is completely determined by Schrödinger's equation, however, only a small system like a hydrogen atom system with only one electron can be solved analytically. To find the numerical solution to the equation (2.3.1-1), several levels of approximations are discussed.

2.3.2 Born-Oppenheimer Approximation

Since nuclei are much heavier than the electrons, the electrons can be assumed to move much slower than the nuclei. In other words, the electrons move instantaneously with fixed nuclei and always are at their ground state. By this Born-Oppenheimer assumption, the Schrödinger equation is simplified.

$$\Phi(\vec{x}_1, \vec{x}_2, \dots, \vec{x}_N, \vec{R}_1, \vec{R}_2, \dots, \vec{R}_M) = \Psi(x, \vec{R})\chi(\vec{R}) \quad (2.3.2-1)$$

Therefore, the Schrodinger equation is rewritten as the follows:

$$\begin{cases} \hat{H}_{elec} \Psi_n(x, \vec{R}) = E_n(\vec{R})\Psi_n(x, \vec{R}) \\ \hat{H}_{nuclei} \chi(\vec{R}) = \epsilon \chi(\vec{R}) \end{cases} \quad (2.3.2-2)$$

The “frozen” nuclei only contribute to an external potential for the electrons.

2.3.3 Density Functional Theory [Kohn & Sham--1965]

The many interacting electrons system represented in equation (2.3.2-2), is still in essence a many-body problem and therefore very difficult to solve. Most modern electronic calculations for solids are based on the density function theory (DFT) proposed by Kohn and Sham [Kohn & Sham--1965]. DFT is based on Hohenberg and Kohn Theorems, which states that (1) The ground-state energy of a many body system is a unique functional of the electron density: $E_0 = E[\rho(\vec{r})]$, where the electron density is $\rho(\vec{r}) = N_e \int \dots \int |\Psi(x)|^2 ds_1 d\vec{r}_2 \dots d\vec{r}_{N_e}$ and N_e the number of the electrons; and (2) The functional has its minimum at the equilibrium density $E_0 = E[\rho_0(\vec{r})] = \min_{\rho \rightarrow \rho_0} \{E[\rho(\vec{r})]\}$.

By introducing a reference system of non-interacting electrons, the Kohn-Sham theory

reduces a many-body interacting electron system to a single-electron system that account for the interacting between electrons through an exchange-correlation functional. This single-electron system is governed by

$$\left[-\frac{\hbar^2}{2m_e} \nabla_i^2 - \frac{e^2}{4\pi\epsilon_0} \sum_{I=1}^N \frac{Z_I}{|\vec{r} - \vec{R}_I|} + \frac{e^2}{4\pi\epsilon_0} \int \frac{\rho(\vec{r}')}{|\vec{r} - \vec{r}'|} d^3\vec{r}' + V_{XC}[\rho(\vec{r})] \right] \psi_i(\vec{r}) = \epsilon_i \psi_i(\vec{r}) \quad (2.3.3-1)$$

where V_{XC} is given by the exchange-correlation functional which is obtained by taking a derivative of the exchange-correlation energy E_{XC} with respect to the electron density. However, the exact form of the exchange-correlation energy E_{XC} is unknown. Then the problem is reduced to solve for a single-electron system with $\psi_i(\vec{r})$ as the Kohn-Sham orbitals, and ϵ_i the energy of the system.

2.3.4 Approximations in the Density Functional Theory

Many approximations have been made to solve the equations in (2.3.3-1).

(1) First, as discussed in above, we have to determine the exchange-correlation energy. A so-called local density approximation (LDA) [Ceperley & Alder] assumes that E_{XC} only depends on the local charge density.

$$E_{XC}[\rho(\vec{r})] = \int \rho(\vec{r}) \epsilon_{XC}[\rho(\vec{r})] d^3\vec{r}$$

where ϵ_{xc} is the exchange-correlation energy for homogeneous electron gas at the same charge density. LDA is a good approximation both for systems with a slowly varying density. But it usually underestimates the lattice volume while underestimating cohesive energies. By introducing the spin density, local spin density approximation (LSDA) was proposed as an extension of the LDA. The so-called generalized gradient approximation

(GGA) was introduced to correct the inaccuracies by including the non-local effects through the gradient of the charge density. GGA usually predicts better lattice constants than LDA does. Many versions of GGA are proposed. Taylor-series expansion was introduced in the charge-density gradient but yields poor results [Gunnarsson--1976]. Generalized gradient approximation shows its success in predicting physical properties and energy. The most widely used are GGA_PW-91 (Perdew & Wang-I) and GGA_PW-II (Perdew & Wang-II) or PBE (Perdew-Burke-Ernzerhof).

(2) To represent the Kohn-Sham orbital in a set of basis functions, we have several options: Slater or Gaussian orbitals, plane waves, linearized augmented plane wave, linear muffin tin orbitals (LMTO), projector augmented waves (PAW) [Kresse--2005], etc. Plane waves and its extended versions are used for solids, which have periodic structures and characteristics. However, orbital type of basis functions like LMTO have been adapted for the applications to solids. PAW is based on plane waves, however, by introducing the projector augmentation, the characteristics of the strong oscillations close to the nuclei region, which are smoothed out by representations of pure plane waves, are approximately reproduced [Kresse--2005].

(3) It is assumed that most physical properties of solids depend on the *valence* electrons to a much greater degree than that of the tightly bound *core* electrons. The core electrons can be approximated to be *frozen* in their core configurations. This approximation considerably simplifies the task of solving the Kohn Sham equations, by eliminating all degrees of freedom related to the core orbitals. The nuclear potential is replaced by a *weaker pseudopotential*, which takes into account the effects of the nucleus

and the core electrons. Pseudopotential acts on a set of *pseudo* “wavefunctions” rather than the true valence “wavefunctions”.

$$\begin{aligned}
 & \left(-\frac{\hbar^2}{2m} \nabla^2 + e^2 \int \frac{n^{ks}(\vec{r}')}{|\vec{r}-\vec{r}'|} d^3r' + V_{Nc}(\vec{r}) + \mu^{xc}[n] \right) \phi_i(\vec{r}) = \epsilon_i \phi_i(\vec{r}) \quad i=1, \dots, N \\
 & \quad \quad \quad \downarrow \quad \quad \quad \downarrow \quad \quad \quad \downarrow \text{Frozen core} \\
 & \left(-\frac{\hbar^2}{2m} \nabla^2 + e^2 \int \frac{n^{ks}(\vec{r}')}{|\vec{r}-\vec{r}'|} d^3r' + V_{psudo}(\vec{r}) + \mu^{xc}[n] \right) \tilde{\phi}_i(\vec{r}) = \epsilon_i \tilde{\phi}_i(\vec{r}) \quad i=1, \dots, N_{\text{valence}} \\
 & \quad \quad \quad \downarrow \quad \quad \quad \downarrow \\
 & \quad \quad \quad \text{†: orbital} \quad \quad \quad \boxed{\tilde{\phi}_i(\vec{r}) : \text{the Pseudo valence wavefunctions}}
 \end{aligned}$$

Various pseudopotentials have been proposed. A so-called norm-conserving pseudopotential that constrains the charge by pseudo wavefunctions, within a cut-off sphere around the nuclei, to be equal to the charge by the true wavefunctions. This pseudopotential requires a large cut-off energy for the first-row and transition elements. There is another pseudopotential called ultrasoft Vanderbilt pseudopotential [Kresse--2005] that relaxes the norm-conservation constraint and add augmentation charges inside the cut-off sphere to correct charge. These pseudopotentials are much softer potentials in the core region, so that they generate significantly *smoother pseudowavefunctions* and therefore result in a reduction of the size of the basis set and cut-off energies. PAW pseudopotentials decompose the wave functions or orbitals, charge densities, kinetic energy into three parts (Figure 2-16): pseudo, pseudo-onsite radial grids and exact onsite grids. Through a projector augmentation, the all-electron wave functions can be produced (Figure 2-17).

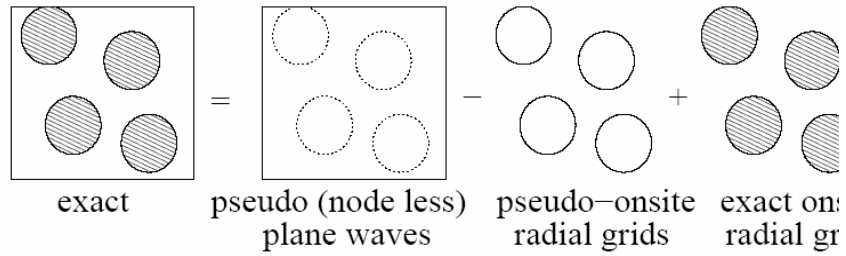


Figure 2-16. PAW method and its decomposition.

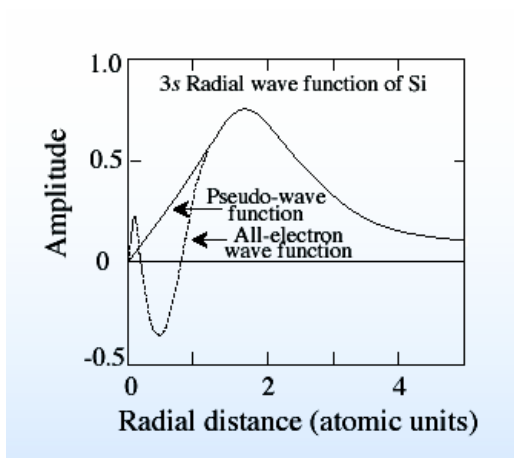


Figure 2-17. Plane waves and PAWs.

The Kohn-Sham equations are solved using iterative matrix diagonalization that was based on the minimization of the norm of the residual vector to each eigenstate [Kresse--2005] and optimized charge- and spin- mixing routines. The calculations are implemented by a self-consistent cycle. First, an initial charge density function is obtained by guessing; then the one-electron Kohn-Sham's equations are solved to obtain a new charge density. The loop is repeated until the difference in two total energies reaches some convergence constraint.

2.4 Studies of Iron from First Principles

As is known, iron is the host material for steel alloys. Therefore, the studies of iron using ab initio methods will provide both a foundation and a calibration for the studies of steels. There are many published papers on the physical properties of iron in the past thirty years. Three main crystal structures of iron are body-centered cubic (bcc), face-centered cubic (fcc) and hexagonal close-packed (hcp). Hexagonal close-packed (hcp) iron, the form stable at high pressure, plays an extremely important role in geophysics.

A. Magnetism in iron

Magnetism plays an important role in understanding the physical properties of the iron and iron alloys, including the relative stability of the iron polymorphs [Gerd-2004]. There are many papers related to this research area. For example, a comprehensive study of the ground-state properties of metals has been presented by Moruzzi, Janak and Williams [Moruzzi--1978] by using the Korringa-Kohn-Rostoker (KKR) method with a LSDA exchange-correlation potential in 1978. Their study includes 3d ferromagnetic metals. In 1981, Kubler [Kubler-1981] investigated the total energies of nonmagnetic, ferromagnetic and antiferromagnetic states for both bcc and fcc phases of iron by using the augmented-spherical-wave (ASW) method. He found that the bcc structure has the lowest energy to ferromagnetic (FM) state, while the fcc has the lowest energy to antiferromagnetic (AFM) state. In the past thirty years, many papers were published to study the magnetism performance in the different crystal structures of iron.

Different forms of magnetic behavior indicate different symmetry considerations. Actually all materials possess some magnetic behavior more or less. To classify the

magnetism types, the response of the material in a magnetic field, the magnitude and orientation of magnetic moments will be considered in the unit cell. Generally magnetic behavior can be divided into five groups: Ferromagnetism, antiferromagnetism, ferrimagnetism, diamagnetism and paramagnetism. The differences in the magnitude and orientation originate from the differences in magnetocrystalline anisotropy and exchange interactions for different materials. Magnetocrystalline anisotropy involves the electron spin-orbital interactions and crystal fields [Hurd--1982], which generates the orientation for the magnetic moments at the minimum energy. These exchange interactions are required by the Pauli exclusion principle. It is known that a pressure will affect the magnetic structure through the delicate balance between the potential energy and the kinetic energy. Potential energy stabilizes a magnetic state and kinetic energy stabilizes a nonmagnetic state. Due to the Pauli exclusion principle, spin electrons can not occupy the same spatial orbital, potential energy is lowered by balancing spins so that spin electrons repel each other less than unlike spins. This results in the lower potential energy and higher kinetic energy because same spin electrons occupy the higher layer, as the following, magnetism becomes favorable in materials, such as bcc iron. When pressure becomes large, the electronic bands are wider and the separation between the layers tends to increase, which causes the magnetic moments to decrease in magnitude. In this situation, volume becomes small. The magnetization energy is less favorable at the smaller volumes.

Based on the above magnetism classifications, the magnetic phases studied here are non-magnetic (NM), ferromagnetic (FM) and antiferromagnetic (AFM). These three magnetic phases will be investigated in the structure bcc, fcc and hcp, respectively. In the

range of lower-pressure, two polymorphs of iron are both magnetic. Around ambient conditions, FM in the body-centered cubic (bcc) is the stable magnetic phase. Above the Curie temperature, spins tend to be disordered and the net magnetization is to disappear. But there is still some individual atomic moments unchanged in magnitude because high temperature has little influence on the electronic structure. Around the low pressure with high temperature, there will be a phase transition from bcc to fcc, where NM is prevalent. The magnetism in hcp is more complicated. It has been debated for thirty years, which results in the contradiction between experiments and theory. The reason of the contradiction is because the experiments [Williamson—1972, Cort—1982, Nasu-2002, Taylor--1991] suggest that hcp iron is nonmagnetic, but computational studies [Gerd--1999] based on density function theory (DFT) show an antiferromagnetic (AFM) at the ground state when pressure is close to 50Gpa. Investigating these magnetic phases are important in understanding the physical properties of iron and steel. To the impact phenomena in iron and steel, pressure is very high, thus hcp is of special interest because this structure is the high pressure phase of iron.

In chapter 5, the magnetism of pure metal iron will be studied based on its different lattice structures by using ab initio method. As the references, in 1985 Wang used the total-energy general potential linearized-augmented-plane-wave (LAPW) method [Andersen—1975, Koelling—1975, Wimmer—1981 & Hamann--1979] to calculate magnetic moments, which is presented in Figure 2-18. The magnetic moment and magnetic energies are predicted by using DFT based methods to the hcp AFM phase [Gerd--1999].

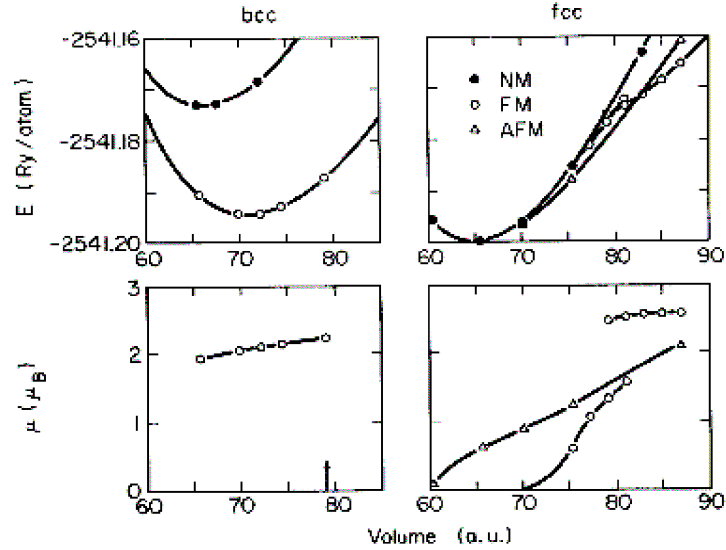


Figure 2-18. Total energy/atom and magnetic moment of NM, FM and AFM phases of bcc and fcc iron [Wang--1985].

B. Equation of State and Phase Transition

The stress tensor σ_{ij} can be decomposed into two parts, hydrostatic pressure P and deviatoric stress tensor σ'_{ij} , therefore, $\sigma_{ij} = -P\delta_{ij} + \sigma'_{ij}$. Equation of state (EOS) describes the dependence of pressure on the density ρ (or volume v) and temperature T , which is $P=P(\rho, T)$. $P=P(\rho, 0)$ is the EOS at the ground state. The experimental techniques include the static high-pressure by diamond-anvil cells up to 0.3Tpa, gas gun tests and shock high-pressure by nuclear explosive up to 1Tpa. Moreover, because of difficulties of directing temperature measurement in shocked systems and the difficulty of temperature control in the static system, EOS always has incomplete information. Thus, it is very meaningful to theoretically predict the EOS by using first principles. In this thesis, corresponding to the 1-D and 2-D impact and penetration models, from the view of iron and alloy used for projectiles, the EOS of iron at ground state will be presented to compare with that of alloy steels.

First principles are used to calculate EOS of solids for almost three decades [Boettge-1999, Cohen—2001, Godwal—1979, Greene—1994, Katsnelson—1997, Nellis—1998, Sikka—1988, Xie-2000, Akber-Knutson—2002, Lizhi—2001, Milman—2001 & Kushwah-1998]. The results of EOS investigation by using first principle have been a benchmark in the studies of the high-pressure solid mechanics. Earliest studies of the EOS of iron were developed with the development of density functional theory (DFT) based techniques. Better approximations of exchange and correlation potentials have been explored, like Augmented-plane-wave (APW) and Muffin-tin approximation. In 1994 Stixrude investigated the energetics of bcc, fcc and hcp structures with the Perdew-Wang-II [Amador—1992] functional by using the general potential linearized-augmented-plane-wave (LAPW) method. His results show excellent agreement in EOS, phase transition and magnetic moments between the experiments [Jephcoat—1986] and computations. He claimed bcc is more stable than fcc at the low temperature in his investigation, which is in agreement with the previous results [Bagno—1989, Barbiellini—1990, Leung—1991, Singh—1991, Amador—1992, Asada—1992 & Haglund--1993]. He also suggested the LAPW method is free of shape approximations to the charge density or the potential. This is important because some errors in the bcc-fcc energy difference will generate to the muffin-tin or the atomic-sphere approximation (ASA) that are shape approximations. His calculation also shows that the phase transition from bcc to hcp at the ground state happens at 11Gpa. This is very similar to the results obtained from LMTO-ASA calculations with the PW-I [Bagno—1989, Barbiellini—1990, Leung—1991, Singh—1991] functional by Asada and Terakura in 1992. By using the local density approximation (LDA) and the generalized gradient approximation

(GGA) developed by Perdew and co-workers [Perdew--1992], John displayed his hcp EOS in 1996, which has the excellent agreement between the EOS from GGA and experiments, while the EOS from LDA systematically underestimates the pressure by about 25-40Gpa.

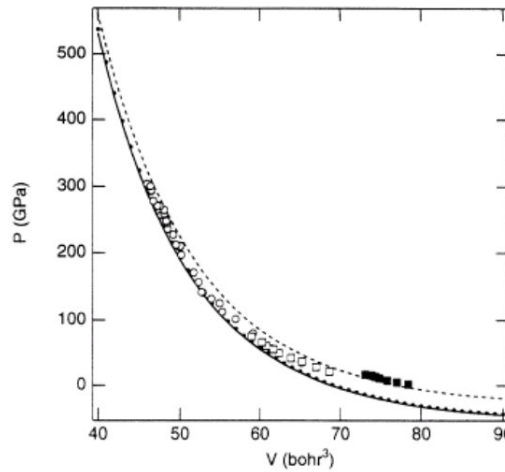


Figure 2-19. GGA pressure-volume relations for bcc (dashed line), fcc (dotted line) and hcp (solid line).

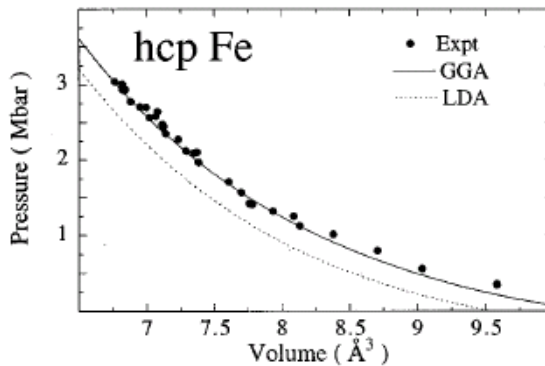


Figure 2-20. Calculated GGA and LDA pressure-volume relations for hcp Fe compared with room-temperature static compression data of [Mao--1990].

2.5 Scope of the Thesis

In Chapter 3, the objectives and the specific problems discussed.

In Chapter 4, a one-dimensional reduced model for impacts and penetrations of a deformable projectile into a deformable target is developed. The context includes (1) the formulation of the 1-D impact and penetration problem of varying cross-section area; (2) the development of 1-D time-dependent simplified penetration models; (3) the effect of phase transition; (4) nose shape change; and (5) numerical examples.

In Chapter 5, ab initio studies of iron are presented. First, various approximations and their combinations in the density functional theory are discussed. Convergence tests for calculations are performed. Secondly, thorough investigations on the structural and magnetic phases of iron by using ab initio methods are implemented. Structural and magnetic phase transitions and the EOS of iron are presented. By comparing to experimental data and previous analysis, the selection of approximations in the DFT is discussed and used in new studies of steel alloys in Chapter 6.

In Chapter 6, a SQS-N structure is first constructed for a disordered binary alloy $\text{Fe}_{1-x}\text{Ni}_x$. Then carbon as interstitial impurity is added in the favorable O-sites (Octahedral sites) of the disordered binary alloy $\text{Fe}_{1-x}\text{Ni}_x$, as a third constituent in a ternary alloy $\text{Fe}_{1-x}\text{Ni}_x\text{C}_y$. Ab initio calculations are implemented to predict the EOS for these two alloys. Comparison of the EOS of these alloys is made with that of pure iron, which is the host material. The effects of each species including Ni and C on the EOS and magnetic orders are discussed.

In Chapter 7, the conclusions of this thesis and recommendations for future work are presented.

CHAPTER 3

OBJECTIVES & THESIS TASKS

The objectives are to seek an understanding of the impact and penetration mechanics of metallic kinetic energy projectiles into hard targets at high striking velocities, with an emphasis on the nose erosion, change in the nose shape, plastic flow in the target and the projectile and possible phase transition. This objective also includes development of simplified models that do not require the integration of a system of partial differential equations. The second objective is to use the understanding of penetration mechanics and ab-initio or first principles techniques to design projectile (alloy) material that can have the desired characteristics to minimize or eliminate erosion, the penetration of a kinetic energy projectile in the hard targets at high striking velocities.

3.1 Reduced Models for Studies of High-Velocity Impact and Penetration

In this thesis, the Tate and Walker's model is modified and combined with the cavity expansion model by Hanagud and Ross to consider a conical nose-shaped projectile penetrating into specific targets. A one-dimensional reduced model that accounts, for the varying cross-section area at the nose, is developed. The modification from Walker's model consists of the effects of the nose shape, the plastic flow with increasing yield stress behind the shock wave, conversion of plastic work into heat and the phase transition near the nose tip. A consideration of the phase transition is important

to explain the experimental results of penetration of steel projectile with striking velocities in the range of 1500 m/sec into concrete targets.

3.2 Material Characterization of Projectile Materials from First

Principles

Steel alloys are widely used as penetrator materials. Traditionally the thermomechanical properties of these alloys are determined through extensive experimental measurements. However, design of a new type of alloys, with superior characteristics like high erosion resistance, needs a theoretical remedy due to insufficient experimental data and the consideration of addition of new elements into the alloy, to improve the penetration performance.

Currently, theoretical analysis of disordered alloys, especially from first principles, is still an active research area in physics, material science and engineering. In this thesis, a theoretical characterization of disorder alloys of interest is studied by SQS method for a binary alloy $\text{Fe}_{1-x}\text{Ni}_x$ and a ternary alloy $\text{Fe}_{1-x-y}\text{Ni}_x\text{C}_y$. The analysis is new and is intended to investigate the effects on mechanical and magnetic properties of some common constituents used in steels: nickel and carbon. The SQS (special quasirandom structure) method is used to construct a system of small size (periodic structures), which then can be characterized by ab initio methods. This virtual structure, although of small sizes, mimics the correlation functions of a random alloy approximately. For analyzing ternary alloy, the third constituent carbon is treated as an interstitial addition. The carbon is added to the favorable sites in the constructed virtual structure representing the binary alloy. This procedure can be extended to consider more elements and phase transitions

including melting. When this work is considered with the first problem, stress in the shank of the projectile can be determined. This will assist in new designs of the shank with dual functional structural energetic materials.

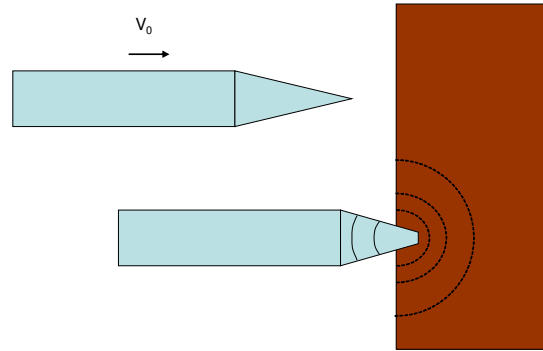
CHAPTER 4

REDUCED MODELS FOR PENETRATION MECHANICS

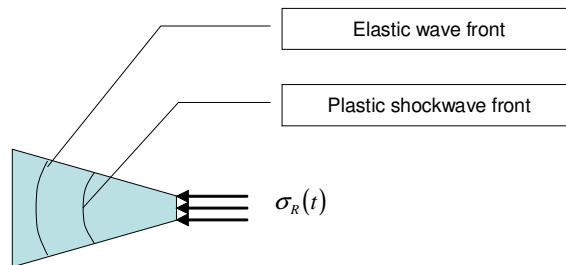
To study and understand the problem of impact and penetration, the resulting blunting of the nose and possible phase transitions, a projectile with a cylindrical shank and a conical nose shape is considered. The target is assumed to be a very thick slab of materials like rock, concrete or metallic materials. The projectile impacts the target and is assumed to be penetrating into the target. In general, it is necessary to study a three dimensional problem with finite deformations, high strain rates, plastic flow and phase transitions. When a phase transition takes place, it is necessary to consider a mixture of phases and the associated thermodynamics. The general equations have been formulated by Lu and Hanagud [Lu & Hanagud--2002]. However, numerical solutions have been obtained only for very simple cases. The objective of the present work is to eliminate the numerical integration of complicated partial differential equations, and obtain simplified models that can be used to estimate the possible phase transition. Before making assumptions, to simplify the constitutive equations, the geometry is simplified. In the first step, the projectile is assumed to be a one dimensional projectile with a varying cross section to consider a realistic nose of the projectile.

The effect of the shock wave propagating into the target is to provide a resisting force (moment) on the projectile. A normal impact of the projectile with a straight path through the projectile is assumed, with no resultant moment on the projectile. Initially,

the observed blunting and phase transitions are in a region surrounding the nose tip and a small portion of the nose. Thus the following simplified problem is considered.



(a) Impact and penetrate



(b) Wave propagates in the projectile and target resistant force acts on the nose tip.

Figure 4-1. The projectile impacts and penetrates into the target.

The resisting stresses σ_R from the target are assumed to be determined (approximately) by the cavity expansion theories developed by Goodier and modified by Hanagud and Ross to include compressibility effects. The first step is to derive conservation equations for a projectile with a varying cross section. To determine the types of differential equations that should be considered in the model, a penetration and nose erosion mechanism is hypothesized.

4.1 Hypothesis and Conservation Equations

In the past, the impact and penetration mechanics are studied by formulating conservation equations and constitutive models in the form of partial differential equations. Then conservation equations usually consisted of conservation of mass, conservation of momentum and sometimes conservation of energy. The constitutive equations consisted of equations that included elastic behavior and different plasticity models that accounted for high strain rates. The formulated partial differential equations, are, very often, integrated numerically by using many different numerical procedures. However, these procedures are not able to explain the changes in nose shape, loss of materials from the nose, thermal softening, possible phase transition including melting and a resulting reduced length of the projectile. However, it is well documented that the changes in the nose shape are important in the penetration performance [Wilkins—1978, Hill—1980, Batra—1987 & Walker--1995]. To remedy the situation and determine the equation that are necessary in this task, a physical model is first hypothesized.

The impact of a metallic projectile, on a target, produces shock waves in the projectile and the target. The shock waves in the projectile, at high striking velocities, can produce high stresses and induce a significant amount of deformation at high strain rates that includes plastic flow. The high stresses associated with high strain rate deformation, generate a large amount of heat due to dislocation pile-up, release and thus resulting plastic work. This can result in structural phase transitions. The interaction of softened projectile materials can result in nose erosion and a change of the nose shape from a pointed end to a different shape. Nose erosion can redistribute stresses resulting from the impact of the projectile with a hard target.

4.1.1 Hypothesis of Sequence of Events Leading to Nose Erosion

When a hard projectile penetrates into a soft target, no significant nose erosion is observed. However, when a deformable steel projectile encounters targets that contain materials harder than the steel, nose erosion is observed. The concrete contains aggregates (granite) that are harder than steel. This means that the aggregate can make an indentation on the steel and result in a material removal from the nose region (Figure 4-2).

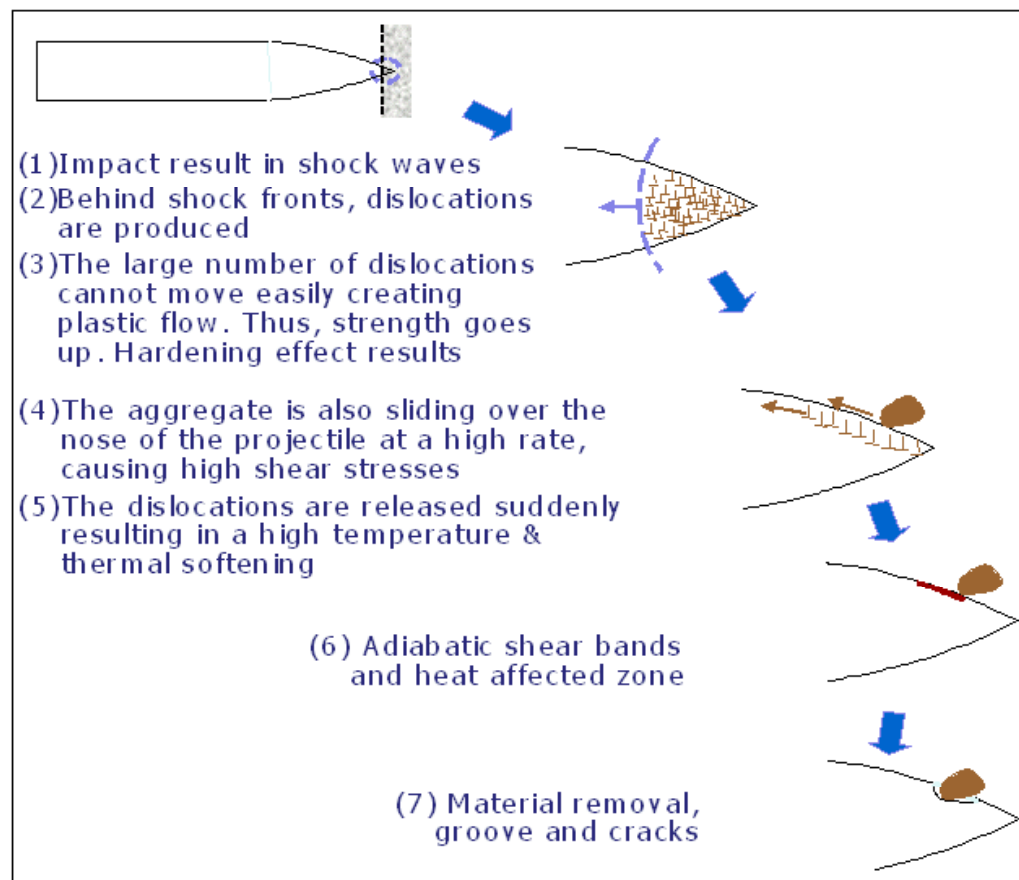


Figure 4-2 Nose erosion mechanisms.

- Aggregates (granite) in the concrete are harder than the steel. An impact with target can result in shock waves in the projectile (Figure 4-2-1) and the target.
- Behind shock waves, a significant amount of dislocations are produced (Meyers 1994, Armstrong 1998) (Figure 4-2-2,3)
- A large number of dislocations that are produced, at the sharp nose tip, cannot move easily. Thus, yield strength goes up.
- During the impact and penetration of steel (4340) projectiles into concrete, concrete is sliding (or flowing) past the steel projectile. Aggregates, in the concrete, can break loose and slide over the nose of the projectile. This can also result in both an indentation of the surface of the nose and can cause high shear stresses.
- Following the passage of the shock wave and development of high shear stresses, the dislocations that are some times described by the term “pile-up” are released suddenly resulting in a large amount of plastic flow and cause a large increase of temperature (Figure 4-2-4,5) due to plastic work.
- Interaction of dislocations and heating result in a thermal softening effect and possible phase changes including melting [Armstrong--1998].
- Adiabatic shear bands [Chang--1987] can also form (or melting can take place following shear band formation) (Figure 4-2-6).
- These events can result in extensive deformation, a possible failure and a removal of the material of the projectile from the nose causing erosion.

- In some cases, phase changes result in melting of the steel and contribute further to the erosion and removal of the material.

The currently available computer codes, for impact and penetration of a kinetic energy projectile, can not explain these phenomena. These computer codes that are used to predict impact and penetration are based on finite deformations, macroscopic elastic-plastic behavior with different types of strain hardening and specified equations of state. In these computer codes, models are not available to include the observed amount of production of heat due to high-strain-rate plasticity behind the shock front, resulting in high temperatures due to shock compression, dislocation of “pile-up” and plastic flow. In addition, the phenomena of phase changes under conditions of high strain rates, high pressures, high temperatures, shear stresses and other defects are not included in these computer codes.

In the next section, equations are developed for a 1-D strain problem with varying cross-section.

4.2 1-D Impact and Penetration Problem

4.2.1 Formulation of 1-D problem with varying cross section area

Mass Balance Equation: Consider a small differential volume of length dx as shown below. Here the cross sectional area varies with distance x .

The accumulation of mass=(Input-Output)+Source

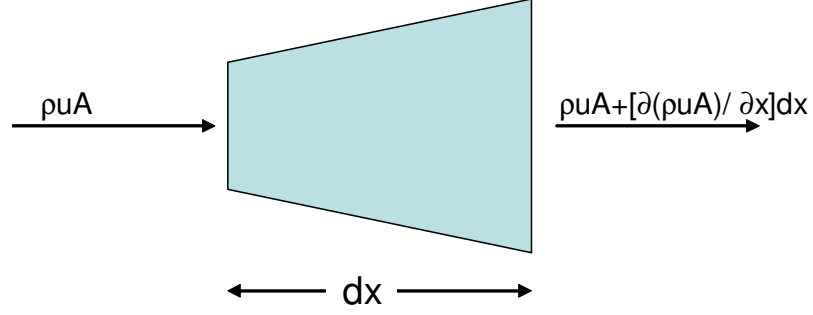


Figure 4-3. Schematic view of a differential element in Eulerian coordinate system.

$$\frac{\partial}{\partial t} [\rho A dx] = \left[\rho u A - \left\{ \rho u A + \frac{\partial}{\partial x} (\rho u A) dx \right\} \right] + \frac{\partial m'}{\partial t} A dx \quad (4.2.1-1)$$

$$\frac{\partial}{\partial t} [\rho A dx] + \frac{\partial}{\partial x} (\rho u A) dx = \eta M \theta A dx \quad (4.2.1-2)$$

$$\text{or } \frac{D\rho}{Dt} + \frac{\rho}{A} \frac{DA}{Dt} + \rho \frac{\partial u}{\partial x} = \eta M \theta \quad (4.2.1-3)$$

where $\frac{D}{Dt} = \frac{\partial}{\partial t} + u \frac{\partial}{\partial x}$

Phase Transition Equation: to consider phase transition, one can consider mixture of materials (different phases), the mass balance equation is:

$$\frac{\partial}{\partial t} [{}^P P^P \xi A dx] = \left[{}^P P^P \xi u A - \left\{ {}^P P^P \xi u A + \frac{\partial}{\partial x} [{}^P P^P \xi u A] \right\} \right] + \frac{\partial m'}{\partial t} A dx + {}^P \psi A dx \quad (4.2.1-4)$$

where left upper index P represents the different phase.

Or define $\bar{\rho} = \sum_P {}^P P^P \xi$ and $\bar{\rho}^P \gamma = {}^P P^P \xi$

$$\frac{\partial}{\partial t} [\bar{\rho}^P \gamma A] + \frac{\partial}{\partial x} [\bar{\rho}^P \gamma u A] = \eta^P M \theta A + {}^P \psi A \quad (4.2.1-5)$$

with

$${}^P\psi = {}^P\psi_{\text{gain}} - {}^P\psi_{\text{loss}} = \sum_{m \neq P} \left({}^m\xi^m \rho A_{m \rightarrow P} - {}^P\xi^P \rho A_{P \rightarrow m} \right) = \bar{\rho} \sum_{m \neq P} \left({}^m\mathcal{A}_{m \rightarrow P} - {}^P\mathcal{A}_{P \rightarrow m} \right) \quad (4.2.1-6)$$

$${}^P\gamma \frac{D\bar{\rho}}{Dt} + \bar{\rho} \frac{D^P\gamma}{Dt} + \frac{\bar{\rho}^P\gamma}{A} \frac{DA}{Dt} + \bar{\rho}^P\gamma \frac{\partial u}{\partial x} = \eta^P M \theta + \bar{\rho} \sum_{m \neq P} \left({}^m\mathcal{A}_{m \rightarrow P} - {}^P\mathcal{A}_{P \rightarrow m} \right) \quad (4.2.1-7)$$

from $\frac{D\bar{\rho}}{Dt} + \frac{\bar{\rho}}{A} \frac{DA}{Dt} + \bar{\rho}^P \frac{\partial u}{\partial x} = \eta^P M \theta$, the following equation is obtained:

$$\frac{D^P\gamma}{Dt} = \sum_{m \neq P} \left({}^m\mathcal{A}_{m \rightarrow P} - {}^P\mathcal{A}_{P \rightarrow m} \right) \quad (4.2.1-8)$$

where ${}^P\gamma$ belongs to $[0,1]$. \bar{e} is the internal energy. M is the molecular mass (g/mole). H is Stoichiometric coefficient. Θ is reaction rate (mole/L sec).

Linear Momentum Balance Equation: The momentum depends on the accumulation rate, which is equal to the input rate minus the output rate plus any sources. All stresses are assumed to be subjected to the same stress σ_{xx} (Figure 4-4). The linear momentum balance can be written into the following equation:

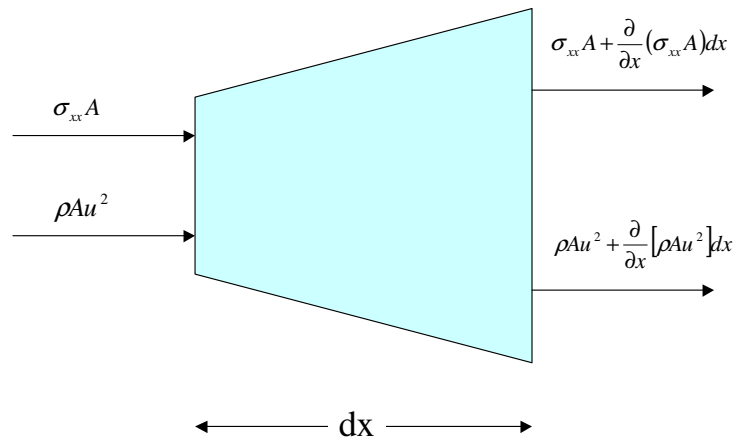


Figure 4-4. Schematic view of a differential element ($A dx$) in Eulerian coordinate system.

$$\frac{\partial}{\partial t}[\rho u A dx] = \rho A u^2 - \rho A u^2 - \frac{\partial}{\partial t}[\rho A u^2] dx + \frac{\partial m^r}{\partial t} u + \left[\sigma_{xx} A + \frac{\partial(\sigma_{xx} A)}{\partial x} dx \right] - \sigma_{xx} A \quad (4.2.1-10)$$

This equation can be simplified to be

$$\frac{\partial}{\partial t}[\rho u A dx] + \frac{\partial}{\partial x}[\rho A u^2] dx = \eta M \theta A dx u + \frac{\partial(\sigma_{xx} A)}{\partial x} dx \quad (4.2.1-11)$$

Because $\frac{D}{Dt} = \frac{\partial}{\partial t} + u \frac{\partial}{\partial x}$ and $\frac{D\rho}{Dt} + \frac{\rho}{A} \frac{DA}{Dt} + \rho \frac{\partial u}{\partial x} = \eta M \theta$, if the cross sectional

area $A \neq 0$, it may be derived to

$$\rho \frac{Du}{Dt} = \frac{\partial(\sigma_{xx})}{\partial x} + \frac{\sigma_{xx}}{A} \frac{\partial A}{\partial x} \quad (4.2.1-12)$$

Energy Balance Equation: the rate of change of energy is equal to the summation of Sources and Convection. The source is the sum of heat energy, mechanical work, chemical potential energy, and energy due to chemical reaction mass.

$$\text{Rate of change} = \frac{\partial}{\partial t} \left[m \left(e + \frac{1}{2} u^2 \right) \right] = dx \frac{\partial}{\partial t} \left[A \rho \left(e + \frac{1}{2} u^2 \right) \right] \quad (4.2.1-13)$$

where e is the internal energy.

Convection=

$$-\left\{ \rho A u \left(e + \frac{1}{2} u^2 \right) \right\} + \frac{\partial}{\partial x} \left[\rho A u \left(e + \frac{1}{2} u^2 \right) \right] dx + \rho A u \left(e + \frac{1}{2} u^2 \right) = -dx \frac{\partial}{\partial x} \left[\rho A u \left(e + \frac{1}{2} u^2 \right) \right] \quad (4.2.1-14)$$

where q_x = heat transferred per unit time through a unit area

$$\text{Heat} = -\frac{\partial(q_x A)}{\partial x} dx \quad (4.2.1-15)$$

$$\text{Rate of mechanical work} = \text{force} \times \text{velocity} = \frac{\partial}{\partial x}(\sigma_{xx} Au) dx \quad (4.2.1-16)$$

$$\text{Energy due to chemical reaction mass} = \left(e + \frac{1}{2}u^2\right) \frac{\partial m^r}{\partial t} = Adx\eta M\theta \left(e + \frac{1}{2}u^2\right) \quad (4.2.1-17)$$

Therefore the energy balance equation becomes

$$\begin{aligned} & dx \frac{\partial}{\partial t} \left[\rho A \left(e + \frac{1}{2}u^2 \right) \right] \\ & = -dx \frac{\partial}{\partial x} \left[\rho u A \left(e + \frac{1}{2}u^2 \right) \right] - \frac{\partial(q_x A)}{\partial x} dx + \frac{\partial}{\partial x}(\sigma_{xx} Au) dx \\ & + Adx\eta M\theta \left(e + \frac{1}{2}u^2 \right) + Adx\eta M\theta u \end{aligned} \quad (4.2.1-18)$$

which can be simplified for the case $A \neq 0$, then we may obtain the energy balance equation

$$\rho \frac{De}{Dt} = -\frac{\partial q_x}{\partial x} - \frac{q_x}{A} \frac{\partial A}{\partial x} + \sigma_{xx} \frac{\partial u}{\partial x} + M\eta\theta u \quad (\text{where } A \neq 0). \quad (4.2.1-19)$$

Therefore, summary of equation, without any chemical reaction and heat transfer are given below:

$$\text{Mass conservation: } \frac{\partial}{\partial t}[\rho A] + \frac{\partial}{\partial x}(\rho u A) = 0 \quad (4.2.1-20)$$

$$\text{Linear Momentum Balance: } \rho \frac{Du}{Dt} = \frac{\partial(\sigma_{xx})}{\partial x} + \frac{\sigma_{xx}}{A} \frac{\partial A}{\partial x} \quad (4.2.1-21)$$

$$\text{Phase Transition: } \frac{D^P \gamma}{Dt} = \sum_{m \neq p} \left(\frac{{}^m \mathcal{V}_{m \rightarrow p}}{\Delta G_{m \rightarrow p}} - \frac{{}^p \mathcal{V}_{p \rightarrow m}}{\Delta G_{p \rightarrow m}} \right) \frac{\partial \bar{e}}{\partial t} \quad (4.2.1-22)$$

$$\frac{D^P \gamma}{Dt} = \sum_{m \neq P} ({}^m \mathcal{V}_{m \rightarrow P} - {}^P \mathcal{V}_{P \rightarrow m}) \quad (4.2.1-23)$$

$$\text{Energy Balance Equation: } \rho \frac{De}{Dt} = \sigma_{xx} \frac{\partial u}{\partial x} \quad (4.2.1-24)$$

4.2.2 Reduced Model with Changing Cross-Section Area in the Nose Region

1D impact and penetration models with changing cross-section area are developed to describe the penetration velocity profile during the short duration right after the impact. Lock density assumption will be applied here.

4.2.2.1 *Reduced Model with Changing Cross-Section Area in the Nose Region with the constant lock density assumption*

Constitutive relation: It is assumed that the locked density ρ_l (Figure 2-6) can be determined by the Hugoniot diagram for the projectile corresponding to the striking velocity or a function of the striking velocity. As a second approximation, one can consider perturbation of the locking density ρ_l .

The relationship between the stress deviator and the deviator of the rate of deformation is assumed to be elastic-plastic. Thus,

$$\sigma'_{xy} = \dot{\sigma}_{xx} - \dot{\sigma}_{yy} = \frac{4}{3} G \left(\frac{\partial u}{\partial x} \right) = 2GD'_{xy} \quad (4.2.2.1-1)$$

Equation (4.2.2.1-1) is under the conditions $\sigma_{xx} - \sigma_{yy} \leq \bar{y}$ and $P < P_1$, where D'_{xy} is the rate of deformation is assumed to be elastic-plastic. P is the pressure at some location in the projectile. P_1 is a fixed pressure that depends on the material. The constraint $P < P_1$ is introduced to account for an increase in the yield stress behind a shock front in the plastic region.

When the projectile material is subjected to a shock loading, the yield stress can significantly increase behind the shock front and later return to the value of Y , or its corrected value due to strain hardening in a short interval. The resulting plastic work due to increased value of Y can lead to a significant increase in the temperature. One of the mechanisms of taking the material to the phase transition is through this heating. Armstrong *et al* explained that the increase in the temperature is due to dislocation dynamics. The dislocation pile-up avalanche model of Armstrong is a model, which can explain the experimentally observed increase in temperature due to plastic work. The other models underpredict the temperature increase. The dislocation pile-up increases the yield stress in a short region behind the shock front and is followed by plastic flow and a relaxation of the dislocations that lowers the yield stress. This increase in yield stress is reported to be a factor in the range 3~4. Because the measurements techniques immediately behind the shock front, it is possible that a transient yield stress increase can be increased by a factor that can be larger than 3 or 4. In this work, the usual continuum based yield condition is modified to account for the increase in yield stress behind the shock front.

$$\text{When } P > P_1, Y^S = Y_0 \left(-\frac{P}{P_1} \right) \hat{a} \quad (4.2.2.1-2)$$

and is followed by an evolution equation for the yield stress.

$$\dot{Y}^S + \hat{a}Y^S = \hat{a}(Y_0 + a_{s_{rr}} \epsilon'_{xy}) \quad (4.2.2.1-3)$$

where \hat{a} is a material constant.

For a special case of one-dimensional strain in the x direction of the x-y-z coordinate system, the yield condition at $t=t_0$ is

$$\left| \frac{\sigma_{xx} + 2\sigma_{yy}}{3} \right| > P_1 \quad (\text{at } t=t_0) \quad (4.2.2.1-4)$$

At $t>t_0$, equation (4.2.2.1-3) is solved to obtain

$$Y^S = \left[Y_0 \left(-\frac{P}{Y} \right) \hat{a} - Y_0 \right] e^{-\hat{a}(t-t_0)} + Y_0 + a_{s_{rr}} \epsilon'_{xy} \quad (4.2.2.1-5)$$

if strain hardening is not considered by $a_{s_{rr}} = 0$.

Kinematics: In the plastic region, the equation of conservation of mass is

$$\frac{\partial}{\partial t}(\rho A) + \frac{\partial}{\partial x}(\rho u A) = 0 \quad (4.2.2.1-6)$$

This equation assumes that there is only one phase initially and chemical potential is zero. A is the cross-section area. Velocity u represents the velocity profile within the projectile. Because of the locking assumption following the boundary of the shock wave, $\rho=\rho_l$. Thus

$$\frac{\partial}{\partial t}(A) + \frac{\partial}{\partial x}(uA) = 0 \quad (4.2.2.1-7)$$

It is assumed that the deformed projectile maintains the conical shape.

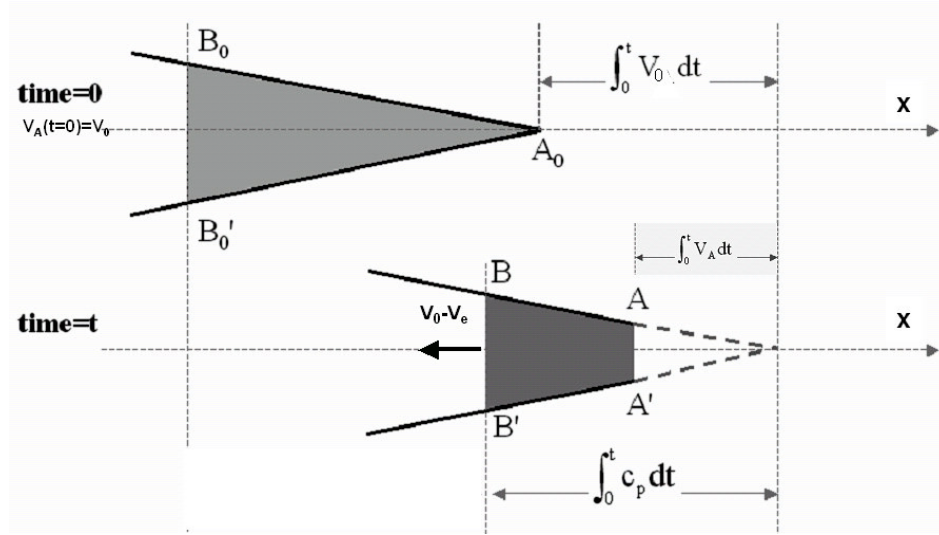


Figure 4-5. 1D model of changing cross-section area in the nose region during the initial stages of penetration (lock density is constant ρ_l).

Mass Conservation: In the region AA'BB', the conservation of mass equation is given by equation (4.2.2.1-6). If the conical shape is maintained (assumption), then the radius of the cross section is proportional to x and the cross sectional area is proportional to x^2 . Then

$$A(x,t) = \beta_2 x^2 \hat{A}_0(t) \quad (4.2.2.1-8)$$

The velocity u is assumed by

$$u = u_1(t)g(x) + \frac{f(t)}{A(x,t)} \quad (4.2.2.1-9)$$

The second term in equation (4.2.2.1-9) results from the fact that any product uA that is equal to only a function of t yields zero when differentiated with respect to x .

By substituting equation (4.2.2.1-9) in equation (4.2.2.1-7), we obtain

$$\beta_2 x^2 \frac{d\hat{A}_0(t)}{dt} + \frac{\partial}{\partial x} [\beta_2 x^2 \hat{A}_0 u_1(t) g(x)] = 0 \quad (4.2.2.1-10)$$

A solution is obtained when $u_1(t)=u_0$ and $g(x)=x$, thus

$$\beta_2 x^2 \left(\frac{d\hat{A}_0(t)}{dt} + 3\hat{A}_0 u_0(t) \right) = 0 \quad (4.2.2.1-11)$$

From equation (4.2.2.1-11), we obtain

$$\hat{A}_0(t) = A_1 e^{\bar{g}t} \quad (4.2.2.1-12)$$

and

$$u_0 = -\frac{\bar{g}}{3} \quad (4.2.2.1-12)$$

Then,

$$u(x) = \frac{f(t)}{A} - \frac{\bar{g}}{3} x \quad (x \neq 0) \quad (4.2.2.1-13)$$

$$A = A_1 e^{\bar{g}t} \beta_2 x^2 \quad (x \neq 0) \quad (4.2.2.1-14)$$

This solution is valid for

$$\int_0^t V_A dt \leq \int_0^t C_P dt \leq L_1 \quad (4.2.2.1-15)$$

Because $x=0$ is in the $f(t)=0$, at

$$x = V_0 t - \int_0^t V_A dt \quad \text{and} \quad u = V_0 - V_A,$$

Therefore, we may obtain \bar{g} and $u(x)$ with

$$\bar{g} = \frac{V_0 - V_A}{V_0 t - \int_0^t V_A dt} \quad (4.2.2.1-16)$$

$$u(x) = \frac{V_0 - V_A}{V_0 t - \int_0^t V_A dt} x \quad (4.2.2.1-17)$$

As needed in the momentum equation Du/Dt is now derived

$$\frac{\partial u}{\partial t} = \frac{\left(V_0 t - \int_0^t V_A dt \right) (-\dot{V}_A) - (V_0 - V_A)^2}{\left(V_0 t - \int_0^t V_A dt \right)^2} x \quad (4.2.2.1-18)$$

$$\text{Let } u \frac{\partial u}{\partial x} = \left(\frac{V_0 - V_A}{V_0 t - \int_0^t V_A dt} \right)^2 x \quad (4.2.2.1-19)$$

$$\frac{Du}{Dt} = x \left(-\frac{\dot{V}_A}{F_1(V_A)} \right) \quad (4.2.2.1-20)$$

where $F_1(V_A) = V_0 t - \int_0^t V_A dt$.

Because of high striking velocity (1200-1500m/sec), V_e is assumed to be very small compared to the particle velocity in the plastic-locked region AA'BB' and thus V_e is assumed to zero and $\rho_e = \rho_0$ (consistent with the assumption of small displacement in the elastic region). The mass contained in the cone OBB', initially with density ρ_0 is now contained in the region AA'BB' with a locked constant density ρ_l . Then let $\alpha = \rho_0 / \rho_l$, we have

$$\frac{\pi}{3} \rho_0 \left(\int_0^t c_p dt \right)^3 \tan^2(\theta) = \frac{\pi}{3} \rho_l \left(\left(\int_0^t c_p dt \right)^3 - \left(\int_0^t \hat{V}_A dt \right)^3 \right) \tan^2(\theta) \quad (4.2.2.1-21)$$

$$(\alpha - 1) \left(\int_0^t c_p dt \right)^3 = - \left(\int_0^t \hat{V}_A dt \right)^3 \quad (4.2.2.1-22)$$

The momentum balance equation: is given by

$$\rho A \frac{Du}{Dt} = \frac{\partial}{\partial xx} [\sigma_{zz} A] \quad (4.2.2.1-23)$$

This equation is now integrated from BB' to AA'. With the cavity expansion theory, it can be extended as

$$\int_{\int_0^t c_p dt}^{\int_0^t V_A dt} \rho_l A_1 e^{\bar{g}t} \beta_2 x^2 \left(-x \frac{\dot{V}_A}{F_1(V_A)} \right) dx = \sigma_{zz} A|_B - \sigma_{zz} A|_A \quad (4.2.2.1-24)$$

$$A_1 = \pi \left(\int_0^t V_A dt \right)^2 \tan^2(\theta) = A|_A \quad (4.2.2.1-25)$$

$$\sigma_{xx}|_A = -\sigma_R \quad (\sigma_R \text{ is the target resistant force}) \quad (4.2.2.1-26)$$

Then

$$\begin{aligned} & \pi \rho_l \left(\int_0^t V_A dt \right)^2 e^{\bar{g}t} \beta_2 \frac{\dot{V}_A}{F_1(V_A)} \left(-\frac{x^4}{4} \right) \Big|_{\int_0^t c_p dt}^{\int_0^t V_A dt} \tan^2(\theta) \\ & = -\sigma_R \pi \left(\int_0^t c_p dt \right)^2 \tan^2(\theta) - \sigma_{xx}|_B \pi \left(\int_0^t V_A dt \right)^2 \tan^2(\theta) \end{aligned} \quad (4.2.2.1-27)$$

Where c_p can be rewritten from the equation (4.2.2.1-22)

$$\left(\int_0^t c_p dt \right) = \left(\frac{1}{1-\alpha} \right)^{\frac{1}{3}} \int_0^t V_A dt \quad (4.2.2.1-28)$$

With the equation (4.2.2.1-28), (4.2.2.1-27) can be simplified as

$$\rho_l e^{\bar{g}t} \beta_2 \frac{\dot{V}_A}{F_1(V_A)} \frac{1}{4} \left(\int_0^t V_A dt \right)^4 \left(\left(\frac{1}{1-\alpha} \right)^{4/3} - 1 \right) = -\sigma_R \left(\frac{1}{1-\alpha} \right)^{2/3} - \sigma_{xx}|_B \quad (4.2.2.1-29)$$

$\sigma_{xx}|_B$ is now determined from shock jump conditions.

Shock Wave Jump Conditions: shock wave jump conditions are derived as follows:

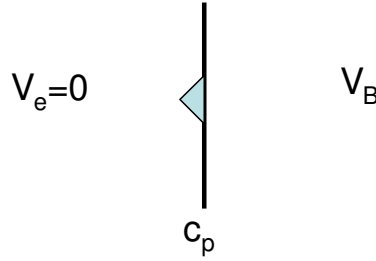


Figure 4-6. Shock wave front. Left side is elastic wave; right side is plastic wave. c_p is the plastic wave propagation speed.

$$\rho_0 c_p = \rho_l (c_p - V_B) \quad (4.2.2.1-30)$$

$$\rho_0 (c_p)(V_B) = -\sigma_{zz}(x_B, t) \quad (4.2.2.1-31)$$

The above two equations can be used to obtain c_p and $\sigma_{xx}|_B$.

$$c_p (\rho_0 - \rho_l) = -\rho_l V_B \quad (4.2.2.1-32)$$

$$c_p \left(1 - \frac{\rho_0}{\rho_l} \right) = V_B \quad (4.2.2.1-33)$$

$$\sigma_{xx}|_{x=x_B} = -\rho_0 c_p^2 (1-\alpha)^2 \quad (4.2.2.1-34)$$

Therefore,

$$c_p = \frac{1}{1-\alpha} \frac{V_0 - V_A}{V_0 - \int_0^t V_A dt} \left(V_0 t - \left(\frac{1}{1-\alpha} \right)^{\frac{1}{3}} \int_0^t V_A dt \right) \quad (4.2.2.1-35)$$

$$\sigma_{xx}|_B = \rho_0 \frac{(V_0 - V_A)^2}{\left(V_0 t - \int_0^t V_A dt \right)^2} \left(V_0 t - \left(\frac{1}{1-\alpha} \right)^{\frac{1}{3}} \int_0^t V_A dt \right)^2 \quad (4.2.2.1-36)$$

Then substitute (4.2.2.1-29) into (4.2.2.1-36), the final equation for V_A is obtained

$$\begin{aligned} \rho_l e^{\bar{g}t} \beta_2 \frac{\dot{V}_A}{F_1(V_A)} \frac{1}{4} \left(\int_0^t V_A dt \right)^4 \left(\left(\frac{1}{1-\alpha} \right)^{4/3} - 1 \right) \\ = -\sigma_R \left(\frac{1}{1-\alpha} \right)^{\frac{2}{3}} - \rho_0 \frac{(V_0 - V_A)^2}{(F_1(V_A))^2} \left(V_0 t - \left(\frac{1}{1-\alpha} \right)^{\frac{1}{3}} \int_0^t V_A dt \right)^2 \end{aligned} \quad (4.2.2.1-37)$$

Equation (4.2.2.1-37) is an ordinary differential equation that can be solved numerically.

Phase Transition in the Plastic Region: The velocities of penetration are determined from the momentum equation. We assume a linear variation of the pressure with respect to x direction in the plastic region. This means,

$$P(x, t) = P(x_B, t) + \frac{P(x_A, t) - P(x_B, t)}{x_A - x_B} (x - x_B) \quad (4.2.2.1-38)$$

The rate of work done by the shock compression in the plastic region is given by

$$\dot{W}(x, t) = \sigma_{xx} \dot{\epsilon}_{xx} \quad (4.2.2.1-39)$$

In this work, a simplified high-strain-rate phase-transition model is used. If we assume that only two phases can coexist, the mass fraction for the second phase is given by γ , and the mass fraction for the first phase is $(1 - \gamma)$.

$$\rho \dot{\gamma} = \frac{1 - \gamma}{\Delta G_{1 \rightarrow 2}} \dot{W} \quad (4.2.2.1-40)$$

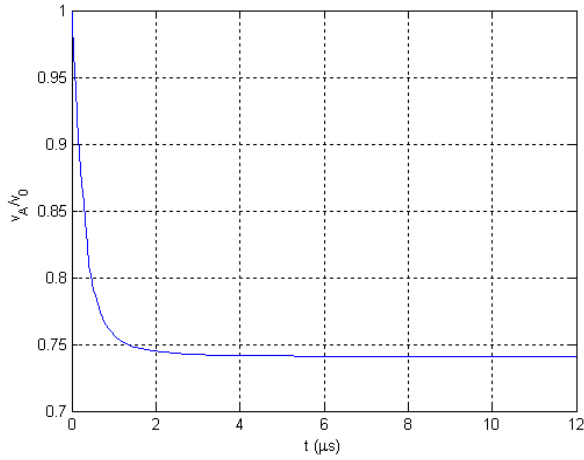


Figure 4-7. Time variations of the penetration velocity $v_A(t)$ for the steel projectile into aluminum target.

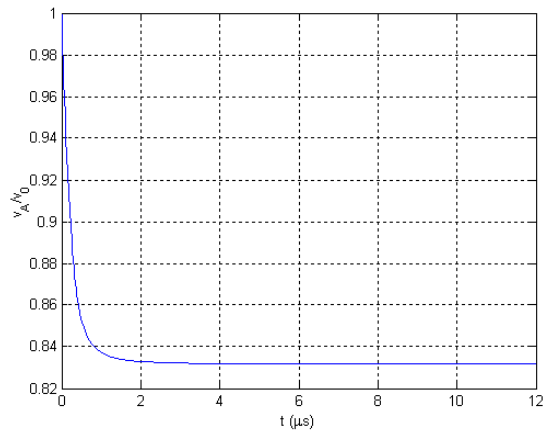


Figure 4-8. Time variations of the penetration velocity $v_A(t)$ for tungsten projectile into steel target.

4.2.2.2 Example Studies

A Steel Projectile into an Aluminum Target: To study the new model, a steel projectile and an aluminum target are selected as used in the work by Hanagud and Ross. The blunting of the projectile is studied. The conical nose is of diameter ¼ inch and slant surface of angle 30° ($\alpha=30^\circ$). Some material constants are listed as follows. For the projectile, $\rho_0 = 7850 \text{ kg/m}^3$, $Y^p = 470 \text{ MPa}$, $E=205\text{GPa}$ (Young's modulus), $E^p = 10 \text{ GPa}$ (strain hardening modulus), $\Delta G=10^{13} \text{ J/kg/sec}$. For the aluminum target, we have $\rho_{t0} = 2768 \text{ kg/m}^3$, $\rho_{t1p} = 4000 \text{ kg/m}^3$, $Y^t = 386.1 \text{ MPa}$, $E^t=68.95 \text{ GPa}$ (Young's modulus), $E^{tt} = 2.827 \text{ GPa}$ (strain hardening modulus). In the following simulations, the initial impact velocity is 1500 m/sec. The time-dependent change penetrator velocity is simulated. The results are shown in Figure 4-7. The time variation of the ratio of the density in the elastic region over the locked density in the plastic region is also presented in Figure 4-7. As shown, the penetration velocity is reduced from 1500 m/sec to around 1110 m/sec in 12 μ s. The penetration depth is around 13.5 mm. 1D model yields a very rapid reduction of the penetration speed in the initial penetration duration, therefore leads to a larger penetration depth.

A Tungsten Projectile into an Armor Steel Target: Material constants for tungsten alloy are $\rho_0 = 17,300 \text{ kg/m}^3$, $Y^p = 1.8 \text{ GPa}$, $E=327.5 \text{ GPa}$ (Young's modulus), $E^p = 163.75 \text{ GPa}$ (strain hardening modulus), $\Delta G=10^{13} \text{ J/kg/sec}$. For Armor steel, we have $\rho_{t0} = 7861 \text{ kg/m}^3$, $\rho_{t1p} = 9000 \text{ kg/m}^3$ (selected), $Y^t = 1.2 \text{ GPa}$, $E^t = 210 \text{ GPa}$ (Young's modulus), $E^{tt} = 3.1 \text{ GPa}$ (strain hardening modulus). In the following simulations, the initial impact velocity is 1500 m/sec. The results are shown in Figure 4-8. As shown, the

penetration velocity is reduced from 1500 m/sec to around 1250 m/sec in 12 μ s. The penetration depth is around 15 mm.

A Steel Projectile into a (Mg_{0.92},Fe_{0.08})SiO₃Perovskite Target: In this case, we consider a hard target. The material perovskite with composition of (Mg_{0.92},Fe_{0.08})SiO₃ (x almost 0.1) [Gong--2003], in the orthorhombic crystal structure is generally accepted to be the dominant phase of the Earth's lower mantle. Material constants for (Mg_{0.92},Fe_{0.08})SiO₃ Perovskite $\rho_{t0} = 4190 \text{ kg/m}^3$, $\rho_{tip} = 5500 \text{ kg/m}^3$ (selected), $Y^t = 60 \text{ MPa}$, $E^t = 260.09 \text{ GPa}$ (Young's modulus), $E^{tt} = 13 \text{ GPa}$ (strain hardening modulus). In the following simulations, the initial impact velocity is 1500 m/sec. The time-dependent penetrating velocity is shown in Figure 4-9. As shown, the penetration velocity is reduced from 1500 m/sec to around 1230 m/sec in 12 μ s. The phase transitions are calculated according to equation (4.2.2.1-23). The mass fraction of phase 2 as a function of x and t is presented in Figure 4-10a, time variations of mass fraction of phase 2 at locations $x=x_A$ and $x_A - 0.5\text{mm}$ are presented in Figure 4-10b; and the profiles of mass fraction of phase 2 at particular times $t = 0.055$ and 12 μ s are presented in Figure 4-10c. It is observed that as time increases, the phase transition takes place very rapidly and then tends to a quasi-steady state. Closer to the nose tip (x_A), there exists more phase transition as indicated by larger values of mass fraction of phase 2.

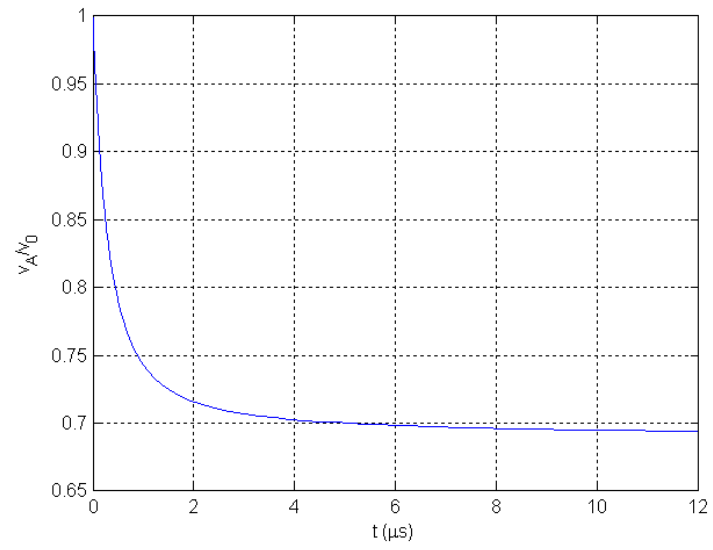


Figure 4-9. Time variations of the penetration velocity $v_A(t)$ for steel projectile into (Mg0.92,Fe0.08)SiO3 Perovskite target

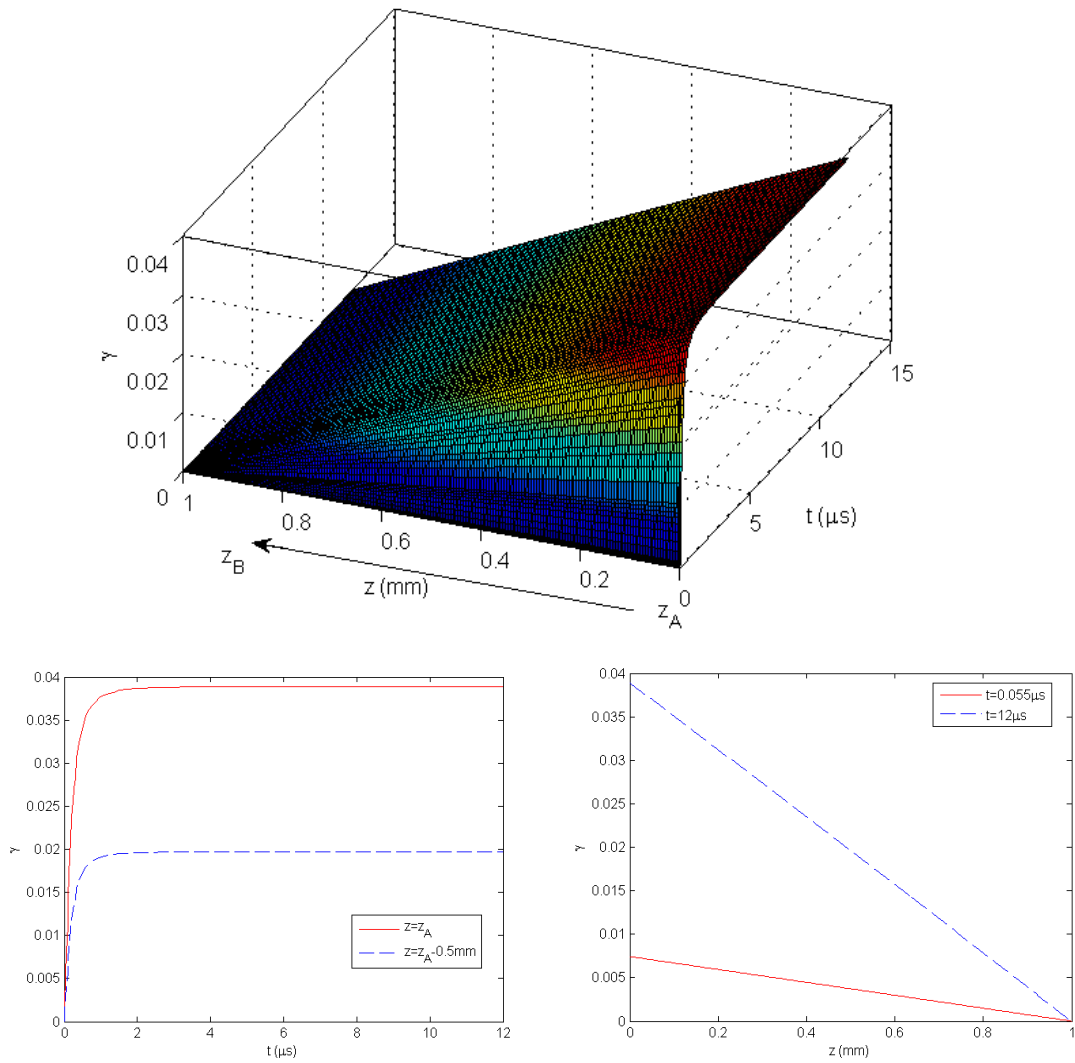


Figure 4-10. The time variations of the phase transition profile for steel projectile into $(\text{Mg}_{0.92}, \text{Fe}_{0.08})\text{SiO}_3$ Perovskite target. (a) Mass fraction of phase 2 as a function of x & t ; (b) Time variations of mass fraction of phase 2 at locations $x=x_A$ & $x_A - 0.5\text{mm}$; and (c) Profile of mass fraction of phase 2 at $t = 0.055$ and $12 \mu\text{s}$.

CHAPTER 5

EOS, MAGNETISM AND PHASE TRANSITION FOR IRON

The physical properties of iron, equation of state, magnetism and phase transition, have been studied by using ab initio methods during the past thirty years. For example [Wang--1985], at ambient conditions, bcc is predicted to be the stable structural phase with a ferromagnetic order; fcc is stable at higher temperatures and low pressures but of a nonmagnetic order...etc. Many scientists investigated iron in different areas and use different ab initio methods. However, there is no agreement on which approximation would provide the best prediction, and so far, there is no any decision about which approximation could be the best selected for the studies of alloys.

In this chapter, studies are to complete a thorough study on structural phases of iron, magnetic orders and phase transitions. The information of structural and magnetic phase transitions of iron is then incorporated into the prediction of the equation of state of iron. A thorough investigation also includes the studies of various approximation methods in DFT based on plane waves or modified plane waves. The investigations include various choices of exchange correlation functionals, basis functions and pseudopotentials. The studies also include the hubbard-U method to improve the description of in transition metals like iron. All the predictions are compared with the experimental measurements and previous theoretical studies. From these results, a best set of approximations of ab initio methods are found for the iron and are used for the

studies of steel alloys in Chapter 6. Also, the obtained phase transition, EOS and magnetic orders will be used as a basis to study the effects of species considered in steels.

In order to predict the EOS of iron with high precisions, the structural and magnetic phase transitions of iron have to be considered. For simple metals like iron, there are three major structural phases: bcc, fcc and hcp. For each structural phase, we considered three possible magnetic orders: ferromagnetic, antiferromagnetic and non-magnetic phases. Therefore, for each structural phase, a first task is to identify its magnetic order at the ground state by using the principle of minimum energy. Then, the next task is to determine structural phase transitions, including bcc, fcc and hcp, with their identified magnetic phases, including ferromagnetic, antiferromagnetic and non-magnetic orders. Finally, the information of the structural and magnetic phase transitions was incorporated into the construction of the EOS of iron.

5.1 Material Characterization by using Ab Initio Methods

5.1.1 Ab initio EOS for a Crystalline Solid

The internal energy $e(v,T)$ of the crystalline solid can be obtained from the three contributions under the assumption of negligible electro-phonon interactions. These three contributions are the cold-curve energy $e_c(v, T=0)$, which is the energy of the system with electrons at absolute zero temperature and ions in their crystallographic sites associated with some fixed volume v , the thermal energy from the ions $e_l(v,T)$, which has each ion vibrating at a fixed average position, and the thermal energy from the electrons $e_e(v,T)$,

where T is the temperature [Godwal—1979 & Swift--2001]. In the formulation, the total internal energy can be written into

$$e(v, T) = e_c(v, T = 0) + e_l(v, T) + e_e(v, T) \quad (5.1-1)$$

The electronic ground state energy $e_c(v, T=0)$ is the zero point energy of the crystalline system. It is obtained from quantum mechanical calculations as the zero-temperature frozen-ion isotherm of the system for a given lattice parameter (a measure of the specific volume of the system).

The electron thermal energies $e_e(v, T)$ are from the thermal excitation of electrons from their ground states. It is calculated from electron band structure based on the Fermi-Dirac statistics.

From Fermi-Dirac statistics,

$$\int_{-\infty}^{+\infty} f_F(\epsilon, T) n(\epsilon) d\epsilon = N \quad (5.1-2)$$

$$f_F(\epsilon, T) = \frac{1}{e^{\frac{\epsilon - \mu}{kT}} + 1} \quad (5.1-3)$$

where $f_F(\epsilon, T)$ is the probability of occupation of a fermions state of energy ϵ at temperature T . Base on equation (5.1-3), the chemical potential $\mu(T)$ can be found, by an iterative inversion algorithm. Once $\mu(T)$ is obtained, the expectation value of the electronic energy is obtained as follows.

$$e_e(v, T) = \int_{-\infty}^{+\infty} \epsilon f_F(\epsilon, T) n(\epsilon) d\epsilon \quad (5.1-4)$$

The contribution of lattice thermal energies $e_l(v,T)$ comes from the thermal excitation of ions, which is calculated from phonon modes of the lattice [Baroni—2001]. $e_l(v,T)$ is obtained from $E_l(T)$ by normalizing to three modes per atom and using a proper interpolation, where $E_l(T)$ is the lattice thermal energy with the phonon modes, which has

$$E_l(T) = \int_0^{+\infty} \hbar \omega g(\omega) f_b(\omega, T) d\omega \quad (5.1-5)$$

Where

$$f_b(\omega, T) = \frac{1}{e^{\frac{\hbar \omega}{KT}} - 1} + \frac{1}{2} \quad (5.1-6)$$

In equation (5.1-6), $f_b(\omega, T)$ means, at some specific temperature T , the probability of the occupation of a Boltzman state of energy $\hbar \omega$.

With the three contributions to the total free energy, Helmholtz's free energy can be written as $A(v,T) = e_c(v,T=0) + A_e(v,T) + A_l(v,T)$, where the cold curve energy $e_c(v,T=0)$ is obtained from quantum mechanical calculations. The electronic thermal free energy $A_e(v,T)$ is $A_e(v,T) = e_c(v,T) - e_c(v,T=0) - T s_e(v,T)$.

The electronic entropy $s_e(v,T)$ is given by using Mermin theorem [Mermin—1965]

$$s_e(v,T) = -k \int_{-\infty}^{+\infty} [f_F(\epsilon, T) \ln f_F(\epsilon, T) + (1 - f_F(\epsilon, T)) \ln (1 - f_F(\epsilon, T))] \eta(\epsilon) d\epsilon \quad (5.1-7)$$

The lattice thermal free energy is given by

$$A_l(v,T) = KT \int_0^{+\infty} \ln \left(2 \sinh \left(\frac{\hbar \omega}{KT} \right) \right) g(\omega) d\omega \quad (5.1-8)$$

Therefore, Helmholtz's free energy $A(v,T)$ can be calculated based on the above formulations. The thermodynamically complete EOS can be obtained by

$$P(v,T) = -\frac{\partial A(v,T)}{\partial v} \quad (5.1-9)$$

5.1.2 Phase transitions & EOS

For multi structural and magnetic phases, the metastable surface between the phase-1 and phase-2 is defined by first assuming pressure and temperature equilibrium: $P_1=P_2=P$ and $T_1=T_2=T$. With this assumption, the equilibrium phase boundary can be found by using $A_1(P,T)=A_2(P,T)$ [Jonathan—1997], where 'A' is the total free energy, which determines a phase transition line in P-T phase diagram. A EOS with phase transitions is then constructed after obtaining the phase diagram.

For the case of iron, three structural phases, i.e. bcc, fcc and hcp, with magnetic orders, i.e. FM, AFM, and NM, are studied from first principles, to predict a precise EOS that includes the structural and magnetic phase transition information, in the range of selected pressures at ground state. Therefore, ground state calculations are first implemented for every structural phase with every possible magnetic order. Then, phase transition at ground state is predicted by using the principle of minimum energy. EOS at $T=0K$ is constructed by incorporating phase transitions into the ground state energy as a function of density (or volume).

5.2 Approximations & Convergences in Ab Initio Methods

Approximations: Various approximations can be used for the approximations in the following categories: (1) Exchange-correlation functional, used to account for the exchange and correlations in the correlated electronic system. We have the choices among L(s)DA, GGA (PW91 or PBE), etc.; (2) Basis functions, plane waves with or without the option of augmentation (PAW) can be chosen from; and (3) Various pseudopotentials which can be used account for the frozen core and valence electrons, like ultrasoft or PAW pseudopotential. For the strong Coulomb interactions in transition metals like iron, Hubbard-U method that improves the description of strong correlations between d electrons, will be investigated.

The electron ground states were calculated using the density functional theory in the projector augmented plane-wave pseudopotential implementation using the Vienna ab-initio simulation package VASP (Vienna ab initio simulation package) [G.Kresse & J.Furthmuller--2005]. For an iron atom, with $3d^74s^1$ chosen as valence electrons and the others as core electrons, pseudopotential was generated with cutoff radius of 2.46 Å and 1.302 Å respectively, with a core radius of 2.991 Å for projector operators.

Accuracies & Convergence: In VASP, the electron wave functions of the valence electrons were expanded in a plane-wave basis set for which the amplitudes of each band were optimized to find the ground state. The electron wave functions are calculated explicitly on a discrete grid of locations in k space.

(1) For a periodic system, numerical integrals in real space over the infinite system are replaced by integrals over the finite first Brillouin zone in reciprocal space by virtue

of Bloch's theorem. Such integrals are performed by summing the function values of the integrand at a finite number of points in the Brillouin zone, called the k-point mesh. The generation of the grids and the density of the mesh of k-point that are crucial for the convergence of the results, therefore are included in the convergence tests.

(2) Only a finite number of basis states were used, corresponding to a selected energy cutoff. The selected energy cutoff is 267.907eV, which is the default energy cutoff value in PW91_PAW. In the plane wave basis set, only plane-waves with a kinetic energy smaller than so-called cut-off energy are included in the calculations. In our studies, a constant cut-off energy is selected for all the calculations. The total number of plane wave changes very smoothly if the volume is increased.

(3) To control the precision of the energy calculations, for both ionic and electronic relaxation loops, break conditions which control the decimal precision of the energy can be selected. In other words, when the total free energy change and the band structure energy change between two electronic or ionic steps are smaller than the specified errors in total energy, the relaxation of the electronic or ionic degrees of freedom will be stopped.

Table 5-1 Energy comparison based on KPOINT at the fixed setting ENCUT=267.907ev, EDIFF=E-07 & EDIFFG=E-06 (PW91_PAW)

ENCUT=267.907, EDIFF=E-07 & EDIFFG=E-06		
	Energy (ev/atom)	Volume/atom (a³)
KPOINT=4	-7.738097	10.34
KPOINT=5	-7.711305	10.34
KPOINT=6	-7.724022	10.34
KPOINT=8	-7.723599	10.34
KPOINT=9	-7.725019	10.34

Convergence Tests: We used a bcc NM Fe for the convergence tests. First, for a combination of PW91 and PAW, we have selected Monkroost-Pack mesh of K-points from 4x4x4 to 9x9x9. The precision for the energy control is set to be 10^{-7} (EDIFF) and 10^{-6} eV (EDIFFG) for electronic and ionic steps. A cut-off energy 267.907eV (ENCUT) is selected. Table 5-1 shows the energy comparison of selected structures with respect to various selections of K-point mesh. The lattice and ion equilibrium positions are calculated based on the setting KPOINTS = 9, ENCUT = 267.907 eV and EDIFF = E-07 & EDIFFG=E-06. It can be seen that KPOINTS = 4 gives the lowest energy which means the minimum energy to these k-points selections. As a second choice, KPOINT=6 will be also selected to the future comparison with the Fe-Ni alloy and Fe-Ni-C alloy.

We also investigated the Hubbard-U method based on the previous convergence test. Table 5-2 shows the energy comparison to the KPOINTS. The lattice and ion equilibrium positions are calculated based on the setting KPOINT=11, ENCUT = 267.907ev and EDIFF=E-04 & EDIFFG=E-03. It can also be seen that KPOINT=4 and KPOINT=6 gave the minimum energy to these k-points selections.

Table 5-2. Energy comparison based on KPOINT at the fixed setting ENCUT=267.907ev, EDIFF=E-04 & EDIFFG=E-03. (PW91_PAW)

ENCUT=267.907, EDIFF=E-04 & EDIFFG=E-03		
	Energy (ev/atom)	Volume/atom (a³)
KPOINT=4	-7.641085	10.16
KPOINT=5	-7.535519	10.16
KPOINT=6	-7.547120	10.16
KPOINT=8	-7.535368	10.16
KPOINT=9	-7.539808	10.16

We assumed a transferable convergence control of the combination of PW91 and PAW to other combinations of approximation methods, like a combination of PBE and PAW. The possible combinations of considered are listed in Table 5-3. In the following calculations, first we used a relative lower precision control to predict on the magnetic orders, structural phases and densities (Table 5-3). Then a higher precision control using KPOINTS 9x9x9, EDIEF=10⁻⁷ and EDIEFG=10⁻⁶ was used for the precise prediction on the EOS and phase transition when we obtained a rough prediction on the locus of phase transitions. A comparison for various approximations is given at the end of the chapter. The cutoff energy 267.883 eV is selected for PBE_PAW, PW91_PAW and Hubbard_U with PW91_PAW, which is the default cutoff energy.

Table 5-3. Parameters used in the calculations.

	PBE_PAW	PW91_PAW	Hubbard_U + PW91_PAW
K-point (NxNxN)	5	6	5
EDIFF (1E-n eV)	7	4	7
EDIFFG (1E-n eV)	6	3	6
ENCUT (eV)	267.883	267.883	267.883

5.3 Results & Discussions

5.3.1 Studies of Bcc, Fcc, Hcp Iron and Their Magnetic Phases

5.3.1.1 *Bcc Iron*

The primitive unit cell of bcc iron consists of only one atom, which can be repeated along the three lattice vectors to construct the large size supercell. For collinear magnetic orders, the primitive unit cell can be selected for the nonmagnetic and ferromagnetic cases, but two-atom conventional unit cell has to be selected to substitute the primitive unit cell for antiferromagnetic case because of the opposite spin orders. To guarantee the agreement on the volume of unit cell, the two-atom conventional unit cell of bcc structure is selected for the studies of three magnetic phases. First, the bcc lattice of an initial guess was relaxed to find its equilibrium lattice parameters. Then the volume of the lattice is reduced from the completely equilibrium size (recorded as 100%) to some smaller value with the fixed volume change ratio—1%. A conventional unit cell consisting of two atoms with the unit lattice vectors $[1\ 0\ 0; 0\ 1\ 0; 0\ 0\ 1]$ was used for the calculations for bcc iron. The positions of the two atoms in the unit cell are $[0\ 0\ 0]$ and $[0.5\ 0.5\ 0.5]$. Three types of magnetic orders were considered (Figure 5-1). For various combinations of approximations as listed in Table 5-3, we have implemented the ground state calculations for bcc FM, bcc AFM and bcc NM structures (Figure 5-1).

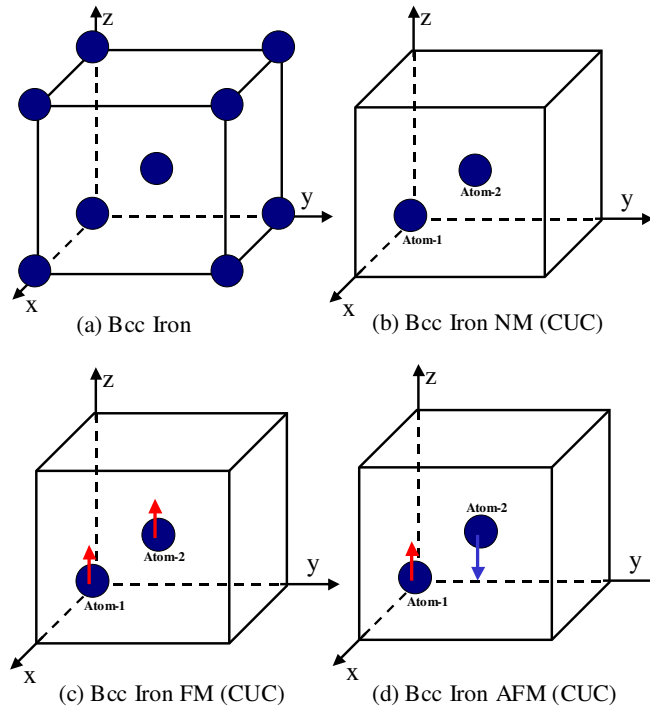


**Figure 5-1. Bcc conventional unit cell and magnetic orientation [001].
CUC=Conventional Unit Cell.**

(1) For the combination of PBE and PAW, the results, including ground state energies and magnitude of the magnetic moments vs. density, are shown in Figure 5-2 and Figure 5-3.

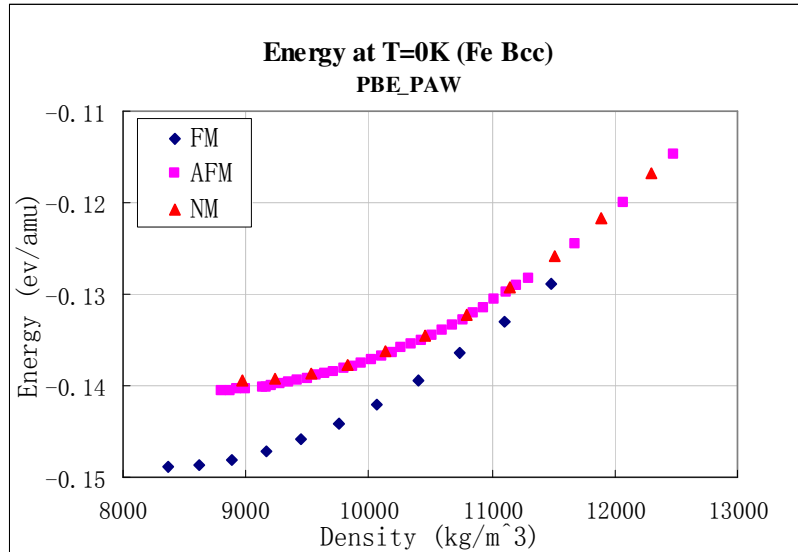


Figure 5-2. Ground state energies of bcc iron vs. density (by PBE with PAW)

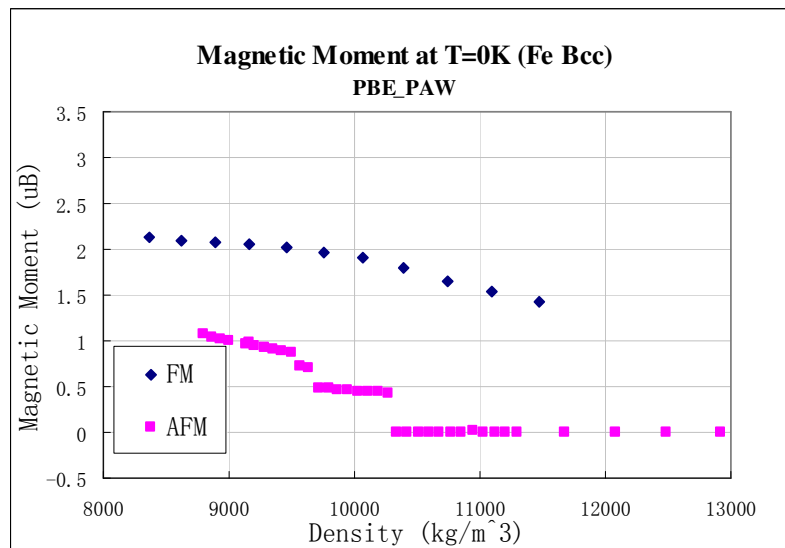


Figure 5-3. Magnitude of the magnetic moments of bcc iron vs. density (by PBE with PAW).

From Figure 5-2 and Figure 5-3, the one among the three possible magnetic orders that gives the lowest energies is the FM order. Therefore, *the bcc iron is of a ferromagnetic phase*. For FM phase, the predicted lattice constant is 2.8094\AA , corresponding to a density of 8365kg/m^3 , which is approximately 1.6% smaller than

experiment [Acet-1994] and approximately 0.6% smaller than the value of 2.827\AA predicted by using the full-potential-linearized-augmented-plane-wave method (FP_LAPW) within the density functional theory and the generalized gradient approximation (GGA) [Clatterbuck--2002]. For FM phase, the predicted magnetic moments first has a gradual reduction from $2.128\mu_B$ to $1.2\mu_B$, as the pressure increases from 0, corresponding to density increasing from 8365kg/m^3 to $13,000\text{ kg/m}^3$; then, a sudden reduction to $0\mu_B$ after the pressure further increases. The predicted magnitude of the magnetic moment at zero pressure, $2.128\mu_B$, has an excellent agreement with the experimental value of $2.12\mu_B$ [Jephcoat--1986].

(2) For the combination of PW91 and PAW, the results are shown in Figure 5-4 and Figure 5-5. Similarly, from Figure 5-4 and Figure 5-5, the most stable magnetic phase at the ground state is found to be the bcc FM. For FM phase, the predicted lattice constant is 2.8085\AA , corresponding to a density of 8373 kg/m^3 , which is approximately 1.6% smaller than experiment [Acet-1994]. For FM phase, at the equilibrium lattice constants, the magnetic moments are predicted as $2.101\mu_B$, which is slightly smaller (0.9%) than the experimental value ($2.12\mu_B$) [Jephcoat--1986].

(3) For the combination of PW91 and PAW with Hubbard-U of $U=4.5$ and $J=1$, the results are shown in Figure 5-6 and Figure 5-7. This combination also predicts that the bcc iron is of FM phase at the ground state. For FM phase, the predicted lattice constant is 2.8880\AA which corresponds to a density of 7648kg/m^3 , which is approximately 1.15% larger than the experimental data [Acet-1994]. For FM phase, at the equilibrium lattice constants, the magnetic moments are predicted as $2.838\mu_B$, which gives an overestimation about 33.8%.

(4) We also investigated Hubbard-U method with various U values, in the framework of PW91 and PAW. The values of 'U' change from 4.5 to 6.5. The comparisons for various U are shown in Figure 5-8. We can see that as U increases, the predicted density at the equilibrium lattice constants decreases. As noted, U = 4.5 gives the best prediction of the density. Therefore, we chose U =4.5 and J =1 for the rest of calculations if Hubbard-U method is used.

The summary of investigations on the bcc iron based on various combinations of approximations is listed in Table 5-4. In summary, all the three combinations show a prediction that agrees with the experiment [Jephcoat--1986] [Acet--1994], which for the bcc iron, the ferromagnetic phase is the most stable phase at the ground state. Among these combinations, with Hubbard_U, it gives the best prediction to density. However, without Hubbard_U, we have a better prediction on the magnetic moment. Therefore, we will expect that the Hubbard_U method will improve the prediction of the density of the bcc alloys. However, for prediction of magnetic orders of bcc alloys, without the inclusion of the Hubbard-U method, might give a better choice.

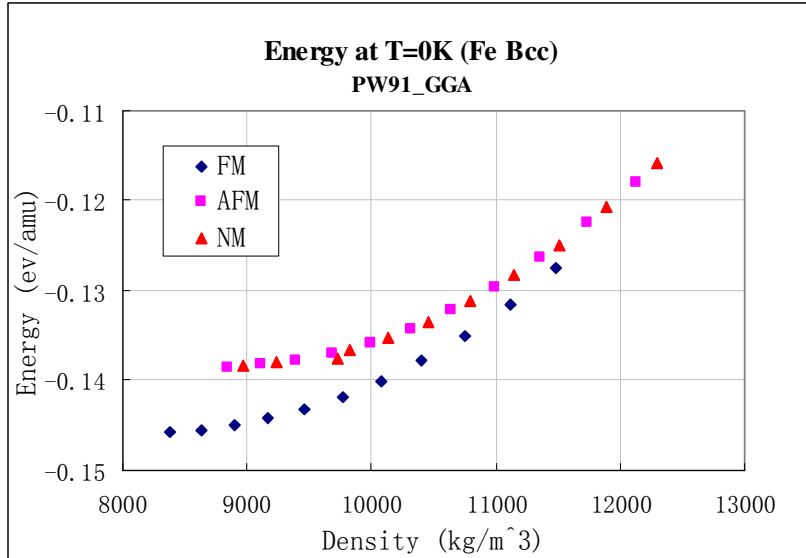


Figure 5-4. Ground state energies of bcc iron vs. density (by PW91 with PAW)

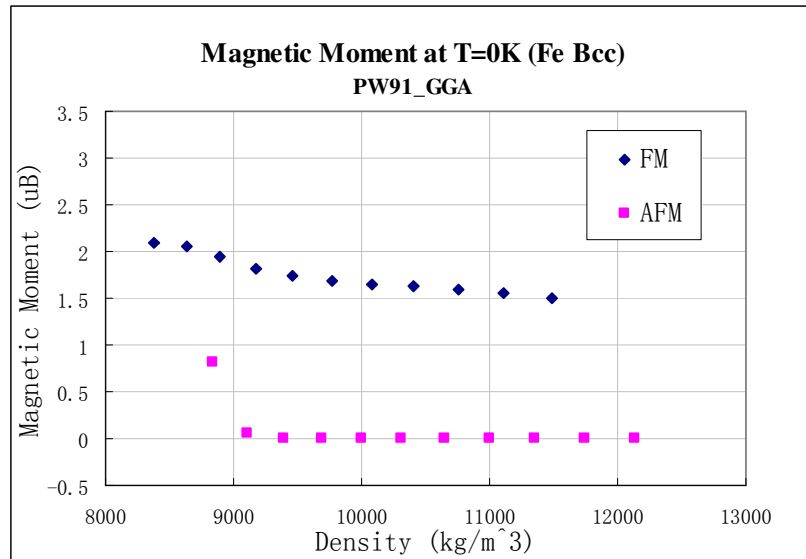


Figure 5-5. Magnitude of the magnetic moments of bcc iron vs. density (by PW91 with PAW).

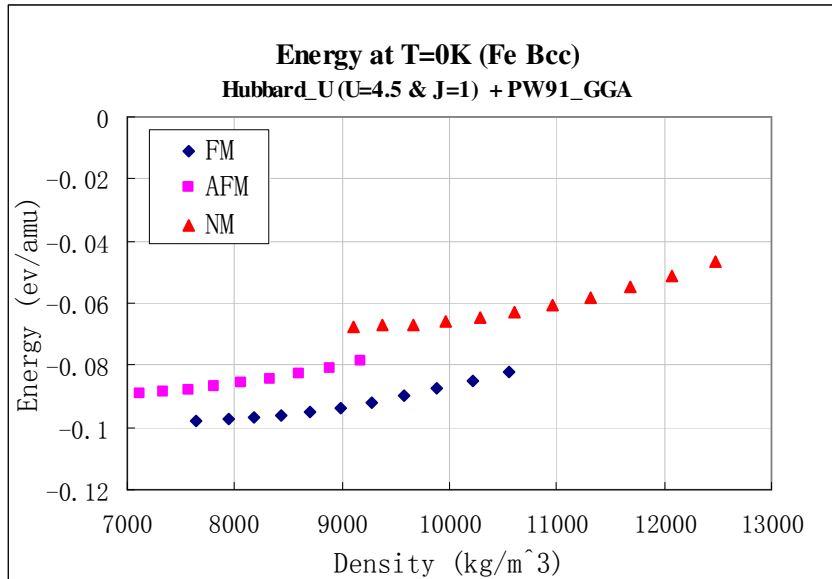


Figure 5-6. Ground state energies of bcc iron vs. density (by PW91 with PAW and Hubbard_U [U=4.5 & J=1]).

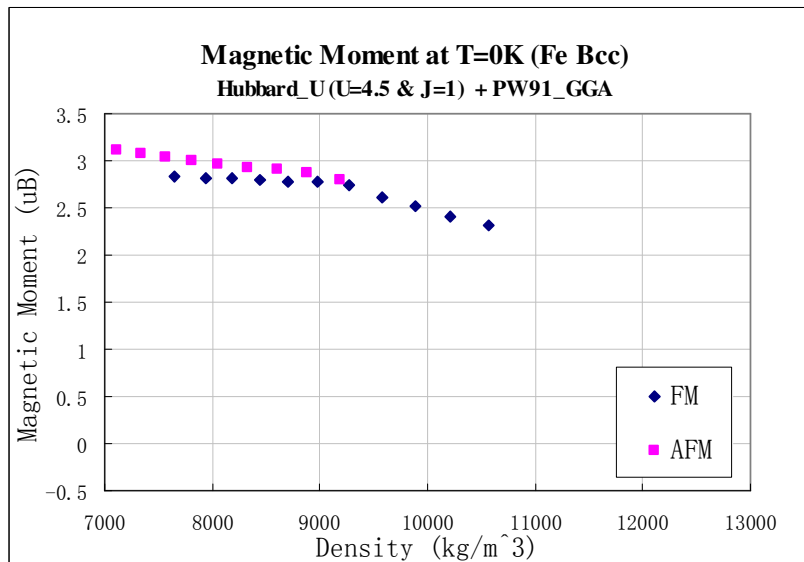


Figure 5-7. Magnitude of the magnetic moments of bcc iron vs. density (by PW91 with PAW and Hubbard_U [U=4.5 & J=1]).

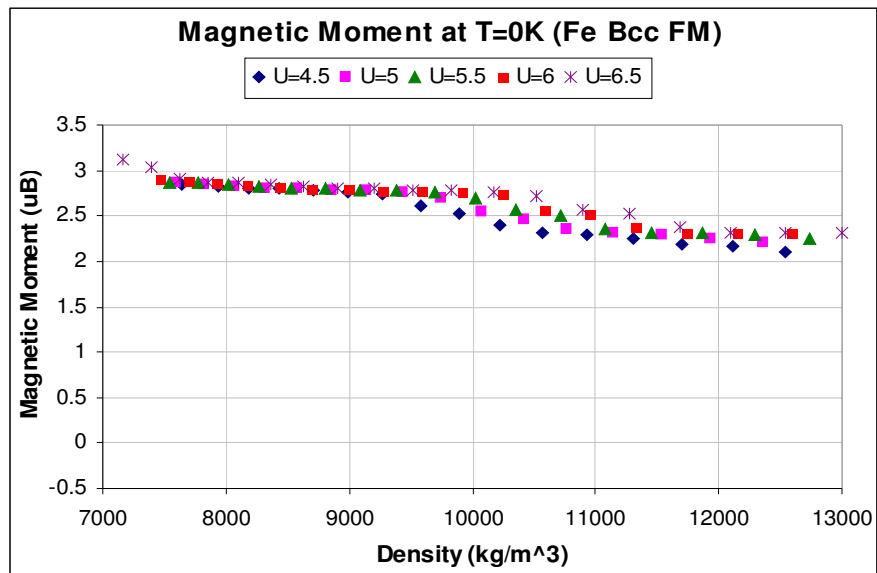
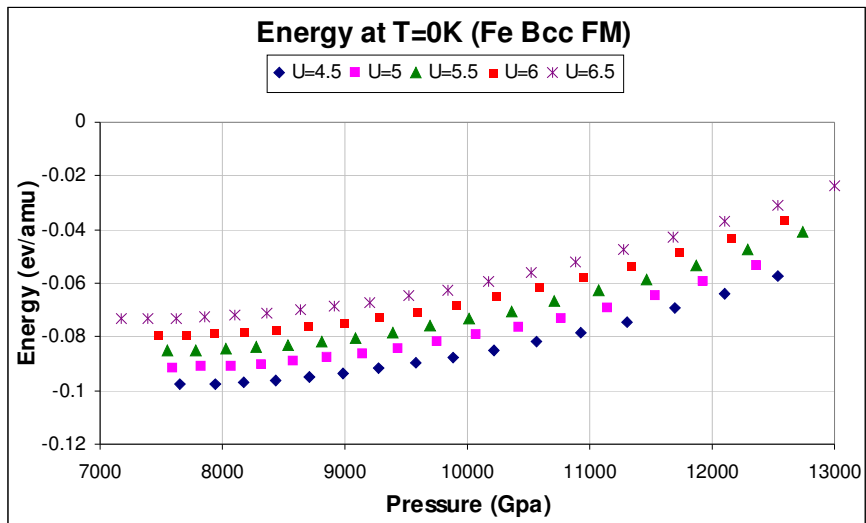


Figure 5-8. Ground state energies and magnetic moments at T=0K for bcc FM iron at various U (Hubbard_U).

Table 5-4. The summary of the investigations on approximations.

	PBE_PAW	PW91_PAW	Hubbard_U + PW91_PAW	Experiment	The methods for the best prediction
density (kg/m ³)	8365 (error 6.28%)	8373 (error 6.39%)	7648 (error -2.82%)	7870	Hubbard_U+PW91_PAW
BCC:					
Magnetic Order	Bcc FM	Bcc FM	Bcc FM	Bcc FM	all
Amplitude of Magnetic Moment	2.128	2.101	2.838	2.13	PBE_PAW & PW91_PAW
FCC:					
Magnetic Order	Fcc AFM	Fcc AFM	Fcc FM	-	
Amplitude of Magnetic Moment	0.936	0.987	2.608	0.635 (Wang-1985)	
HCP:					
Magnetic Order	Hcp NM	Hcp NM	Hcp FM	Hcp NM	PBE_PAW & PW91_PAW
Amplitude of Magnetic Moment			3.041		
axial ratio c/a	1.6	1.58	1.722	1.6	PBE_PAW & PW91_PAW

5.3.1.2 *Fcc Iron*

A conventional unit cell with 4 atoms is used for the analysis of the fcc iron lattice. The unit lattice vectors are [1 0 0; 0 1 0; 0 0 1]. The direct positions of the four atoms are [0 0 0], [0 0.5 0.5], [0.5 0 0.5] and [0.5 0.5 0]. The magnetic orders considered are along the [001] direction. For collinear magnetic orders, for a ferromagnetic phase, all the four atoms in the conventional unit cell have the same spin orientation; however, for an antiferromagnetic phase, the spin orientations are different. The magnetic orders in ferromagnetic and antiferromagnetic phases in a fcc lattice are showed in Figure 5-9.

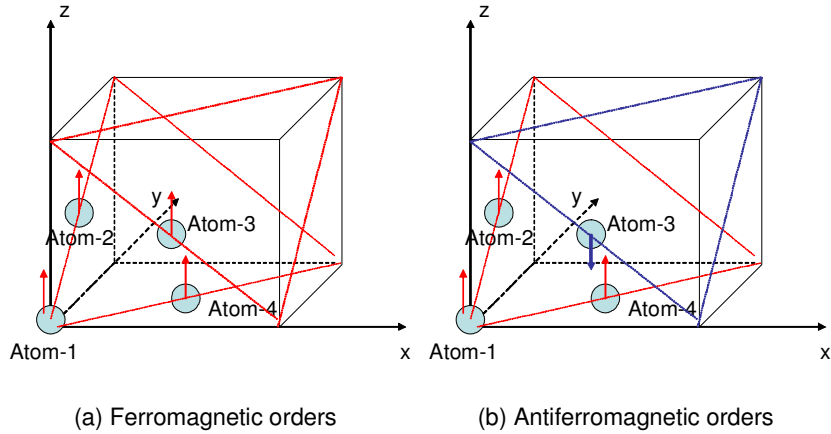


Figure 5-9. Collinear magnetic orders in [001] for fcc iron.

Similarly, various combinations of approximations (Table 5-3) were used in the studies of fcc iron. We have implemented the ground state calculations for fcc FM, bcc AFM and bcc NM structures (Figure 5-1).

(1) For the combination of PBE and PAW, the results, including ground state energies and magnitude of the magnetic moments vs. density, are shown in Figure 5-10 and Figure 5-11. From Figure 5-10 and Figure 5-11, the AFM phase has the minimum energy at the ground state, which is in agreement with the investigation by Kubler [Kubler--1981] and Clatterbuck [Clatterbuck--2002]. In addition, the ferromagnetic phase has the lower energy than the nonmagnetic phase, which coincides with the observations by Clatterbuck [Clatterbuck—2002]. Lattice constant of fcc antiferromagnetic is approximately 3% smaller than experiment [Tsunoda--1989]. The predicted fcc lattice constant is 3.455865\AA , which lies in the range from 3.47\AA to 3.56\AA presented by Garcia. At the equilibrium lattice constants, for the antiferromagnetic phase, the magnetic phase low-spin at low-volume is predicted at $0.939\mu_B$, which is larger comparing to the value $0.64\mu_B$ calculated by Wang in 1985 [Wang--1985].

(2) For the combination of PW91 and PAW, the results are shown in Figure 5-12 and Figure 5-13. From Figure 5-12 and Figure 5-13, PW91_PAW accurately predicted that the antiferromagnetic phase has the minimum energy at the ground state for fcc iron. However, the magnetic moments of FM phase were totally underestimated. The predicted lattice constant of the fcc antiferromagnetic phase is at 3.428 Å, which is slightly away from the range of [3.47 Å ~ 3.56 Å]. At the equilibrium lattice constants, for the antiferromagnetic phase, magnetic moments predicted are predicted at $0.635\mu_B$, which is very close to $0.64\mu_B$ calculated by Wang in 1985 [Wang--1985]. It can be seen that the magnetic phase predicted here is a low-spin state at the low-volume.

(3) For the combination of PW91 and PAW with Hubbard-U of $U=4.5$ and $J=1$, the results are shown in Figure 5-14 and Figure 5-15. From Figure 5-14 and Figure 5-15, we observed that the FM phase is the stable phase, which is contrary to the predictions by PBE_PAW and PW91_PAW, which do not include the Hubbard-U approximations. Although the ground state of fcc iron is thought to be the AFM from early measurements [Kondorskii--1959] on the fcc alloys of iron and analyzing small particles of fcc iron precipitates from supersaturated Cu-Fe solid solutions [Abrahams--1970], more measurements of the precipitates show that FM is at the ground state for fcc iron [Gonser--1980]. Therefore, it is not clear how to decide which magnetic order really stays at the ground state. It is concluded that either FM or AFM occurs to the films of fcc iron grown on copper surfaces [Wright—1971, Gradmann—1976, Keune—1977 & Gradmann--1980]. The predicted lattice constant for FM phase 3.603977 Å; while a 3.78034Å for AFM phase and a 3.4062 Å for NM phase.

The calculated results from Hubbard_U ($U=4.5$ & $J=1$) support the idea that the fcc iron exists in FM phase with the low-spin at low-volume and high-spin at high-volume because of its minimum energy. It is worth mentioning that Hubbard_U accurately verified that fcc ferromagnetic phase has two distinct FM fcc phases. One is with a small volume and moment; the other is with a larger volume and moment, which is in the agreement with the investigation presented by Tsunoda [Tsunoda--1989], Wang [Wang--1085] and Clatterbuck [Clatterbuck--2002]. The magnetic orders of fcc antiferromagnetic orders are totally overestimated. Lattice constant of fcc ferromagnetic is very close to the experimental value 3.577 \AA [Tsunoda--1989], and lattice constant of fcc nonmagnetic is very similar to the all-electron estimate of 3.375 \AA [Garcia-Suarez--2004].

In summary, PBE_PAW and PW91_PAW approximations predict an AFM phase for fcc iron at the ground state. However, with Hubbard_U of $U=4.5$, a FM phase is predicted for fcc iron at the ground state. Hubbard_U presents an excellent prediction about FM fcc iron that two distinct magnetic states exist. But it overestimated the magnetic orders of AFM fcc iron, which are presented by PAW_GGA in good agreement with Wang's calculations in 1985 [Wang--1985].

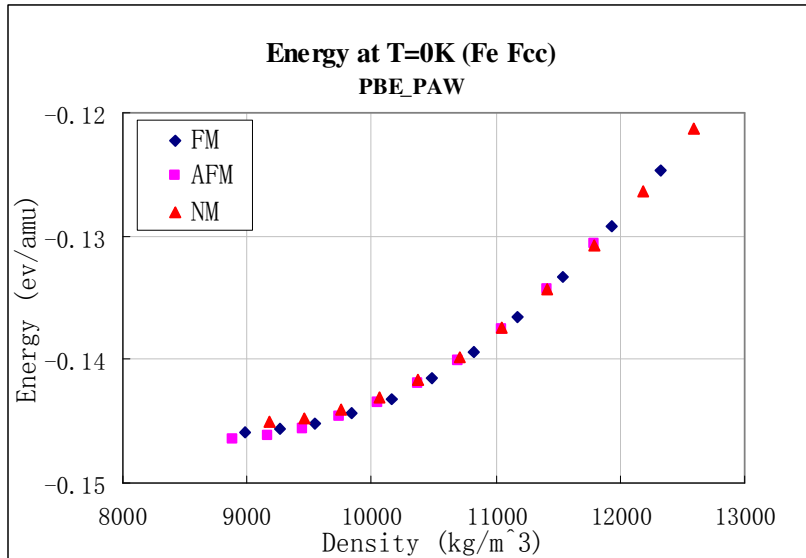


Figure 5-10. Ground state energies of fcc iron vs. density (by PBE with PAW).

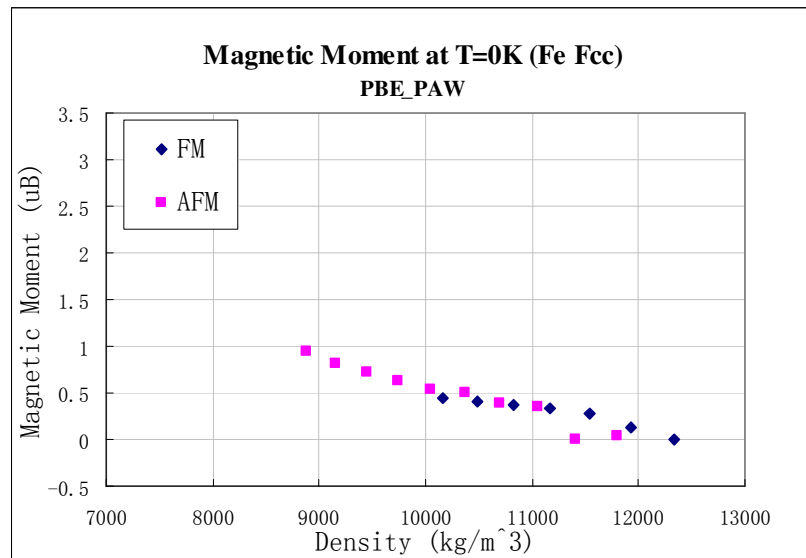


Figure 5-11. Magnitude of the magnetic moments of fcc iron vs. density (by PBE with PAW and Hubbard_U [U=4.5 & J=1]).

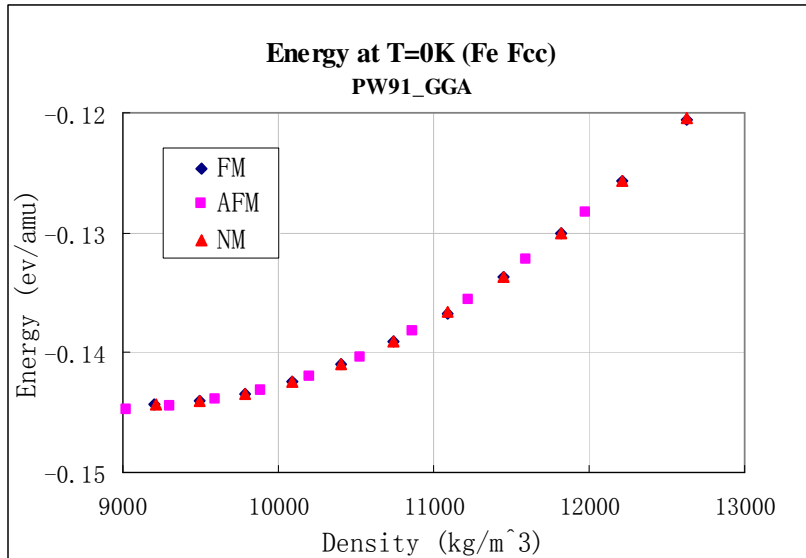


Figure 5-12. Ground state energies of fcc iron vs. density (by PW91 with PAW).

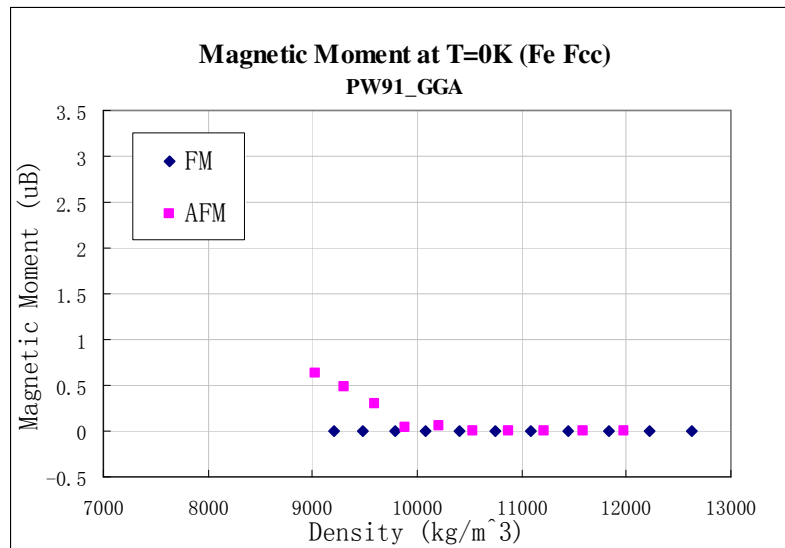


Figure 5-13. Magnitude of the magnetic moments of fcc iron vs. density (by PW91 with PAW).

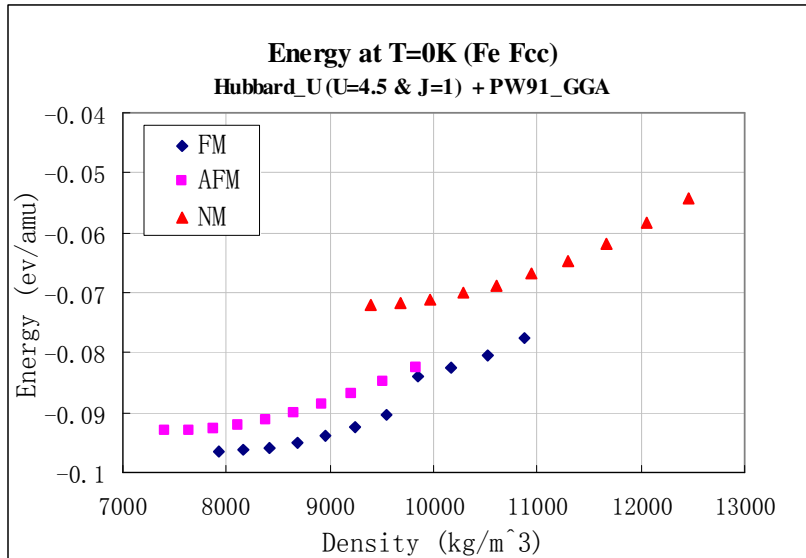


Figure 5-14. Ground state energies of fcc iron vs. density (by PW91 with PAW and Hubbard_U [U=4.5 & J=1]).

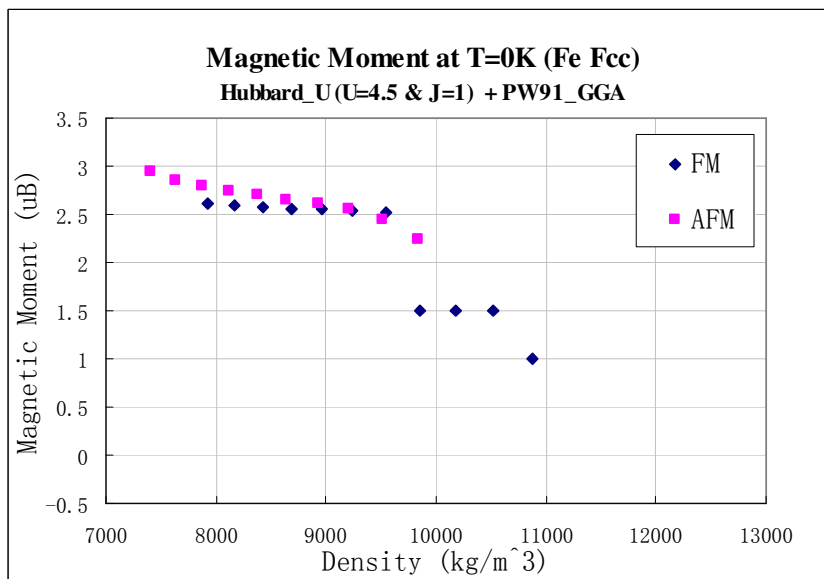


Figure 5-15. Magnitude of the magnetic moments of fcc iron vs. density (by PW91 with PAW and Hubbard_U [U=4.5 & J=1]).

5.3.1.3 Hcp Iron

Hcp iron is more complex than bcc because of its lattice structure. The ratio between the height of the hexagon and the edge length on the bottom plane is called axial ratio c/a , which is about 1.6 at the lattice equilibrium volume. A conventional unit cell consisting of two atoms is selected for analyzing the hcp iron. The unit lattice vectors are $[1\ 0\ 0; -0.5\ 0.866\ 0; 0\ 0\ 1.6]$. The initial direct coordinates of the two atoms are $[0\ 0\ 0]$ and $[0.3333\ 0.6666\ 0.5]$. For collinear magnetic orders, both two atoms in the 2-atom conventional unit cell have the same spin orientation for ferromagnetic case and opposite orientation for antiferromagnetic case (Figure 5-16, Figure 5-17).

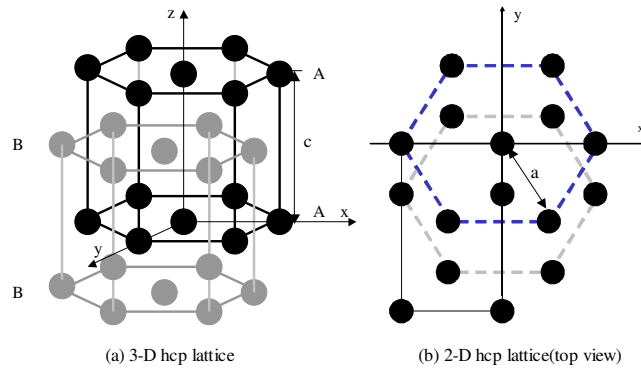


Figure 5-16 NM Hcp lattice structure (A/B/A/B).

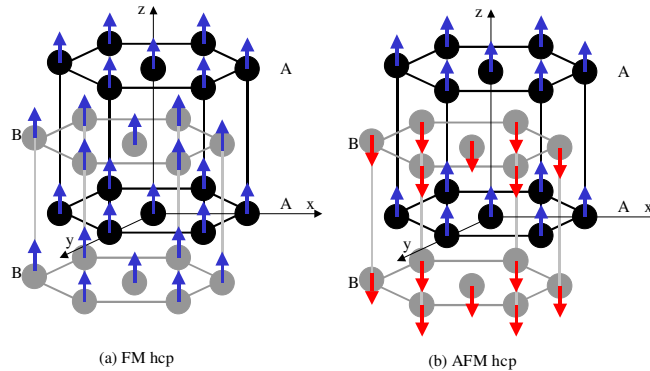


Figure 5-17. FM hcp and AFM hcp lattice structures and magnetic orders.

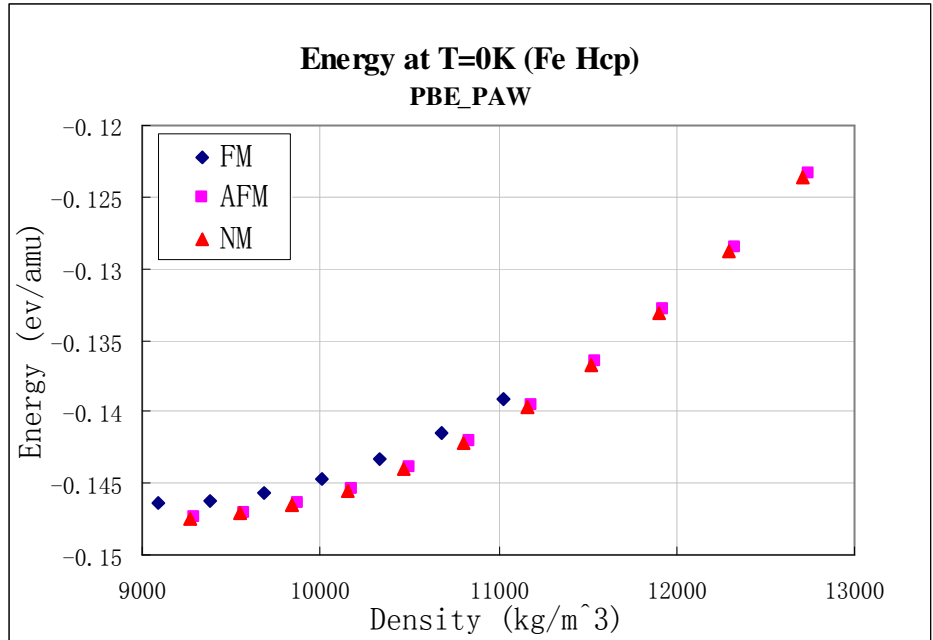


Figure 5-18. Ground state energies of hcp iron vs. density (by PBE with PAW).

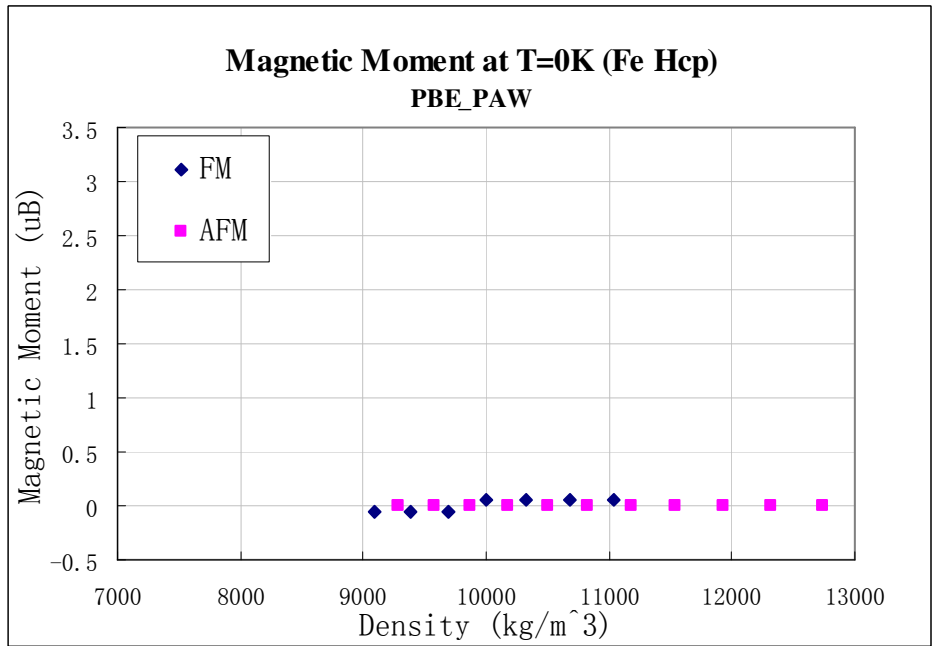


Figure 5-19. Magnetic moments of hcp iron vs. density (by PBE with PAW).

(1) For the combination of PBE and PAW, the results, including ground state energies and magnitude of the magnetic moments vs. density, are shown in Figure 5-18 and Figure 5-19. The predicted lattice constant is 2.48413 Å for ferromagnetic phase, ratio c/a is 1.73; 2.4319 Å for antiferromagnetic phase, ratio c/a 1.603; 2.43427 Å for nonmagnetic phase, ratio c/a is 1.602. The predicted c/a ratios of antiferromagnetic and nonmagnetic phases have the very good agreement with the experimental measurement 1.6 [Jephcoat--1986] and theoretically determined ratio [Steinle-Neumann--1999]. It also predicted that the NM phase has the minimum energy at the ground state among the three magnetic phases, which has also been supported by the experiments [Williamson—1972, Cort—1982, Nasu-2002, Taylor--1991]. At the equilibrium lattice constants, the antiferromagnetic phase is incorrectly predicted. Steinle-Neumann suggested that it could be the reason that it is impossible to surround every atom with atoms of opposite spin in hcp lattices [Steinle-Neumann--2003].

It is worth mentioning that the FM phase has a sudden drop from 2.305 μ B to 0.574 μ B in magnetic moment when pressure is close to 14.5Gpa. Steinle-Neumann [Steinle-Neuman--2004] suggested that pressure would broaden the electronic bands and has the tendency to increase the separation between these electronic states, which results in decreasing the magnetic moments.

(2) For the combination of PW91 and PAW, the results are shown in Figure 5-20 and Figure 5-21. The predicted lattice constant is 2.44512 Å for ferromagnetic phase and ratio c/a is 1.58; 2.4445 Å for antiferromagnetic phase and ratio c/a 1.583; 2.44463 Å for nonmagnetic phase and ratio c/a 1.583. Excellent agreement is observed for the c/a ratio comparing to experimental measurements: 1.58 ($P = 0$ GPa) to 1.60 ($P = 400$ GPa).

[Jephcoat--1986]. It also predicted that the NM phase the minimum energy at the ground state. At the equilibrium lattice constants, compared to the calculations of Steinle-Neumann [Steinle-Neumann--2004], the magnetic moments of AFM phase are overestimated.

(3) For the combination of PW91 and PAW with Hubbard-U of $U=4.5$ and $J=1$, the results are shown in Figure 5-14 and Figure 5-15. The predicted lattice constant is 2.588 Å for ferromagnetic phase and ratio c/a is 1.72; lattice constant Å for antiferromagnetic phase and ratio c/a 1.811; 2.4106 Å for nonmagnetic phase and ratio c/a 1.603. With Hubbard_U, an overestimation of the c/a ratio for FM and AFM are observed. Contrary to approximations without Hubbard-U, the FM phase is predicted to have the minimum energy at the ground state. Although there are some experiments showing the NM phase is the stable magnetic order for hcp iron, some evidences have been provided by other experiments [Williamson—1972, Cort—1982, Nasu-2002, Taylor--1991] are controversial and therefore not conclusive. Actually, the magnetic structure of the hcp phase is quite complicated. A scientific debate about magnetic phase of hcp structure has existed for thirty years. Moreover, Hubbard_U ($U=4.5$) also suggested the higher magnetic moments than the prediction by using PW91 and PAW.

(4) Hubbard-U method with various U values are also investigated, in the framework of PW91 and PAW. The values of 'U' change from 4.5 to 6.5. The comparisons for various U are shown in Figure 5-24. We can see that as U increases, the predicted density at the equilibrium lattice constants decreases.

In summary, the predictions on several items by using various approximations are listed in Table 5-4. For density, with Hubbard-U seems to yield an improved prediction;

for magnetic order and magnetic moment, since the experimental evidence on fcc and hcp irons is not conclusive, every combination of approximations supported some experimental observations; for the hcp axial ratio c/a , approximations of PW91 and PAW or PBE and PAW predict a better solution.

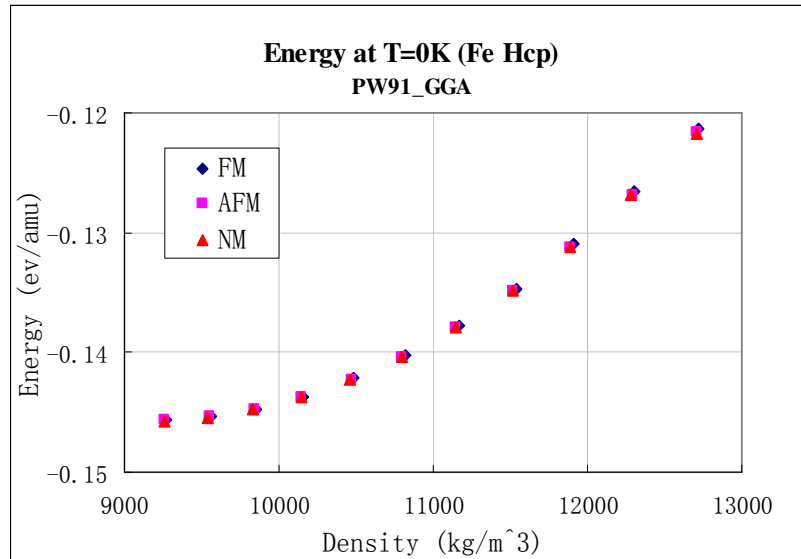


Figure 5-20. Ground state energies of hcp iron vs. density (by PW91 with PAW).

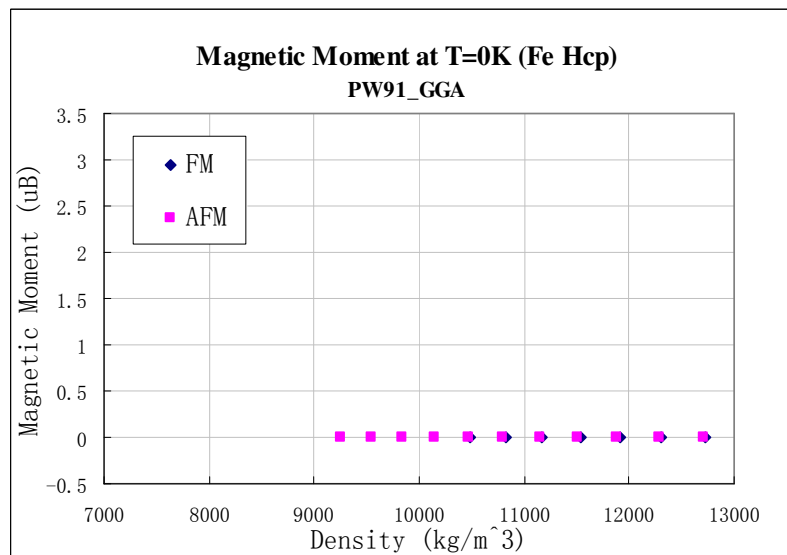


Figure 5-21. Magnetic moments of hcp iron vs. density (by PW91 with PAW).

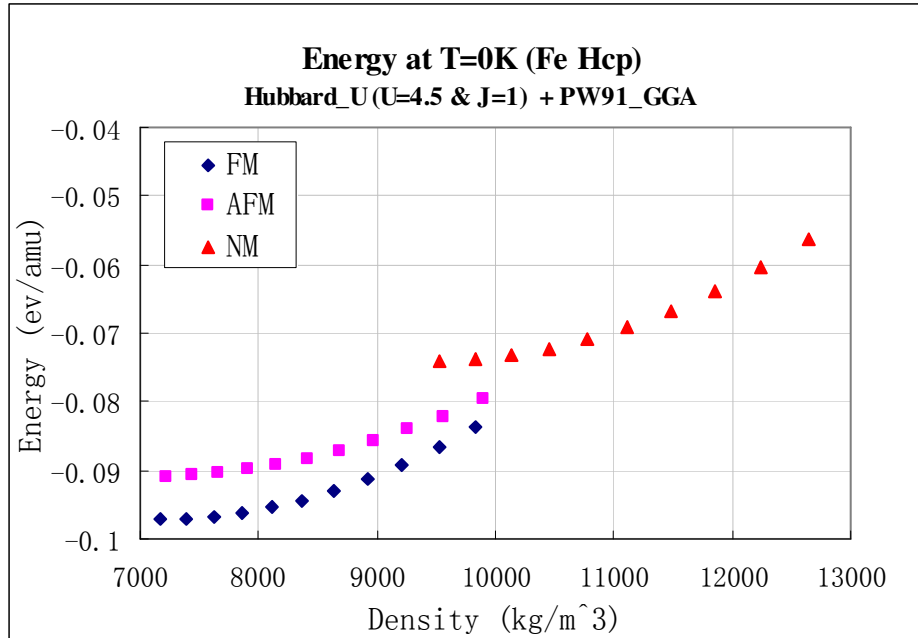


Figure 5-22. Ground state energies of hcp iron vs. density (by PW91 with PAW and Hubbard_U [U=4.5 & J=1]).

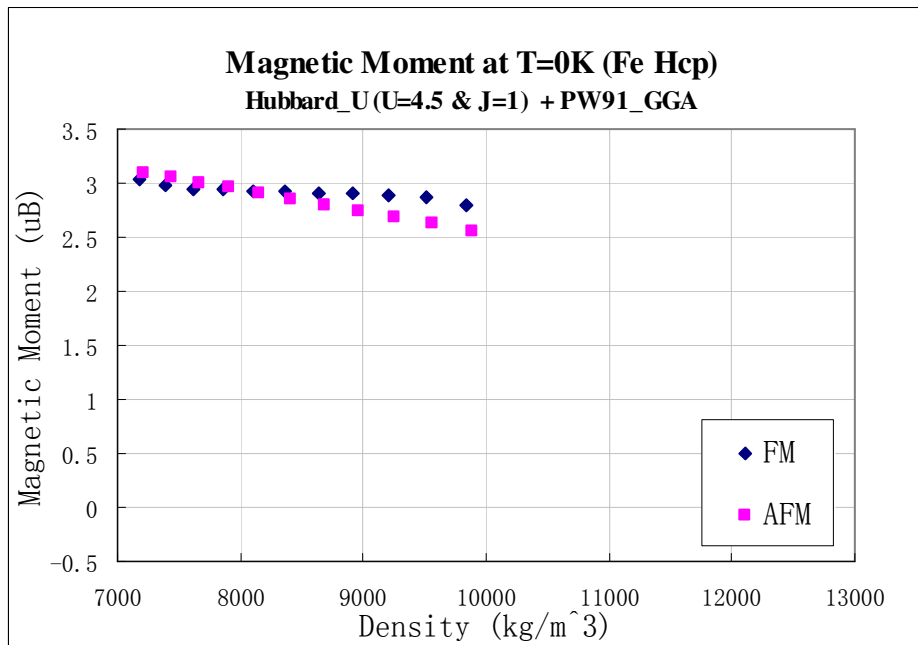


Figure 5-23. Magnitude of the magnetic moments of hcp iron vs. density (by PW91 with PAW and Hubbard_U [U=4.5 & J=1]).

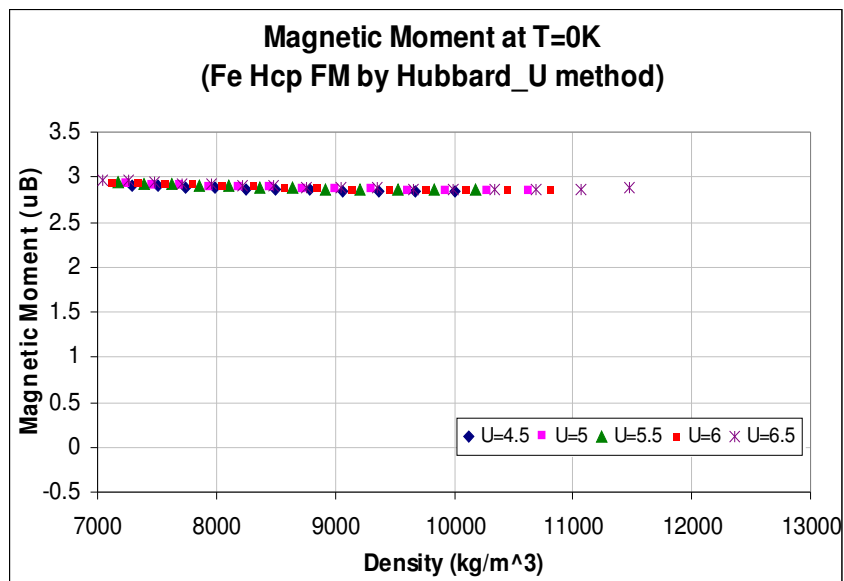
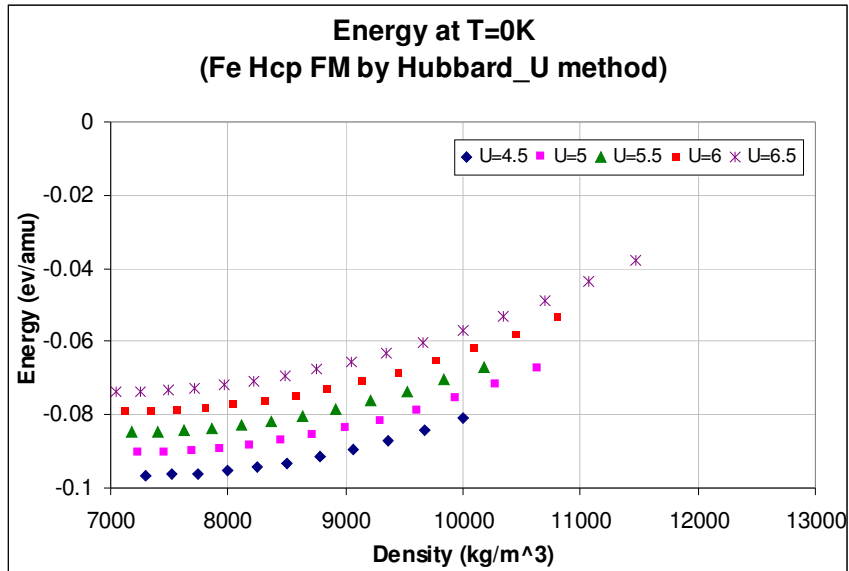


Figure 5-24. Ground state energies and magnetic moments at T=0K for hcp FM iron at various U (Hubbard_U).

5.3.2 Phase Transitions for Iron

Phase transition from bcc to hcp is observed in experimental phase diagram (Figure 5-25). Experiments showed that the phase transition from bcc to hcp occurs in the pressure range from 10Gpa to 15Gpa [Jephcoat-1986]. Stixrude suggested 11Gpa to the occurrence of the phase transition by using PW-II [Stixrude--1994]. Soderlind presented the pressure 10Gpa to the phase transition [Soderlind--1996].

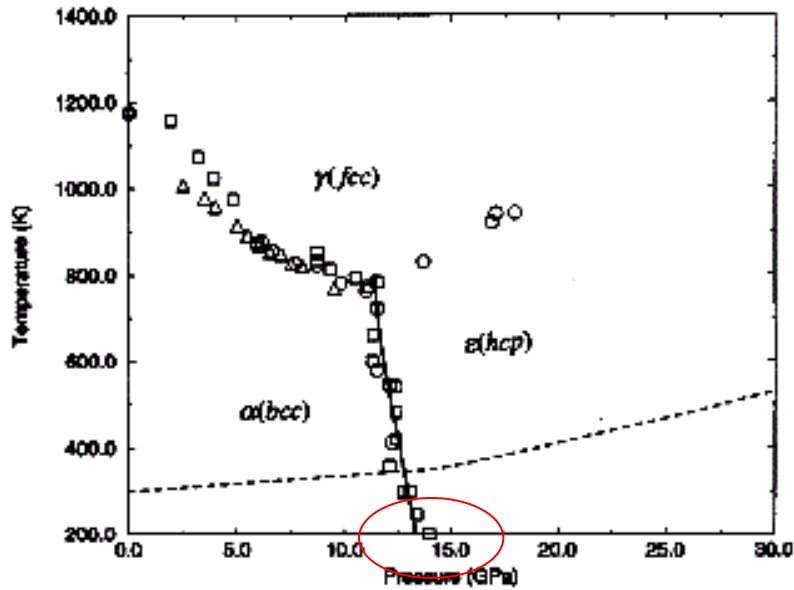


Figure 5-25. Phase diagram of iron [Jephcoat-1986].

In Figure 5-28, Figure 5-29, and Figure 5-30, we present our calculations for bcc, fcc and hcp iron with identified magnetic orders. The cross-points in the energy figures correspond to the phase transition locus. The results are presented and discussed as follows.

For the combination of PBE and PAW, the predicted phase transition sequence is from bcc FM to hcp NM at a pressure $P = 31$ GPa, and then to fcc AFM at a pressure $P =$

43 GPa; for the combination of PW91 and PAW, the predicted phase transition sequence is from bcc FM to hcp NM at a pressure $P = 9.8$ GPa; For the combination of PW91 and PAW with Hubbard-U ($U=4.5$ and $J=1$), the predicted phase transition sequence is from bcc FM to fcc FM at a pressure $P = 35$ GPa. Comparing to the experimental observations, we can see that PW91 and PAW not only gives the correct prediction on magnetic orders but a better prediction on critical pressure of phase transitions for bcc FM to hcp NM iron [Singh--1991]. Moreover, PW91 and PAW also predicted a good hcp c/a ratio. Therefore, for the construction of the EOS of iron in the next section, we used PW91 and PAW with a higher precision control (KPOINTS $9 \times 9 \times 9$, EDIEF = 10^{-7} eV and EDIEFG = 10^{-6} eV).

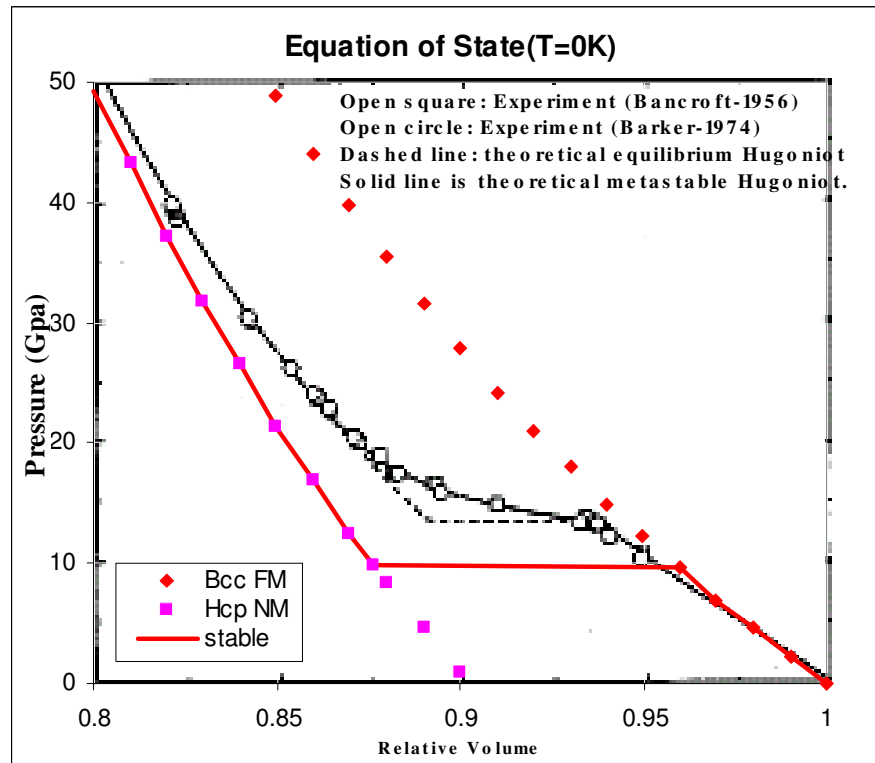


Figure 5-26. Phase Transition from Bcc FM to Hcp NM.

5.3.3 Equation of State for Iron

With the verification of structural and magnetic phase transitions from bcc FM to hcp NM, the EOS of iron is constructed from the EOS of bcc FM and hcp NM. The results are shown in Figure 5-27 and compared to data provided in the paper by Jonnathan, Boettger and Wallace [Jonathan et al. 1997].

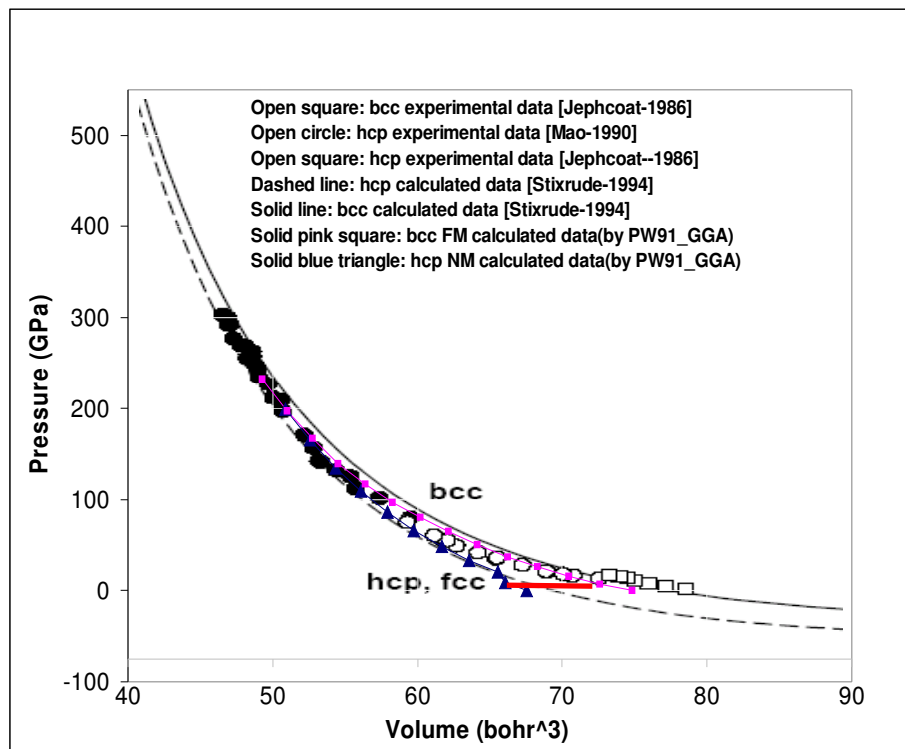


Figure 5-27. EOS of iron with phase transitions from bcc FM to hcp NM at $P = 9.8$ GPa and comparison with experimental data [Jonathan et al. 1997].

5.3.4 Discussions

5.3.4.1 *Hubbard_U Method*

As stated in the studies by Rozenberg et al.[Rozenberg--2005], the L(S)DA often fails to describe systems with localized (strongly correlated) d and f electrons (this manifests itself primarily in the form of unrealistic one-electron energies). In some cases this can be remedied by introducing a strong intra-atomic interaction in a (screened) Hartree-Fock like manner, as an on-site replacement of the L(S)DA [Kresse--2005]. This approach is commonly known as the L(S)DA+U method. The Hamiltonian of DFT is modified by a Hubbard-Hamiltonian

$$H = \frac{U}{2} \sum_{m,m',s} n_{m,s} n_{m',-s} + \frac{(U-J)}{2} \sum_{m \neq m',s} n_{m,s} n_{m',s} \quad (5.3.4-1)$$

where $n_{m,s}$ is the operator yielding the number of electrons occupying an orbital with magnetic quantum number m and spin s at a particular site. The Coulomb repulsion is characterized by a spherically averaged Hubbard parameter U describing the energy required for adding an extra d electron to a Fe atom, and a parameter J representing the screened exchange energy. While U depends on the spatial extension of the wave functions and on screening, J is an approximation of the Stoner exchange parameter and is very often considered as constant $J = 1$ eV. The total energy of the modified system is then given by

$$E_{\text{DFT+U}} = E_{\text{DFT}} + \frac{(U-J)}{2} \sum_{m,s} (n_{m,s} - n_{m,s}^2) \quad (5.3.4-2)$$

In this thesis, the effective on-site electronic interaction (the Hubbard U) is incorporated and used to investigate iron with PW91 and PAW. The value of U is taken from 4.5eV to 6.5ev according to the previous work [Yamasaki—2003 & Punkkinen--1999].

From the investigation of Hubbard_U to bcc, fcc and hcp iron, one can see Hubbard_U does not present an excellent prediction. In the verification of the magnetic order, for bcc iron, it does verify the correct FM order that is in agreement with the experiment [Jephcoat--1986]. For fcc iron, it presents an opposite result that FM is the stable one [Wang--1985]. For hcp iron, obviously being different from experimental results [Jephcoat--1986], Hubbard_U suggests hcp FM is the stable one. In the verification of the magnetic moment, Hubbard_U overestimates the magnetic moments for all the three lattice structures of iron. Therefore, Hubbard_U will not be selected for the investigation of the steel alloys.

5.3.4.2 Comparisons among PBE_PAW, PW91_PAW & Hubbard_U with PW91_PAW

As shown in Table 5-4, various approximate methods used in ab initio techniques can predict well only in some aspects. Based on the previous description, it seems that Hubbard-U method can drastically change magnetism but might not in a desirable direction. However, Hubbard_U indeed improve the prediction of density. On the other hand, in the framework of GGA and PAW, both PBE and PW91 produce a similar prediction on iron properties. These observations will provide guideline for the studies of steels.

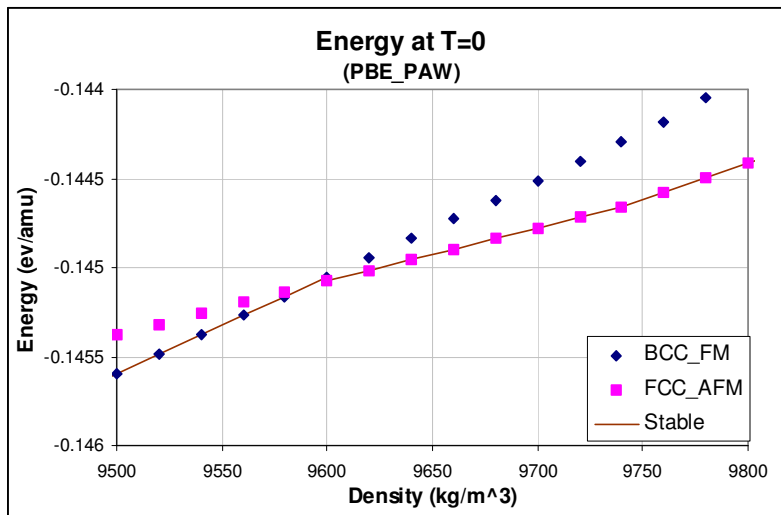
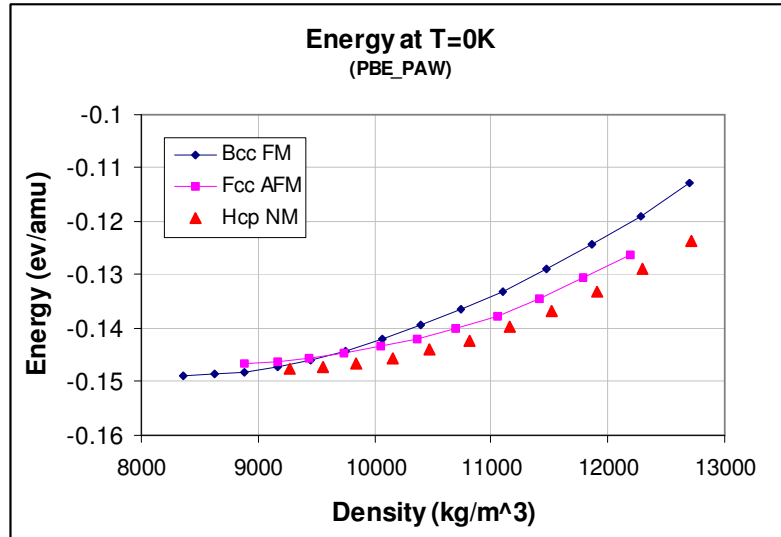


Figure 5-28. Energy comparison of bcc FM, fcc AFM, and hcp NM (by PBE and PAW).

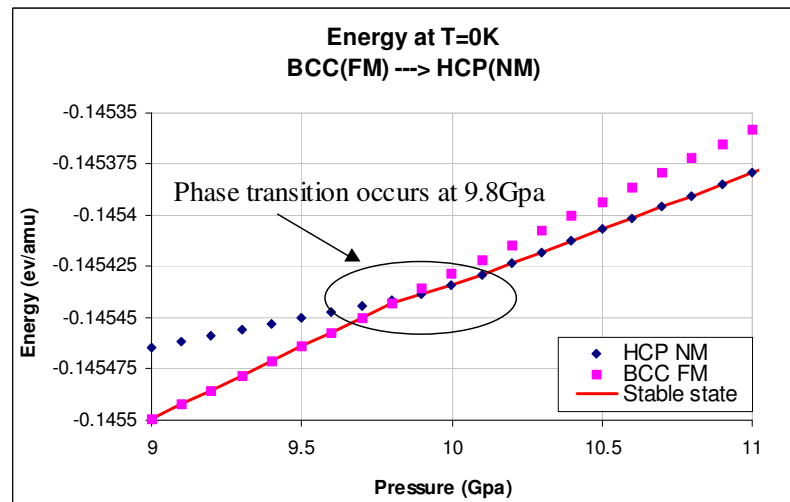
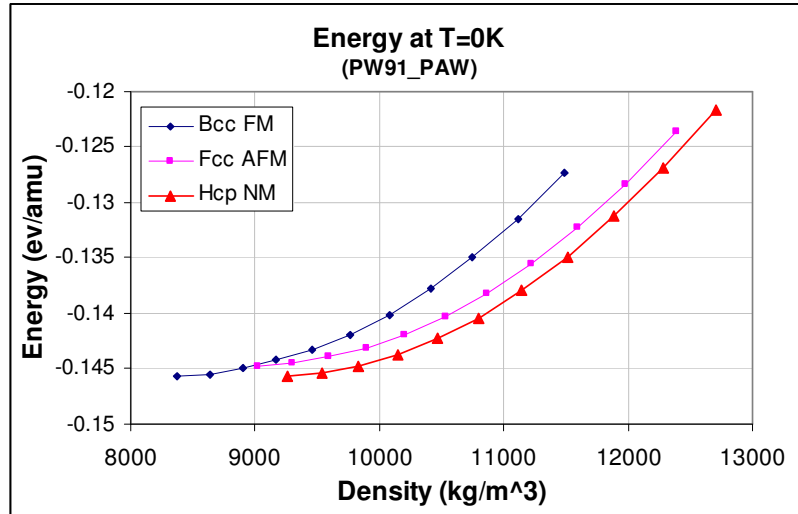


Figure 5-29. Energy comparison of bcc FM, fcc AFM, and hcp NM (by PW91 and PAW).

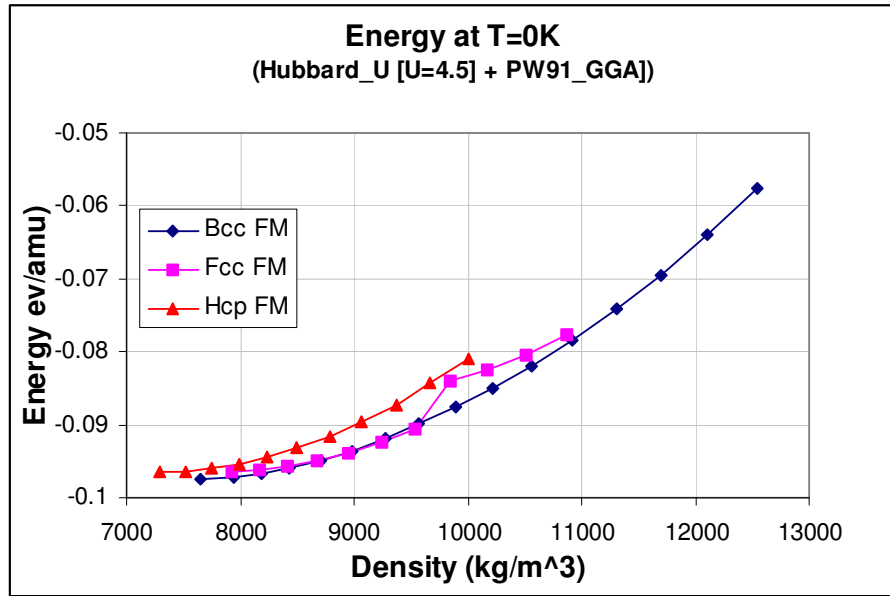


Figure 5-30. Energy comparison of bcc FM, fcc AFM, and hcp NM (by PW91 and PAW with U=4.5 and J=1).

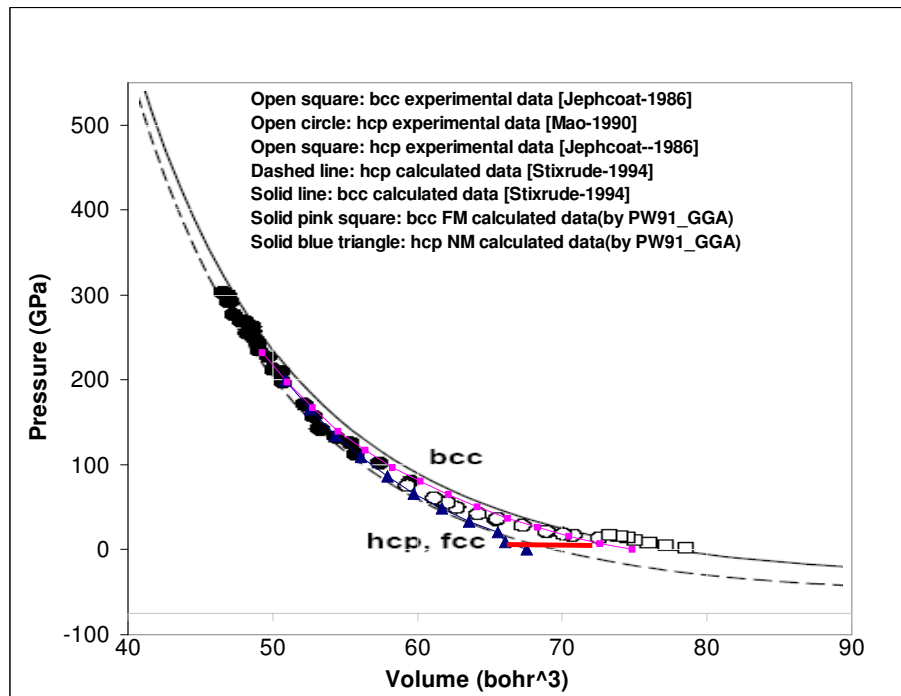


Figure 5-31. EOS of iron with phase transitions from bcc FM to hcp NM at P = 9.8 GPa and comparison with experimental data [Jonathan et al. 1997].

CHAPTER 6

EOS AND MAGNETIC PROPERTIES FOR STEEL ALLOYS

The objective in this chapter is to predict the EOS of steels from ab initio methods. Although the host material of steel alloys, i.e. the pure iron, has been studied extensively, including the EOS, electronic structures, magnetic and structural phases, the ab initio studies of steels are far from mature. This is mainly because the steel is an alloy and the alloy is disordered, and the iron is an ordered crystal. In addition, there are numerous types of steels. The difficulties are in modeling the disordered structures, with many possible combinations. In this thesis, we start from the host material, i.e. the iron, and then systematically add other elements of interest. The effects of each element and their cumulative effects are investigated. Eventually we would like to use our studies to design for new alloys with desirable erosion resistance. In this thesis, we are restricting the studies to the two most commonly used elements in steels: nickel and carbon. Nickel, has properties similar to iron, and is a substitutional constituent. Carbon, with very different properties, is treated as an interstitial addition to the alloy.

As discussed in Chapter 2, theoretical difficulties lie in finding efficient methods that yield sufficient accuracy to simulate the disordered structures. Based on previous studies, a method and a procedure are proposed to obtain structures that can represent the characteristics of disordered structures and also can be used in the ab initio calculations. The method can treat both substitutional and interstitial species.

Instead of using the mean field approach, which does not treat the dependence of properties on the local environments surrounding atoms explicitly, or using the cluster expansion method, which requires large statistical ensembles of component figures with each one needing characterization, a SQS (special quasirandom structure) method is used. This method creates a virtual repeated structure or a super unit cell that can approximately represent the disordered substitutional alloys. The correlations in the disordered structures are preserved up to an order of accuracy that can be controlled. Then, interstitial species are added to sites in the host substitutional alloy or supercell.

First, a procedure to obtain a virtual structure for the substitutional disordered binary alloy $\text{Fe}_{1-x}\text{Ni}_x$ by using the SQS is studied. Then, a virtual structure is constructed, for a ternary alloy $\text{Fe}_{1-x-y}\text{Ni}_x\text{C}_y$ from the binary alloy $\text{Fe}_{1-x}\text{Ni}_x$. This is accomplished by adding carbon atoms at interstitial sites, that reside in the optimal O-sites. Then, ab initio method is used to predict EOS for: (1) *Host metal*: Iron; (2) *Binary alloy*: $\text{Fe}_{1-x}\text{Ni}_x$; (3) *Ternary alloy*: $\text{Fe}_{1-x-y}\text{Ni}_x\text{C}_y$. The determination of the optimum SQS configuration, the equilibrium electronic structures and the equation of state $\text{Fe}_{1-x}\text{Ni}_x$ is not considered previously in the literature with low concentration of Ni. The treatment of ternary $\text{Fe}_{1-x-y}\text{Ni}_x\text{C}_y$, with its equilibrium electronic structure and the equation of state has not been discussed before in the literature.

6.1 Binary Alloy $\text{Fe}_{1-x}\text{Ni}_x$ by Using the SQS Method

For a disordered (or random) binary alloy $A_x\text{B}_{1-x}$, there is no correlation in the occupation of various sites. The correlation functions $\overline{\Pi}_f$ simply become the product of lattice-averaged variables of the ‘figure’ f , where figures f are symmetry-related

groupings of lattice sites. These figures, $f = (k, m)$ can have k vertices and span a maximum distance of m ($m = 1, 2, 3 \dots$ are the first, second and third-nearest neighbors, etc.). For a random binary alloy, the correlation functions are proven to be

$$\bar{\Pi}_f(\text{radom}) = \bar{\Pi}_{k,m}(\text{random}) = \langle \bar{\Pi}_{k,m} \rangle_{\text{randomR}} = (1 - 2x)^k \quad (6-1)$$

Table 6-1. Correlation functions of a random binary alloy A_xB_{1-x} with $x = 0.125$.

$\bar{\Pi}_{k,m}$		M					
		2	3	4	5	6	7
k	2	0.5625	0.5625	0.5625	0.5625	0.5625	0.5625
	3	0.4219	0.4219	0.4219	0.4219	0.4219	0.4219
	4	0.3164	0.3164	0.3164	0.3164	0.3164	0.3164

For example, the matrix of correlation functions for random binary alloy A_xB_{1-x} , for $x = 12.5\%$, is given in Table 6-1. For the binary $Fe_{1-x}Ni_x$ substitutional disordered alloy, the material properties depend on the lattice configuration. The first task is to construct a virtual periodic structure (or supercell) of small sizes, which mimic the correlation functions of the random alloys in equation (6-1). Theoretically if we construct a virtual structure of infinite size, we can reproduce all the correlation functions of a random alloy. However, for a finite size of system like SQS-N structures with $N = 8, 16$, etc., atoms per unit cell, errors are surely introduced beyond a certain distance. However, the errors are limited to those that are acceptable, since the interaction force due to elements at a smaller distance between the nearest neighbors are much greater than that due to element at a larger distance. Of course, a larger size of SQS structure (larger N) will result in

matching of the correlation functions to a larger distance (k, m) . Therefore, the approximate method and the resulting accuracy involve a trade-off between the selections of the size N of SQS and the accuracy desired for matching the random correlation functions up to certain distance (k, m) . This means that we first select an acceptable distance (K, M) , where $k = 2, \dots, K$ and $m = 2, \dots, M$, and then construct a SQS-8, SQS-16, etc. The errors of SQS- N structures can be determined by

$$\begin{aligned} error &= \sum_{k=2}^K \sum_{m=2}^M [\bar{\Pi}_{k,m}(\text{SQS}-N) - \bar{\Pi}_{k,m}(\text{random})] \\ &= \sum_{k=2}^K \sum_{m=2}^M [\bar{\Pi}_{k,m}(\text{SQS}-N) - (2x-1)^k] \end{aligned} \quad (6-2)$$

In the present study, various SQS- N structures (with $N = 8$ and 16 atoms per unit cell) are constructed for a random binary alloy $\text{Fe}_{1-x}\text{Ni}_x$ with $x = 12.5\%$. As discussed in Chapter 2, a binary $\text{Fe}_{1-x}\text{Ni}_x$, with $x < \text{at. } 20\%$, is a bcc based structure. We used a *gensqs* code in the Alloy-Theoretic Automated Toolkit (ATAT). This program and the sample input program are listed in the Appendix. The main procedure to find SQS is as follows.

Create a structure (or supercell) with a right concentration x based on a bcc lattice, use the code *corrump* to calculate the random correlation functions $\bar{\Pi}_{k,m}(\text{Random})$ to a selected distance (K, M) . The program *corrump* and a sample input are shown in the Appendix.

Then, code *gensqs* is used to generate all the structures (or supercells) with N -atoms per unit cell and the concentration x based on bcc lattice; The program *gensqs* and a sample input are shown in the Appendix.

Then, code *corrdump* is used to calculate the correlation functions $\overline{\Pi}_{k,m}(S)$ for each structure S . The error in equation (6-2) is used to find the structures that are of error less than a selected tolerance.

The SQS_8 $\text{Fe}_{1-x}\text{Ni}_x$ structure for $x = 0.125$ is obtained by requiring its pair correlation functions to be equal to those of random alloy up to the third-nearest neighbor i.e. $(K, M) = (2, 3)$. Four SQS-8 structures are found to be of the smallest least square error 0.00825. The pair correlation functions of these structures are shown in Table 6-2. The SQS_16 $\text{Fe}_{1-x}\text{Ni}_x$ structure for $x = 0.125$ is obtained by requiring its pair correlation functions matching up to the sixth-nearest neighbor, i.e. $(K, M) = (2, 6)$. The errors of all the structures of $N = 16$ (there are 313 such structures) created by the code *gensqs* are shown in Figure 6-1. Among these, five structures are found to be of the smallest least square errors and are listed in Table 6-3. These five SQS-16 structures are of error 0.005207917 (equation 6-2) or 0.004774028. The pair correlation functions of these structures are shown in Table 6-4. We have selected a SQS-16 structure of the minimum error (noted by case 157 in Table 6-3) for simulations of a binary alloy $\text{Fe}_{1-x}\text{Ni}_x$ with $x = 0.125$. The ideal (unrelaxed) SQS-16 supercells is listed in Table 6-4. The relaxed SQS-16 supercell of NM order by using PBE and PAW is listed in Table 6-5. Other relaxed structures, of either FM or NM order, by using other combinations of approximations were also obtained. The relaxed structures are triclinic-type structures with space group S_2 . The mass densities predicted by various approximate methods are listed in Table 6-6. As seen, introducing Ni as a second constituent increases the density, in comparison to the pure iron.

Table 6-2. Pair correlation functions of four SQS-8 structures.
 (The numbers inside of the brackets [] indicate the degeneracy factors of the corresponding figures).

Concentration $x=0.128$					
Correlation Functions	Random	SQS_8			
		Case_1	Case_1	Case_3	Case_4
$\Pi_{2,1}[4]$	0.5625	0.625	0.5	0.5	0.5
$\Pi_{2,2}[3]$	0.5625	0.5	0.5	0.5	0.5
$\Pi_{2,3}[6]$	0.5625	0.58333	0.58333	0.58333	0.58333
$\Pi_{2,4}[12]$	0.5625	0.58333	0.54167	0.58333	0.5
$\Pi_{2,5}[4]$	0.5625	0.625	0.625	0.5	0.75
$\Pi_{2,6}[3]$	0.5625	0.5	0.5	0.66667	0.66667
Error	0	0.00825	0.00825	0.00825	0.00825

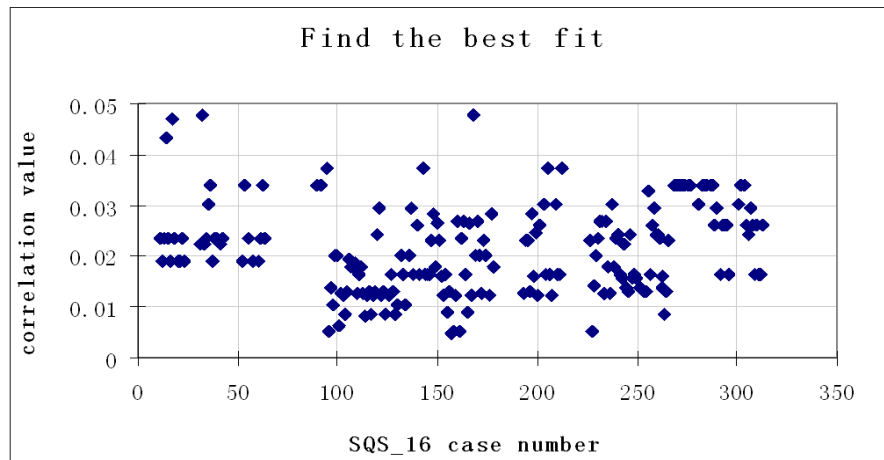


Figure 6-1. The errors of all the structures of N=16 atoms per unit cell and with $x = 0.125$.

Table 6-3. Pair correlation functions for five SQS-16 structures.

Concentration $x=0.128$						
Correlation Functions	Random	SQS_16				
		Case_96	Case_157	Case_158	Case_161	Case_227
$\Pi_{2,1}[4]$	0.5625	0.5625	0.5625	0.5625	0.5625	0.5625
$\Pi_{2,2}[3]$	0.5625	0.5	0.5	0.5	0.5	0.5
$\Pi_{2,3}[6]$	0.5625	0.54167	0.54167	0.54167	0.58333	0.58333
$\Pi_{2,4}[12]$	0.5625	0.58333	0.5625	0.54167	0.58333	0.54167
$\Pi_{2,5}[4]$	0.5625	0.5625	0.5625	0.5625	0.5625	0.5625
$\Pi_{2,6}[3]$	0.5625	0.58333	0.58333	0.58333	0.58333	0.58333
Error	0	0.005207917	0.004774028	0.005207917	0.005207917	0.00520792

Table 6-4. Ideal SQS-16 structure for alloy $\text{Fe}_{1-x}\text{Ni}_x$

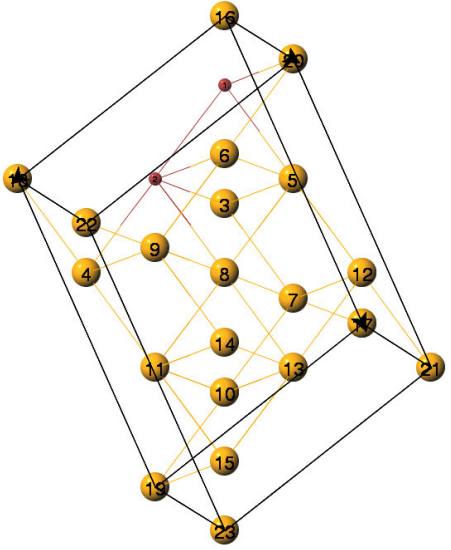
Ideal Supercell $\text{Fe}_{1-x}\text{Ni}_x$ ($x=12.5\%$)	Ideal SQS – 16 Structure				
	Lattice vectors: $a_1=[4.29 \ 1.43 \ -1.43]$ $a_2=[4.29 \ -1.43 \ 4.29]$ $a_3=[2.86 \ -5.72 \ -2.86]$				
	Ni	4.29	1.43	-1.43	1
	Ni	5.72	0	-5.72	2
	Fe	0	2.86	-5.72	3
	Fe	7.15	-1.43	-10.01	4
	Fe	2.86	5.72	-2.86	5
	Fe	8.58	2.86	-2.86	6
	Fe	-1.43	7.15	-7.15	7
	Fe	4.29	4.29	-7.15	8
	Fe	10.01	1.43	-7.15	9
	Fe	0	5.72	-11.44	10
	Fe	5.72	2.86	-11.44	11
	Fe	1.43	10.01	-4.29	12
	Fe	2.86	8.58	-8.58	13
	Fe	8.58	5.72	-8.58	14
	Fe	4.29	7.15	-12.87	15
	Fe	8.58	8.58	-14.3	16

Table 6-5. Equilibrium SQS-16 structure for $\text{Fe}_{1-x}\text{Ni}_x$ with NM order, relaxed by using PBE and PAW.

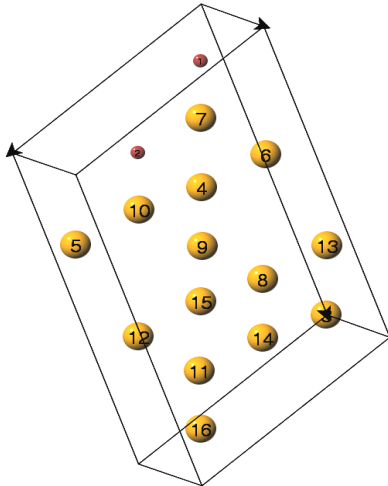
Relaxed Supercell $\text{Fe}_{1-x}\text{Ni}_x$ ($x=12.5\%$) ---- by PBE_PAW	Relaxed SQS-16 Structures			
	Lattice vectors:			
	$a_1=[3.668227532 \quad 1.57384526 \quad -1.224442031]$ $a_2=[3.661293334 \quad -1.56287608 \quad 3.652890144]$ $a_3=[2.444770028 \quad -6.28285806 \quad -2.447088622]$			
	Ni	2.445768684	-0.000290814	-0.000844956
	Ni	3.662564473	-1.562196819	1.210408885
	Fe	0.004686157	0.004369464	0.00671362
	Fe	2.422651893	-3.13348367	-0.026369795
	Fe	4.881821109	-3.130777761	2.422788424
	Fe	3.693780277	-1.579470869	-1.263405134
	Fe	4.888280344	0.005678813	-0.007439051
	Fe	3.644749412	-4.697512892	-1.2046293
	Fe	4.908353772	-3.147832802	-0.032895393
	Fe	6.103646999	-1.566857097	1.202850309
	Fe	4.859322907	-6.265874825	0.025880441
	Fe	6.107198259	-4.70411089	1.207682725
	Fe	4.881451871	-3.14529437	-2.454022584
	Fe	6.130451291	-4.711862024	-1.211154898
	Fe	7.339878845	-3.126206063	-0.00794414
	Fe	7.332575409	-6.277444019	-0.007422973

Table 6-6. Predicted densities for $\text{Fe}_{1-x}\text{Ni}_x$ ($x = 0.125$).

Density (kg/m^3)	$\text{Fe}_{1-x}\text{Ni}_x$		$\text{Fe}_{1-x-y}\text{Ni}_x\text{C}_y$		Fe (bcc)	
	NM	FM	NM	FM	NM	FM
PBE_PAW	10,096	9,292	9,413	9,404	8,964	8,365
PW91_PAW	9,470	8,643	8,776	8,631	8,964	8,373

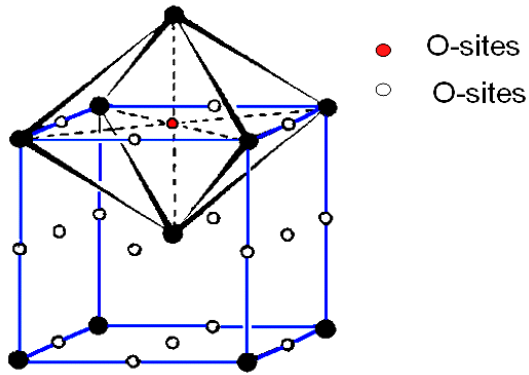


Figure 6-2. O-sites in the bcc conventional unit cell.

•Rhombohedron primitive cell

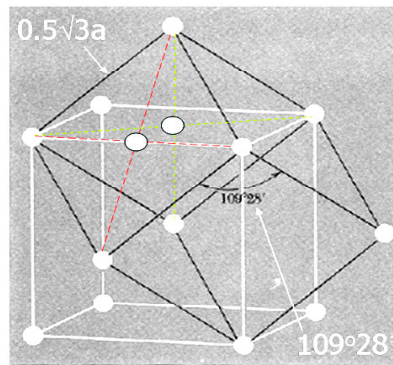


Figure 6-3. O-site in the bcc primitive unit cell.

6.2 Interstitial Disordered Ternary Alloy $\text{Fe}_{1-x-y}\text{Ni}_x\text{C}_y$

As is discussed in Chapter 2 the previous studies of interstitial carbon atoms in $\text{Si}_{1-x}\text{Ge}_x$ alloys [Venezuela--2004], Carbon prefers some O-sites exclusively surrounding the host atoms. Therefore, we can create a ternary alloy $\text{Fe}_{1-x-y}\text{Ni}_x\text{C}_y$ by adding the carbon atoms as interstitial impurities and using the binary alloy $\text{Fe}_{1-x}\text{Ni}_x$ as the host.

Octahedral sites, or O-sites, are the locations for interstitial atoms residing in the interstices between 6 regular atoms that form an octahedron (Figure 6-2). Four of these six atoms are located in a plane, while the other two atoms are positioned above or below the plane in symmetrical positions. Figure 6-2 shows the O-sites of a conventional bcc unit cell. Since all the SQS structures are built from a bcc primitive unit cell, the task is to locate O-sites in a bcc primitive unit cell, from the O-sites in a bcc conventional unit cell. In Figure 6-3, the primitive unit cell is a rhombohedron represented by black lines and the conventional unit cell is a cubic cell represented by white lines. Then the O-sites in the conventional unit cell, represented by white circles with white perimeter, can be projected onto the rhombohedron as shown. These O-sites in the bcc primitive unit cell, represented by white circles with black perimeter, are then located at the centers of its six surfaces, which are parallelograms. Therefore, for the constructed SQS structures, O-sites are located at the centers of identified parallelograms of angles of 109.5° , which are surfaces of the rhombohedron cell.

For the SQS-16 structure of $\text{Fe}_{1-x}\text{Ni}_x$ with $x = 0.125$, all the parallelograms were first identified, as listed in Table 6-7. The first column is the numbering of the parallelogram, the second column lists the four atoms associated with the parallelogram, and the third column lists the angle of the parallelogram. From the above discussions, only those parallelograms of angle 109.5° were considered. The number of these parallelograms is 10. They are labeled by (3-1), (4-1), (5-2), (5-4), (7-1), (7-3), (8-2), (8-3) and (10-1). The centers of these parallelograms are identified as O-sites. The coordinates of these 10 O-sites are listed in the fourth column of Table 6-7.

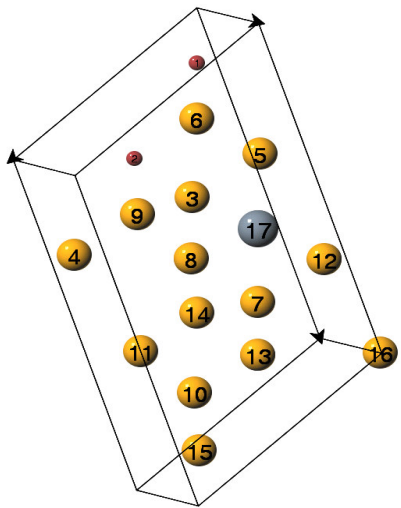
**Table 6-7. Parallelograms and O-sites
in the SQS-16 structure of $\text{Fe}_{1-x}\text{Ni}_x$ with $x = 0.125$.**

Parallelogram	Atoms to construct the parallelogram	Angle between two edges	O-site (Direct Coordinates)
3-1	3-5-7-12	109.5	[1.5 -1 -0.5]
3-2	3-5-10-13	90	
3-3	3-5-4-9	90	
3-4	3-7-8-13	125.3	
3-5	3-5-13-16	148.5	
3-6	3-8-15-16	161.6	
3-7	3-8-10-15	135	
3-8	3-4-7-11	90	
4-1	4-9-11-14	109.5	[2.5 -1 -0.5]
4-2	4-9-10-13	90	
4-3	4-8-11-13	125.3	
5-1	5-6-7-8	54.7	
5-2	5-8-12-13	109.5	[2 -1 -0.5]
5-3	5-7-8-10	125.3	
5-4	5-8-6-9	109.5	[2 -0.5 0]
5-5	5-9-12-14	90	
5-6	5-6-13-14	90	
6-1	6-8-14-15	135	
6-2	6-8-9-11	125.3	
7-1	7-10-12-13	109.5	[2 -1.5 -0.5]
7-2	7-11-12-14	90	
7-3	7-8-10-11	109.5	[2 -1.5 0]
7-4	7-8-13-14	125.3	
7-5	7-10-13-15	125.3	
8-1	8-11-12-13	125.3	
8-2	8-11-13-15	109.5	[2.5 -1.5 0]
8-3	8-9-13-14	109.5	[2.5 -1 0]
8-4	8-9-10-11	109.5	
8-5	8-10-14-15	90	
9-1	9-11-14-15	125.3	
10-1	10-11-13-14	109.5	[2.5 -1.5 0]

Two O-sites, labeled by (5-4) and (7-1), are unfavorable, since nickel atoms, not just the host iron atoms, surround them. Among the rest of O-sites, the one with the longest distance to the nickel atoms is favorable and therefore selected as the locus of the carbon impurity. This O-site is in parallelogram (2-1). Then a ternary alloy $\text{Fe}_{0.82}\text{Ni}_{0.12}\text{C}_{0.06}$ can be constructed and represented by a $\text{Fe}_{14}\text{Ni}_2\text{C}_1$ supercell. The relaxed supercell structure from the ideal $\text{Fe}_{14}\text{Ni}_2\text{C}_1$ supercell is listed in Table 6-8. The densities

predicted by various approximation methods are listed in Table 6-6. As is seen, introducing C as a third constituent increases the density, in comparison to that of binary alloy $\text{Fe}_{14}\text{Ni}_2$.

Table 6-8. Relaxed supercell $\text{Fe}_{14}\text{Ni}_2\text{C}_1$ of NM order.

Relax Supercell $\text{Fe}_{14}\text{Ni}_2\text{C}_1$ ---- by PBE_PAW	Relaxed SQS-16 Structure with one Carbon atom as impurity at an O-site			
	Lattice vectors:			
	a1=[3.636006964	1.712629603	-1.21986628]	
	a2=[3.626223959	-1.710267041	3.62850238]	
	a3=[2.426662194	-6.842193059	-2.42861559]	
	Ni	2.415881	0.001457	-0.010768
	Ni	3.624079	-1.686649	1.222281
	Fe	2.325594	-3.401255	0.086137
	Fe	4.797885	-3.421450	2.404535
	Fe	3.622719	-1.571093	-1.256847
	Fe	4.828206	0.005328	-0.007336
	Fe	3.638601	-5.262575	-1.206852
	Fe	4.948941	-3.420450	0.090864
	Fe	6.042633	-1.689511	1.167683
	Fe	4.829285	-6.836295	0.036712
	Fe	5.972862	-5.147092	1.103636
	Fe	4.927764	-3.446720	-2.529746
	Fe	6.122969	-5.145137	-1.209543
Fe	7.280126	-3.429536	-0.015129	
Fe	7.287119	-6.851158	-0.053881	
Fe	6.061307	-5.129829	-3.633853	
C	3.639055	-3.416453	-1.205662	

6.3 Approximations & Convergences

Approximations: As discussed in Chapter 5, PBE and PW91 exchange-correlation functional are chosen. The PAW and Hubbard-U methods are used for the studies of iron. The investigations of these methods of approximations are used in the studies of alloys. For nickel, $3d^84s^2$ chosen as valence electrons and its pseudopotential was generated with outmost cutoff radius of 2.3\AA and cutoff radius for local potential 1.681\AA respectively, with a core radius of 2.808\AA for projector operators. For carbon, $2s^22p^2$ are chosen as

valence electrons and its pseudopotential was generated with outmost cutoff radius of 1.5Å respectively, with a core radius of 2.266Å for projector operators.

Convergences: (1) The studies of the selection of the energy precision control parameters, i.e. EDIEF and EDIEFG, for electronic and ionic steps, are listed in Table 6-9. It can be seen that the energy convergence from the setting EDIFF = 10^{-4} eV and EDIFFG = 10^{-3} eV are close to those from EDIFF= 10^{-7} and EDIFFG= 10^{-6} , up to the fifth decimal. Therefore EDIFF= 10^{-4} and EDIFFG= 10^{-3} have sufficient accuracy to be selected as the constraints for the further calculation.

(2) The listed values for cut-off energies in the pseudopotentials of nickel, iron and carbon are ENMAX_{Fe}=267.969ev, ENMAX_{Ni}=269.618ev, and ENMAX_C=400ev. Among these three cut-off energies, the maximum value 400 eV was chosen. Therefore, ENCUT is set to be 400 eV for the entire calculations. Higher values of ENCUT were investigated and the results are listed in Table 6-9.

(3) The k-point meshes for Brillouin zone sampling were constructed by Monkhorst-Pack scheme. The k-points are selected to be 4, 6, 8 and 9 for the convergence testing. Table 6-11 shows KPOINTS=6x6x6 gives the lowest energy, which means KPOINTS=6x6x6 provides the most stable status. We then chose MK K-mesh at 6x6x6 for the calculations.

Table 6-9. Accuracy and convergence comparison to EDIFF & EDIFFG at KPOINT=6 & ENCUT=400.

KPOINT=6	Nonmagnetic Case	
ENCUT=400	EDIFF=E-07 & EDIFFG=E-06	EDIFF=E-04 & EDIFFG=E-03
Energy (ev)	-153.308592	-153.308553
Volume	160.74	160.74

Table 6-10. NM accuracy and convergence comparison for ENCUT at KPOINT=6 and EDIFF=10⁻⁴ & EDIFFG=10⁻³

NM case	EDIFF=E-04 & EDIFFG=E-03	
KPOINT=6	Energy (ev)	Volume
ENCUT=400	-153.308553	160.74
ENCUT=450	-153.283665	160.74
ENCUT=500	-153.281608	161.13
ENCUT=550	-153.280586	160.74

Table 6-11. NM accuracy and convergence test for KPOINT at ENCUT=450ev and EDIFF=10⁻⁴ & EDIFFG=10⁻³.

NM case	EDIFF=E-04 & EDIFFG=E-03	
ENCUT=450ev	Energy (ev)	Volume
KPOINT=4	-153.269205	160.74
KPOINT=6	-153.283665	160.74
KPOINT=8	-153.275994	160.74
KPOINT=9	-153.275254	160.74

6.4 EOS and Magnetic Properties

The ab initio calculations are conducted to find the ground-state EOS for binary alloy Fe_{1-x}Ni_x and the ternary alloy Fe_{1-x-y}Ni_xC_y. As discussed, both alloys have a bcc

based structure. For each alloy, either a nonmagnetic or ferromagnetic phase is considered. The magnetic order for each alloy is first identified by comparing the ground-state energies. Then the EOS for each alloy is found based on the predicted magnetic order. All the details are listed in tables and figures.

6.4.1 Binary Alloy $\text{Fe}_{1-x}\text{Ni}_x$

(1) Hubbard_U overestimates the magnetic moments at bcc, fcc and hcp of iron in Chapter 5 and there is a disagreement with experiments in the hcp NM order [Williamson—1972, Cort—1982, Nasu—2002, Taylor--1991]. Due to these disagreements, Hubbard_U was not selected to predict the binary alloy and the ternary alloy [see the section 5.3.4.1]. By using a combination of PBE and PAW approximations, we first relaxed the ideal SQS-16 structure. The relaxed equilibrium structure of a NM bcc supercell is shown in Table 6-5. By scaling the volume of supercell, with relaxed lattice shape and ion positions, the ground-state energies at each selected volume was calculated. The results of ground state energies and magnetic moments vs. density (and pressure) are shown in Figure 6-4 and Figure 6-5. From Figure 6-4a, it is not clear to see the FM phase gives a lower energy in comparison to that of a NM phase at low density. But in Figure 6-4b, at lower pressure, it can be seen that the FM phase provides a lower energy. This is also in agreement with the experiment. With the pressure increasing, the energy of the NM phase becomes lower which means more pressure results in the loss of magnetic phase. Therefore, PBE_PAW method predicted a FM phase for binary $\text{Fe}_{1-x}\text{Ni}_x$ with composition $x = 0.125$ at low pressure and NM at high pressure. From Figure 6-5, for the FM phase, each one of 16 atoms in the SQS-16 structure has a different magnetic moment. The magnetic moment of iron atoms are around $2\mu_B$, which are slightly lower

than that of bcc FM iron. However, nickel atoms have much lower magnetic moment, at about $0.5\mu_B$. It means that the introduction of the nickel, at a low concentration like $x = 0.125$, brings down the magnetic moment.

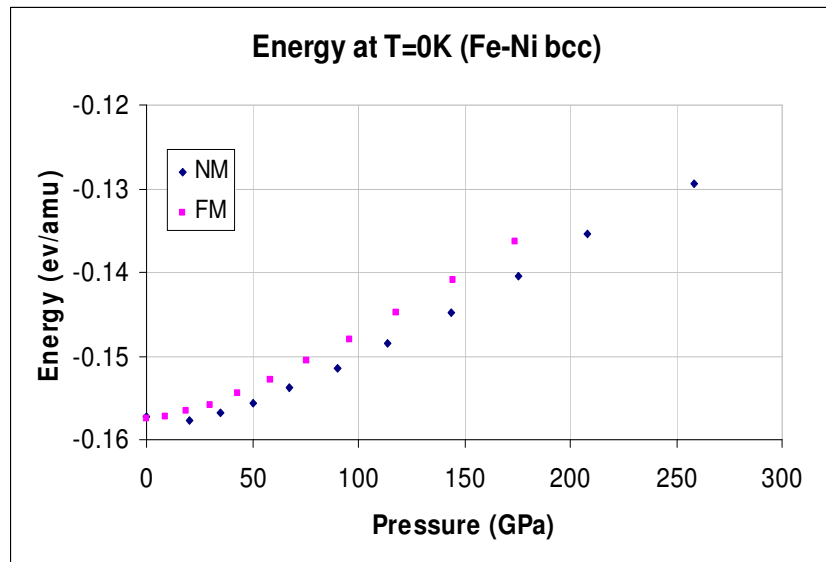
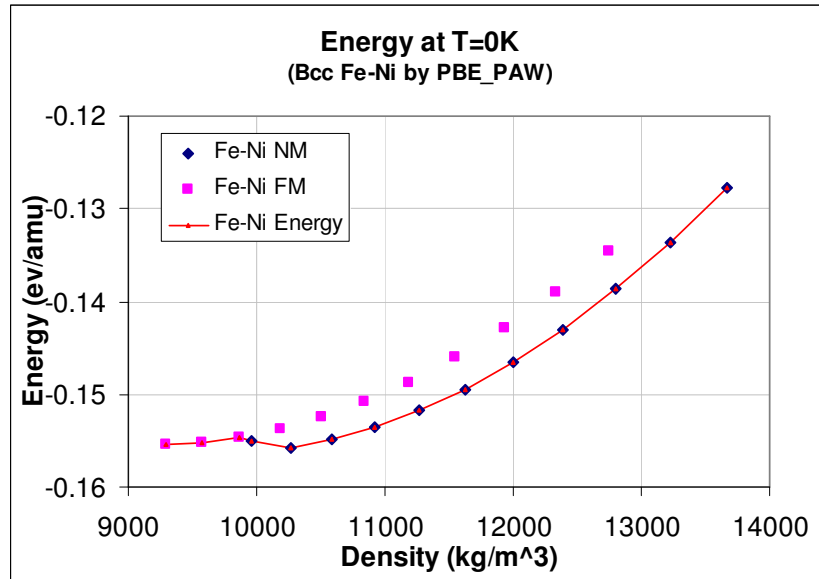


Figure 6-4. (a) Ground state energies of bcc $Fe_{1-x}Ni_x$ vs. density (by PBE with PAW). (b) Ground state energies of bcc $Fe_{1-x}Ni_x$ vs. pressure (by PBE with PAW).

(2) By using a combination of PW91 and PAW approximations, the same calculations were repeated. The results of ground state energies and magnetic moments vs. density, are shown in Figure 6-6 and Figure 6-7. From Figure 6-6, PW91_PAW predicts that the FM phase has a slightly lower energy than NM phase. PW91_PAW predicts that FM is stable. From Figure 6-7, we obtained a similar prediction. The magnetic moments are slightly smaller than those predicted by PBE_PAW.

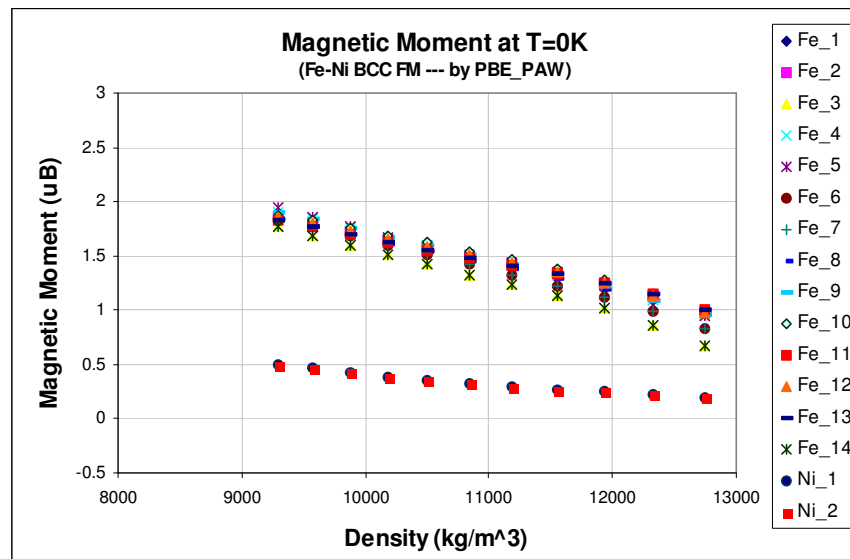


Figure 6-5. Magnetic moment of bcc Fe_{1-x}Ni_x vs. density (by PBE with PAW).

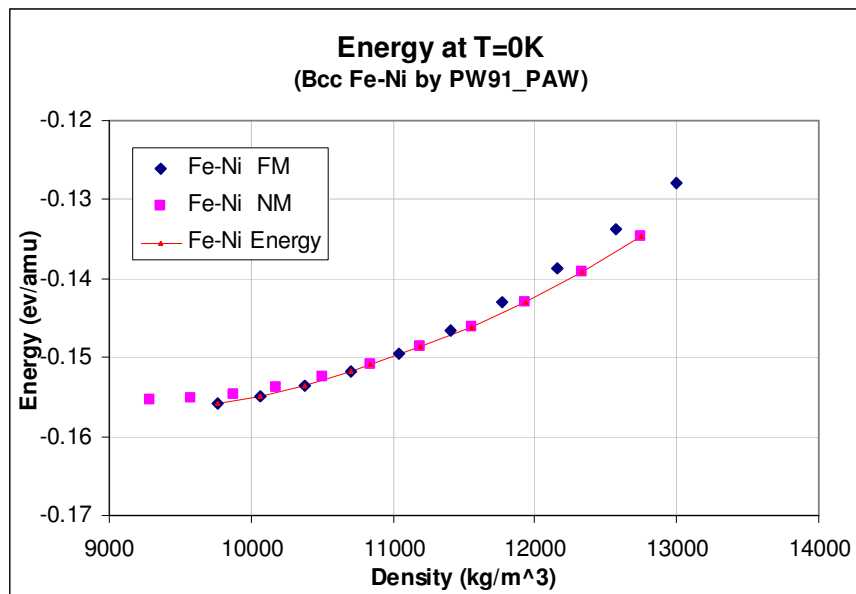


Figure 6-6. Ground state energies of bcc Fe_{1-x}Ni_x vs. density (by PW91 with PAW).

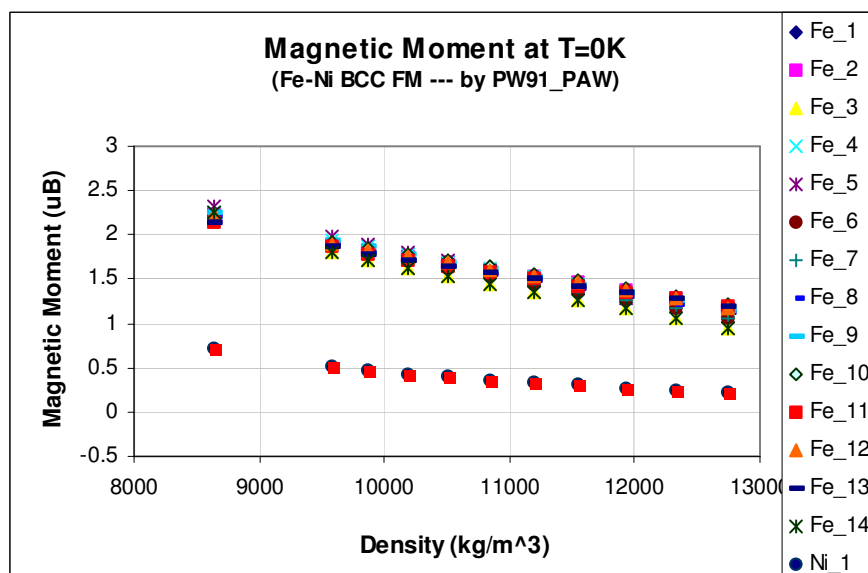


Figure 6-7. Magnetic moment of bcc Fe_{1-x}Ni_x vs. density (by PW91 with PAW).

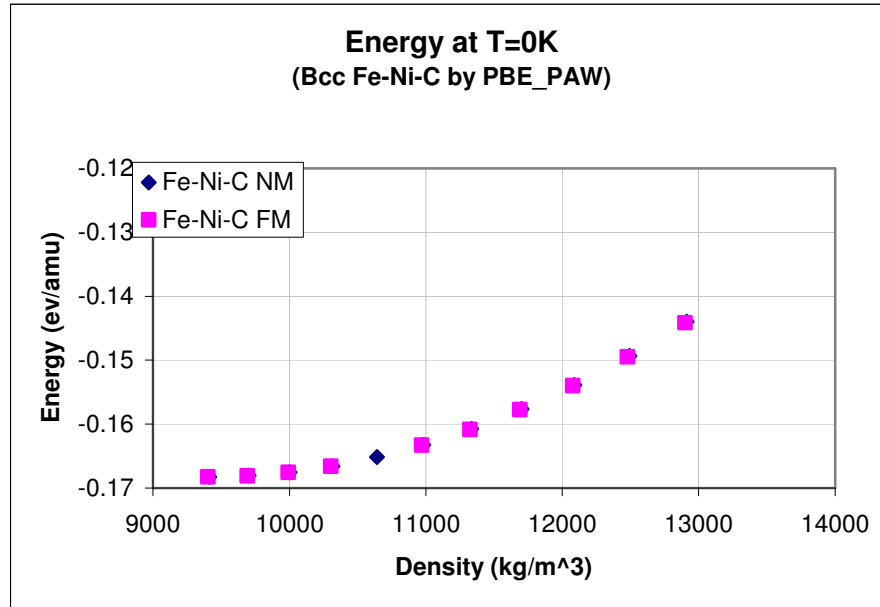


Figure 6-8. Ground state energies of bcc Fe_{1-x}Ni_xC_y vs. density (by PBE with PAW).

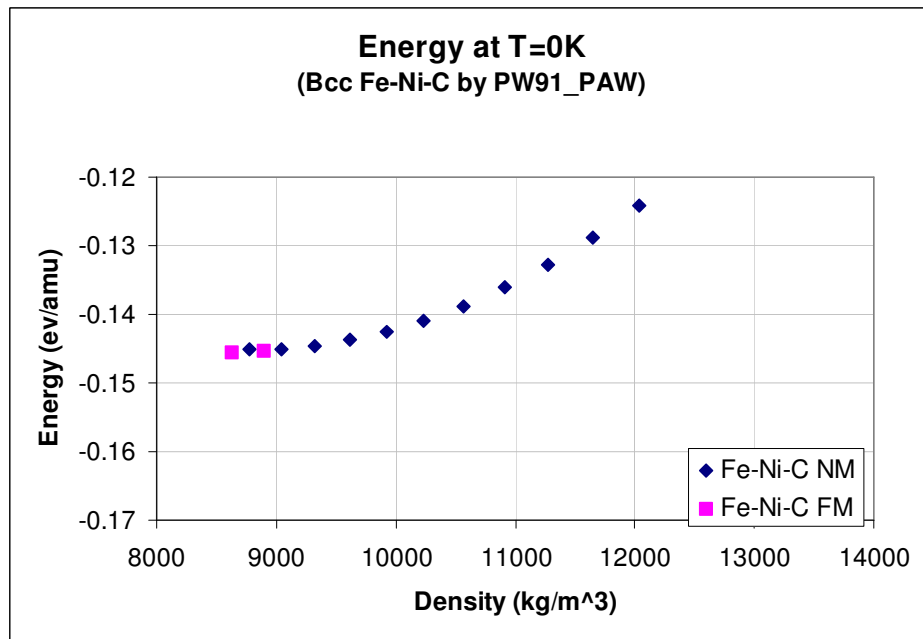


Figure 6-9. Ground state energies of bcc Fe_{1-x}Ni_xC_y vs. density (by PW91 with PAW).

6.4.2 Ternary Alloy $\text{Fe}_{1-x-y}\text{Ni}_x\text{C}_y$

(1) By using a combination of PBE and PAW approximations, the ideal $\text{Fe}_{14}\text{Ni}_2\text{C}_1$ structure was first relaxed. The relaxed equilibrium structure of a NM order is shown in Table 6-8. By scaling down the volume of supercell, however, with relaxing the lattice shape and ion positions, we calculated the ground-state energies at each selected volumes. The results of ground state energies vs. density, are shown in Figure 6-8. We can see that a NM and FM phase have identical energies. This can be explained by the following observations: An initial FM phase collapses to a NM phase, after a full relaxation. Therefore, PBE_PAW method predicted only a NM phase available for ternary alloy $\text{Fe}_{14}\text{Ni}_2\text{C}_1$. This means that the introduction of the carbon as impurity eliminates the FM phase.

(2) By using a combination of PW91 and PAW approximations, we implemented the same calculations. Similar predictions are observed and shown in Figure 6-9.

6.4.3 EOS of Binary Alloy $\text{Fe}_{1-x}\text{Ni}_x$ and Ternary Alloy $\text{Fe}_{1-x-y}\text{Ni}_x\text{C}_y$

The magnetic phase for both binary alloy $\text{Fe}_{1-x}\text{Ni}_x$ and ternary alloy $\text{Fe}_{1-x-y}\text{Ni}_x\text{C}_y$ are developed in the last two sections. For both alloys, in comparison to a FM phase, we found that a NM phase is favorable for the ternary alloy, and a FM phase is favorable for the binary alloy. The EOS ($T=0\text{K}$) for a binary alloy $\text{Fe}_{1-x}\text{Ni}_x$ in a FM order and a ternary alloy $\text{Fe}_{1-x-y}\text{Ni}_x\text{C}_y$ also in a NM order are presented in Figure 6-10 and compared to the EOS of bcc FM iron. The following observations are made:

- Both alloys are stiffer than the pure iron.
- The binary alloy $\text{Fe}_{1-x}\text{Ni}_x$ with $x = 0.125$ is stiffer than ternary alloy $\text{Fe}_{1-x-y}\text{Ni}_x\text{C}_y$ with $x = 0.12$ and $y = 0.06$.
- PBE_PAW predicted EOS are stiffer than those predicted by PW91_PAW.

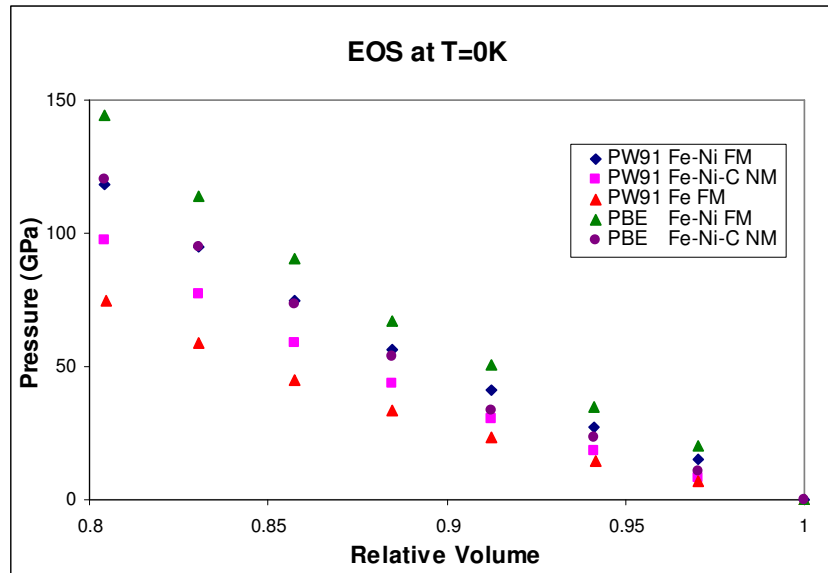


Figure 6-10. EOS of bcc Fe, $\text{Fe}_{1-x}\text{Ni}_x$ and $\text{Fe}_{1-x-y}\text{Ni}_x\text{C}_y$ vs. relative volume (by PW91 with PAW).

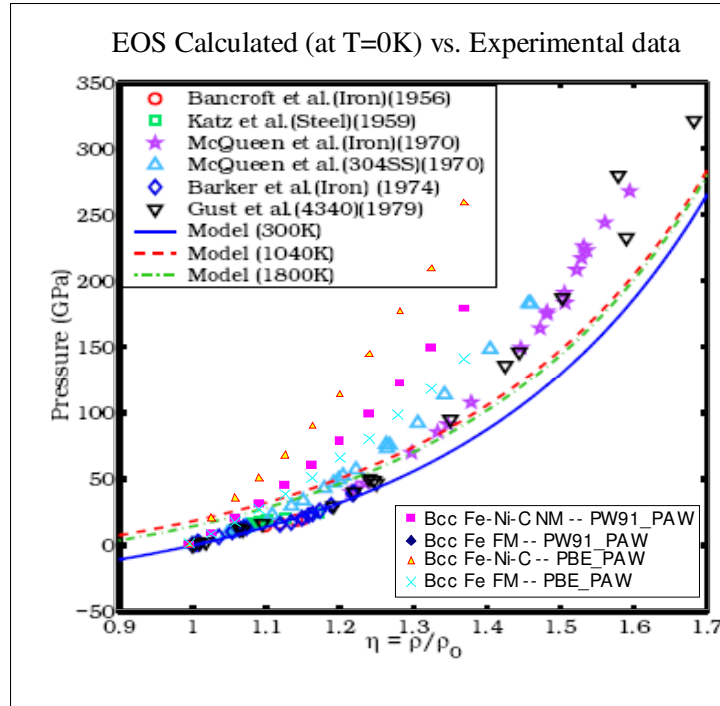


Figure 6-11. EOS calculated (at T=0K) vs. experimental data [Biswajit--2005].

6.4.4 Thermodynamical EOS for the Binary Alloy $\text{Fe}_{1-x}\text{Ni}_x$ and the Ternary Alloy $\text{Fe}_{1-x-y}\text{Ni}_x\text{C}_y$.

Unlike the previous mixing model introduced in Chapter 2, in this thesis, the thermodynamical EOS ($T=300\text{K}$) of Bcc FM $\text{Fe}_{1-x}\text{Ni}_x$ is directly investigated by PBE combined with PAW to the substitutional disordered binary lattice structure. The thermodynamical EOS ($T=300\text{K}$) of BCC NM $\text{Fe}_{1-x-y}\text{Ni}_x\text{C}_y$ is directly investigated by PW91 combined with PAW to the interstitial disordered ternary lattice structure. The contribution of lattice thermal energies $e_l(v,T)$ comes from the thermal excitation of ions, which is calculated from phonon modes of the lattice [Baroni—2001].

For the binary alloy $\text{Fe}_{1-x}\text{Ni}_x$, the discrete values 1, 0.99, 0.98, 0.96 and 0.94 were fixed for the lattice volume ratio. Forces were calculated by perturbing the non-

equivalent displacing ion from its equilibrium positions. Total 16 non-equivalent displacement of ions are given in phonon analysis. A triclinic supercell is created for bcc $\text{Fe}_{1-x}\text{Ni}_x$. Lattice constants are $a_1=4.3041105521\text{\AA}$, $a_2=5.576169432\text{\AA}$ and $a_3=7.75334444\text{\AA}$. The angles between each two lattice vectors are $\alpha=74.8518\text{deg}$, $\beta=74.10375\text{deg}$, and $\gamma=89.295\text{deg}$. The displacement of each ion in the supercell is chosen to be 0.01\AA in three independent directions: (1 0 0), (0 1 0) and (0 0 1). By using the forces calculated by the ab initio package VASP, the phonon modes and dispersion curves are calculated from the PHONON software package. The sequence of standard labels C# (0 0 0), X (0.5 0 0), K (0 0.5 0) is used to denote symmetry points in the Brillouin Zone for the supercell.

For the ternary alloy $\text{Fe}_{1-x-y}\text{Ni}_x\text{C}_y$, the discrete values 1, 0.99, 0.98, 0.96 and 0.94 were fixed for the lattice volume ratio. Similar to the binary alloy $\text{Fe}_{1-x}\text{Ni}_x$, forces were calculated by perturbing the non-equivalent displacements of ions from its equilibrium positions. Carbon and Nickel (numbered 3) as non-equivalent displacements of ions are given to phonon analysis. A triclinic supercell is created for bcc $\text{Fe}_{1-x-y}\text{Ni}_x\text{C}_y$. Lattice constants are as same as those of the binary alloy $\text{Fe}_{1-x}\text{Ni}_x$, $a_1=4.3041105521\text{\AA}$, $a_2=5.576169432\text{\AA}$ and $a_3=7.75334444\text{\AA}$. The angles between each two lattice vectors are also as same as those of the binary alloy $\text{Fe}_{1-x}\text{Ni}_x$, $\alpha=74.8518\text{deg}$, $\beta=74.10375\text{deg}$, and $\gamma=89.295\text{deg}$. The displacement of each of these two ions in the supercell is chosen to 0.01\AA in three independent directions: (1 0 0), (0 1 0) and (0 0 1). The sequence of standard labels C# (0 0 0), X (0.5 0 0) is used to denote symmetry points in the Brillouin Zone for the supercell.

From the previous studies, FM is predicted to be stable to the bcc binary alloy $\text{Fe}_{1-x}\text{Ni}_x$ at low pressure and low temperature. No AFM exists in the iron alloy with very low Ni concentration. The EOS ($T=300\text{K}$) for $\text{Fe}_{1-x}\text{Ni}_x$ in a FM order is obtained (Figure 6-12) by PBE_PAW to compare with EOS ($T=0\text{K}$) for $\text{Fe}_{1-x}\text{Ni}_x$ in a FM order. The EOS ($T=300\text{K}$) for $\text{Fe}_{1-x-y}\text{Ni}_x\text{C}_y$ in a NM order is obtained (Figure 6-13) by PW91_PAW to compare with EOS ($T=0\text{K}$) for $\text{Fe}_{1-x-y}\text{Ni}_x\text{C}_y$ in a NM order. It can be observed that (1) in comparison to the cold-curve EOS, the 300K thermal curve moves upward, which means at the same density, 300K main sustain more pressure than 0K; (2) For the binary alloy $\text{Fe}_{1-x}\text{Ni}_x$ and the ternary alloy $\text{Fe}_{1-x-y}\text{Ni}_x\text{C}_y$, each of the EOS at $T=300\text{K}$ has a slightly lower stiffness than the EOS at $T=0\text{K}$, which means that with a temperature increase, the stiffness (slopes) is getting lower and therefore the material is getting softer. This can be used to partially explain the material removal from the nose tip area when erosion occurs in the region.

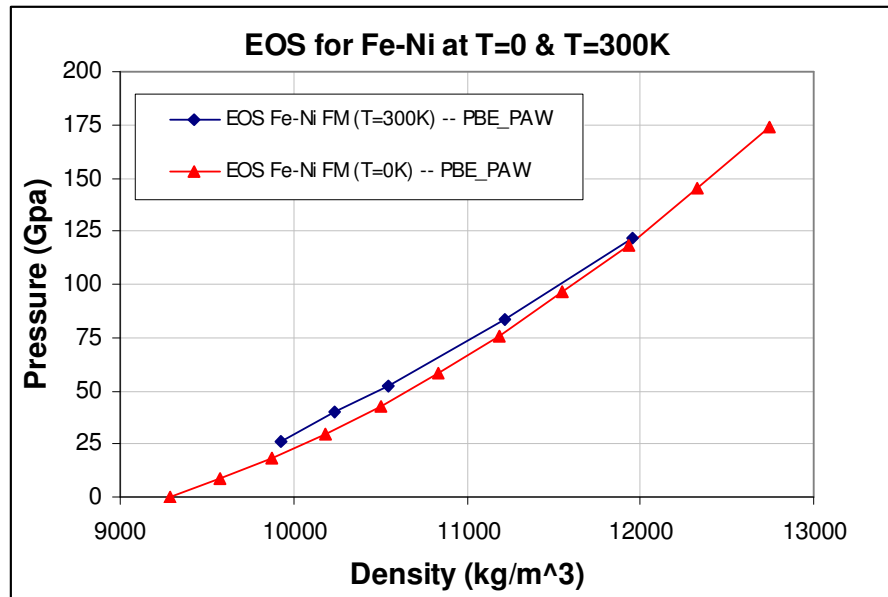


Figure 6-12. EOS for the binary alloy $\text{Fe}_{1-x}\text{Ni}_x$ at $T=0\text{K}$ and $T=300\text{K}$.

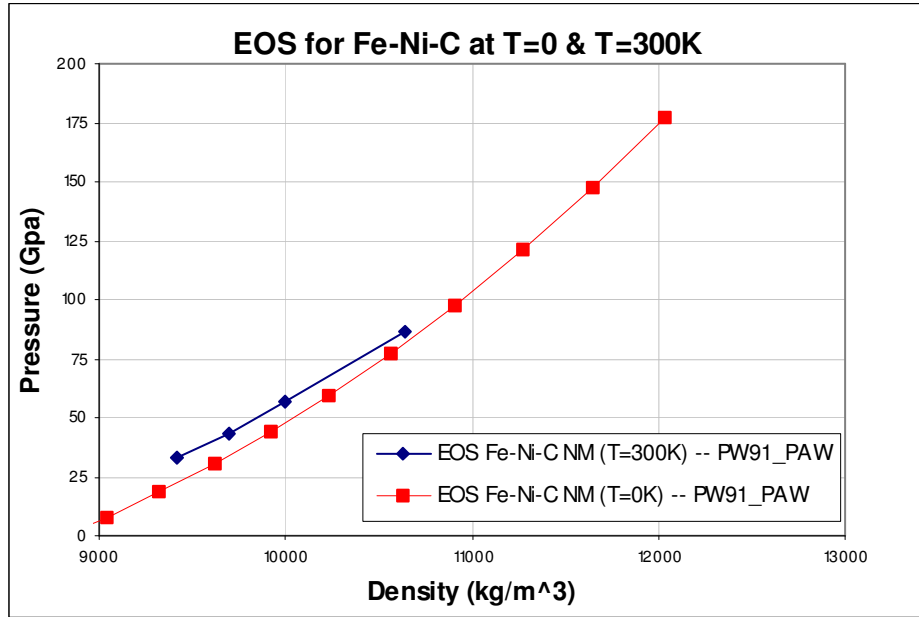


Figure 6-13. EOS for the ternary alloy $\text{Fe}_{1-x-y}\text{Ni}_x\text{C}_y$ at $T=0\text{K}$ and $T=300\text{K}$.

6.4.5 Effects of Nickel and Carbon as Constituents

Magnetic Effects: the FM phase of the binary alloy Fe-Ni is compared for the magnetic moments to pure iron in order to investigate on the effects of species nickel and carbon. The comparison is shown in Figure 6-14. From these predictions, we can see that (1) nickel can bring down the magnetisms when adding to pure iron at a low concentration; (2) carbon can destroy the magnetisms.

Concentration Effects: Hong [Hong—1989] used a single-band Hubbard Hamiltonian with the Hartree-Fock approximation to investigate the concentration dependence of the magnetization of the disordered FM alloy $\text{Fe}_{1-x}\text{Ni}_x$. He suggested that the binary alloy $\text{Fe}_{1-x}\text{Ni}_x$ with the low concentration (less than 20% Nickel) would have a FM order in bcc structure. According to his conclusion, the investigation to the binary alloy $\text{Fe}_{1-x}\text{Ni}_x$ shown in this thesis will be concentrated on FM and NM orders to bcc.

Moreover, bcc is also the favorable structure to the binary alloy $\text{Fe}_{1-x}\text{Ni}_x$ with the low concentration at the low temperature.

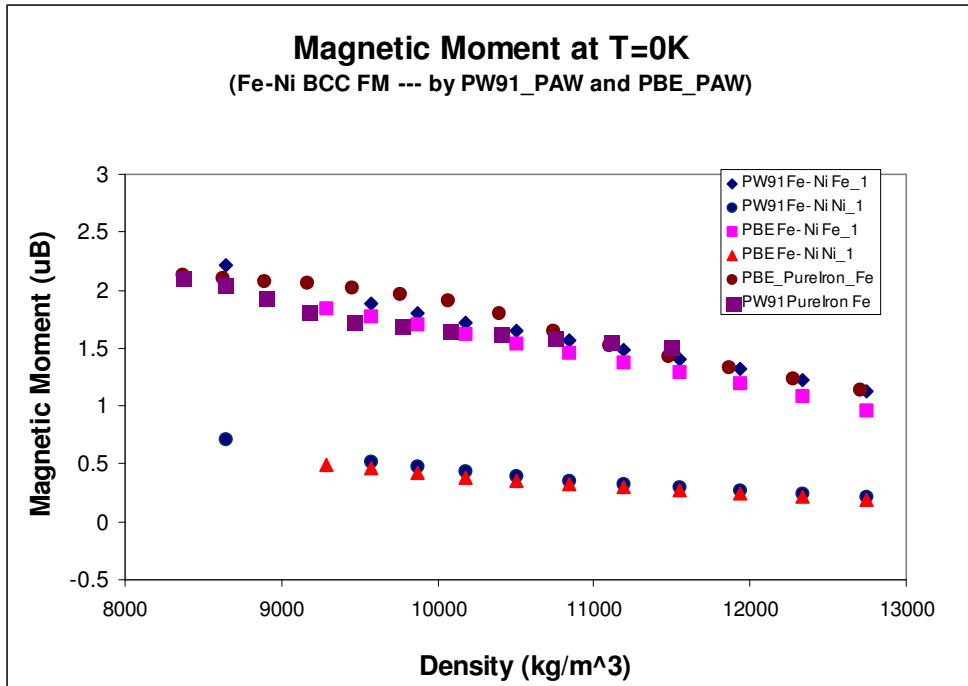


Figure 6-14. Magnetic moments of bcc Fe and $\text{Fe}_{1-x}\text{Ni}_x$ vs. relative volume (by PBE with PAW & PW91 with PAW).

CHAPTER 7

CONCLUSION & FUTURE WORK

7.1 Conclusions

For purposes of preliminary design of projectiles that should penetrate hard targets at high striking velocities, it is possible to obtain reasonably accurate results by using approximate simplified models. These models require integration of nonlinear ordinary integro-differential equations instead of complicated set of three-dimensional partial differential equations, with equations of conservation of mass, momentum and energy and constitutive equation. Results of the approximate model can yield information on possible phase changes, blunting of the nose, material removal from the nose and shortening of the nose. When these equations are combined with the cylindrical shank (Walker-Ardenson's model) it is possible to obtain shock loading effect on the shank. This information on the loading can be used to design the target loads in the shank, including the use dual functional structural energetic materials that can provide the penetration resistance when needed and additional energetic characteristics when needed.

By using the developments of the second part of the thesis, it is possible to obtain the thermo-mechanical equations of state of the projectile materials that are used in the nose region. The developments eliminate costly experiments and are strictly based on the use of first principles or ab initio methods. Such a procedure, with modifications, can be used to design erosion resistant alloys that can be used to design the nose of an impacting

projectile that are capable of a successful performance at high striking velocities, with hard targets.

7.2 Future Work

The future work should formulate simplified penetration model with equation of the mass conservation and the new plasticity model with phase transition in two-dimensional axisymmetric penetration penetrators. Moreover, bending problem of the projectile at high velocity striking should also be investigated. The future work should also include the investigation of the buckling and bending problems of the projectile.

The ab initio models should be modified to include phase transition (including melting) and plasticity effects. The models should consider different alloying elements that are considered today and new elements that can improve the penetration performance with minimal nose erosion. The ab initio methods should be developed as a design tool to develop future alloys for other different applications.

The ab initio model and the simplified model for penetration should be combined with the Walker-Ardenson cylindrical projectile model, to evaluate loads in the shank of the projectile, with an alloy nose. Such a procedure can be used to evaluate the use of dual functional structural energetic materials that can provide penetration resistance through hard targets and increased energetic characteristics following the penetration of a hard target.

CHAPTER 8 APPENDIX

8.1 Ising Models

Ising Model [Kikuchi--1951] is a mathematical model in statistical mechanics. The name came from the physicist Ernst Ising. The model can be represented on a figure that consists of possible configurations. As a first step in the alloy problem, Ising Model has to be presented in details so that we may easily introduce the cluster expansion. We may utilize a 1-D model, a 2-D model and a 3-D model to give a thorough description to this concept.

8.1.1 1-D Ising Model

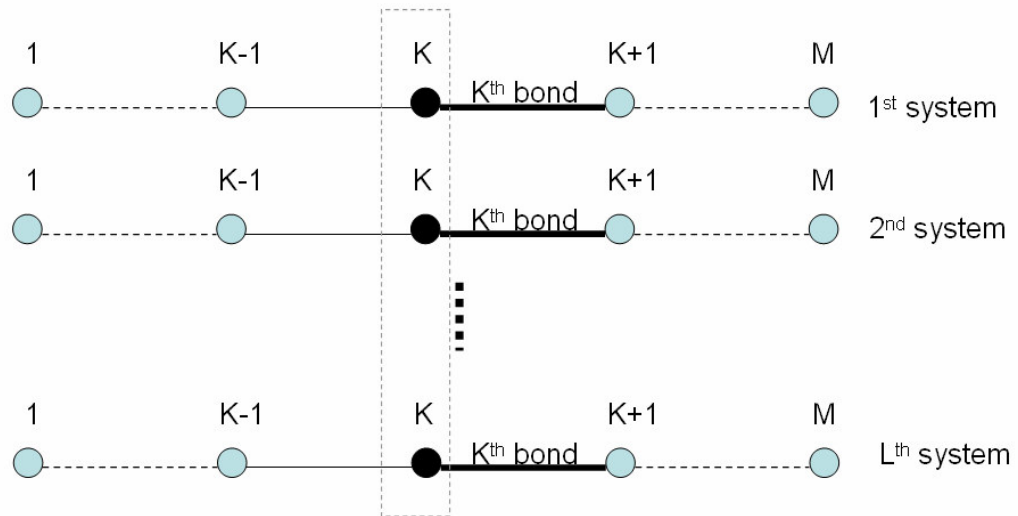


Figure 8-1. An ensemble of linear lattices [Kikuchi--1951].

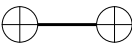
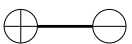
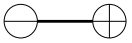
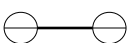
Let us consider an ensemble that consists of L systems. The system definition here is a linear lattice composed of M lattice points. Figure 8-1 gives the image of the ensemble.

The set of kth lattice point is a group of points marked in black and named “K”. The set of the kth bond is a group of bonds marked with heavy lines and named “k”. For 1-D linear Ising model, the configurations are showed in the Figure 8-1.

-1 or +1 is assigned to each vertex in the configuration. β_i indicates the number of different configurations that have the same probability, where the configuration (- +) is assumed to have the same probability as the configuration (+ -). y_i represents the probability of the ith configuration and satisfies

$$\sum_1^3 \beta_i y_i = 1. \quad (8.1.1-1)$$

Table 8-1. Probabilities of appearance of configurations of a bond [Kikuchi--1951].

Bond	Prob.	β_i
	y_1	1
 	y_2	2
	y_3	1

Therefore, here is the statement:

The set of the kth bond has right distribution of spin.

That is to say, y_1L has the configuration (+ +), y_2L has the configuration (+ -) or (- +), and y_3L has the configuration (- -).

Therefore, to the lattice points, we may have the probabilities of appearance of spins

Table 8-2. Spins and Probability [Kikuchi--1951].

Spin	Probability
+	$x_1=y_1+y_2$
-	$x_2=y_2+y_3$

Table 8-2 means x_1L has (+) spins and x_2L has (-) spins. Similarly, we may say “the set of the k^{th} lattice points has right distribution of spins.” Obviously, $x_1L+x_2L=1$, thus, when the set of a bond has right distribution of spins, each end lattice point of the k^{th} lattice bond naturally has right distribution of spins, too. Now, here is the question:

What will be the number of ways of putting a spin on A point so that the bond B-A has right distribution of spin?

By giving a linear Ising lattice (Figure 8-2), we have the spin selection tree in

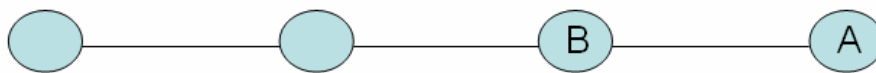


Figure 8-2. An intermediate stage of constructing a linear Ising Lattice [Kikuchi--1951].

If B is assumed to have right distribution of spins, then we will fill A under the request of the bond B-A having right distribution of spins also.

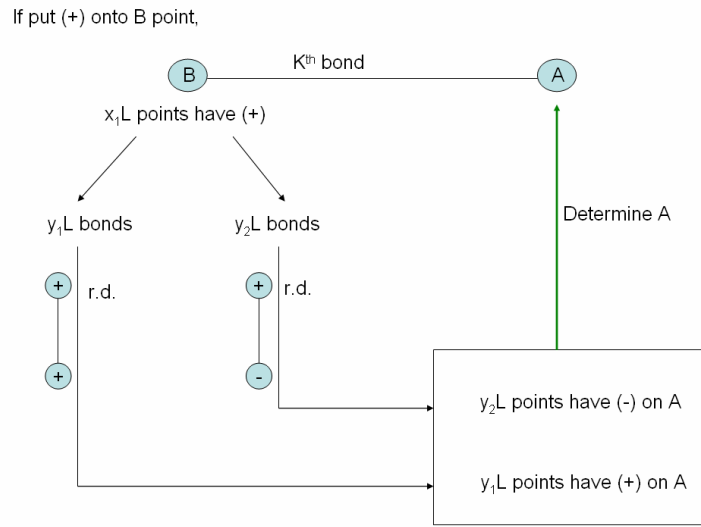


Figure 8-3. spin selection tree(1)

When spin up (+) is assigned to the K^{th} lattice point, from Table 8-2, we may know the possibility with spin up on B is x_1L , therefore, in order to impose right distribution of spins on the k^{th} bond ($B \rightarrow A$), we need to obey the probabilities of appearance of configuration of a bond. From Table 8-1, we know the probability to put the spin up (+) on A under the restriction of the prescribed spin-up (+) of B is y_1L , and the probability to put the spin down (-) on A under the restriction of the prescribed spin-up (+) of B is y_2L .

Similarly, we may calculate out the probability to put (+) on A when the spin-down (-) is assigned to B is y_2L and the probability to put (-) on A when the spin-down (-) is assigned to B is y_3L .

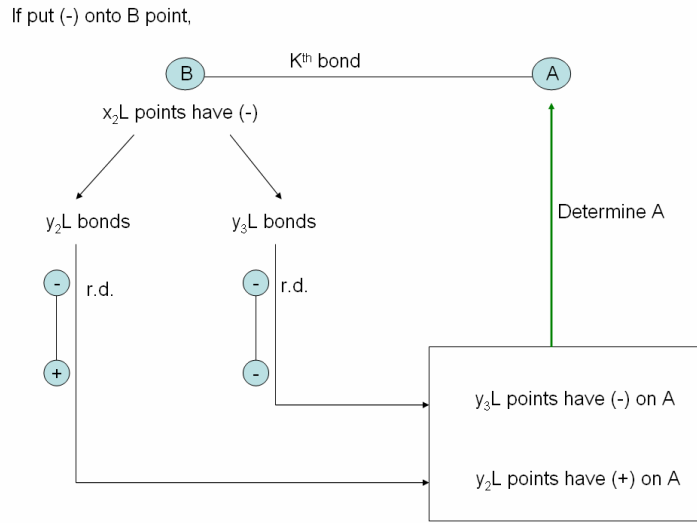


Figure 8-4. spin selection tree(2).

Based on the above analysis, it is obvious that A has right distribution of spins because the lattice point A satisfies the equation (8.1.1-1).

Ryoichi Kikuchi presented the equations to count the number of ways of putting a spin on A so that the k^{th} bond $B \rightarrow A$ has right distribution of spins. Briefly, the number of ways to put the spin-up (+) on A is

$$g_1 = (x_1 L)! / [(y_1 L)! (y_2 L)!] \quad (8.1.1-2)$$

The number of ways to put the spin-down (-) on A is

$$g_2 = (x_2 L)! / [(y_2 L)! (y_3 L)!] \quad (8.1.1-3)$$

The number of ways to put a spin on A so that $B \rightarrow A$ has r.d. is

$$G_L = g_1 g_2 \quad (8.1.1-4)$$

Remember this is only for one lattice point, for M lattice points in a 1-D linear system, $(G_L)^M$ is the number required for the ensemble. The number of ways for one

system G is the L^{th} root of $(G_L)^M$. Refer to Stirling's formula, the entropy of a system is obtained as $S = k \ln(G_L)^{M/L}$, where S is the entropy for a system. The free energy may be obtained from the calculated total energy and the entropy, there we may minimize the free energy to give the equilibrium states.

8.1.2 2-D square lattice – Bethe's approximation

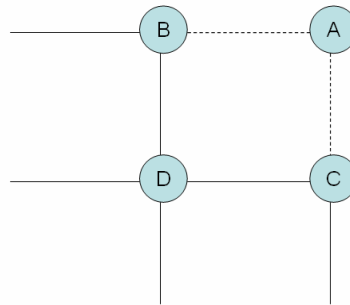


Figure 8-5. 2-D Ising Model [Kikuchi--1951].

The goal of Bethe's approximation is similar to the 1-D Ising Model. It will calculate the number of ways to put a spin on A so that the bond $B \rightarrow A$ and $C \rightarrow A$ both have right distribution of spins.

It takes advantages of the basic bond configurations of 1-D linear Ising Model. Table 8-1 and Table 8-2 will also be used to this 2-D approach. Briefly, there are three steps needed to find the number.

1. Utilize the 1-D linear Ising model to find the number of ways of putting a spin on A so that the bond $B \rightarrow A$ has right distribution of spins. Here we have to remember there is no relation to $C \rightarrow A$ when we count this step. The number is equal to G_L in the 1-D linear Ising model.

2. Obviously the assumption in step-1 about no relation to $C \rightarrow A$ is not correct. A correction needs to be given to the procedure. The key point here is to find out the probability of $C \rightarrow A$ having right distribution spins after the step-1. The probability of $C \rightarrow A$ having r.d. is $\Gamma = G_L / A_L$, where A_L is the number of ways to put a spin on A without considering C, and G_L also represents the probability of the bond $C \rightarrow A$ having r.d.
3. As an approximation, the number of ways to put a spin on A is $G_L * \Gamma$.

Then follow the left steps in 1-D linear Ising model to obtain the equilibrium state.

8.1.3 3-D Ising Model – Simple Cubic Lattice

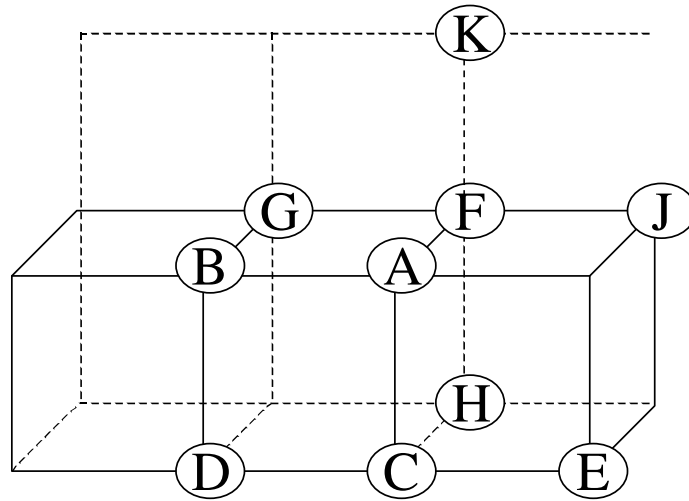


Figure 8-6. An intermediate stage of constructing a simple cubic lattice [Kikuchi--1951].

Based on the 2-D Bethe's approximation, we may extend it to build 3-D Ising Model. The shortest way is to take the two dimensional square basic configurations, therefore all tables used in 1-D Ising model and 2-D Ising model are needed here. The goal is to determine the number of ways of putting a spin on the lattice point A so that all

squares and angles including A will have r.d., then utilize the number of ways to obtain the entropy of a system.

The following steps have to be applied:

4. According to 2-D Kramers-Wannier [Kikuchi—1951] approximation, in square F-G-B-A, with respect to the angle FGB, the number of ways to put a spin on A so that F-G-B-A has r.d. is

$$G_1 = \frac{\{\angle FGB\}_L}{\{\text{Square } FGBA\}_L} \quad (8.1.3-1)$$

Now, consider the square A-B-D-C, we will put a spin on A with respect to the angle BDC so that the square A-B-D-C has the r.d.. Here the bond B→A is also contained in the square F-G-B-A that has r.d. already, therefore, the correction factor is

$$\Gamma_1 = \frac{\left(\frac{\{\angle BDC\}_L}{\{\text{Square } ABDC\}_L} \right)}{\frac{\{\text{Point } B\}_L}{\{\text{bond } BA\}_L}} \quad (8.1.3-2)$$

5. The third square containing A will be F-A-C-H. You may find the bond A→C and F→A are both in the square F-A-C-H. In step one, we have put A-F with respect to F; in step two, Kikuchi gave a correction factor to correct between A and C, which is

$$\lambda = \frac{\left(\frac{\{\text{Point } C\}_L}{\{\text{bond } AC\}_L} \right)}{\left(\frac{\{L!\}}{\{\text{Point } A\}_L} \right)} \quad (8.1.3-3)$$

Therefore, with respect to the angle FHC, the correction factor is

$$\Gamma_2 = \frac{\left(\frac{\{\angle FHC\}_L}{\{\text{SquareACHF}\}_L} \right)}{\frac{\{\text{Point } F\}_L}{\{\text{bondAF}\}_L} \times \lambda} \quad (8.1.3-4)$$

Similarly, consider the squares containing A one by one, and find the correction factors one by one, we should have total 12 squares containing A and 11 correction factors. More squares are counted, more accurate the approximation will be.

Following the 1-D and 2-D Ising Models, the number of ways G_L to put a spin on A is

$$G_L = G_1 \prod_{i=1}^{11} \Gamma_i \quad (8.1.3-5)$$

8.2 Procedures to Construct the Substitutional Disordered Alloy

The main programs and procedures to construct the substitutional disordered alloy can be divided into four steps (Figure 8-7).

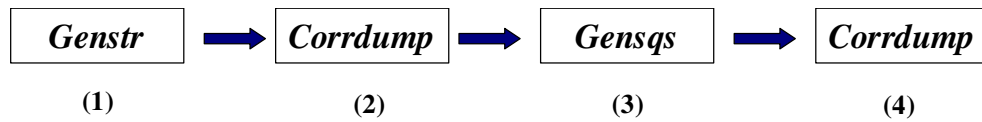


Figure 8-7. Procedures to construct the substitutional disordered alloy.

8.2.1 Genstr

First, an input file, named Lat.in, with the information of unit cell is passed into the code *Genstr*. In this thesis, 16-atom $\text{Fe}_{1-x}\text{Ni}_x$ ($x=12.5\%$) is desired. By this code, the atom Fe or Ni is periodically repeated along the lattice vectors and total 2^{16} structures are

generated. Each structure is called configuration here. The Ising-like model can be used to describe the configurations (Figure 8-9). The procedures and pseudocode of *genstr* are shown in Figure 8-10.

1	1	1	90	90	90		
0.5	0.5	0.5				}	Lattice vectors
0.5	-0.5	-0.5					
-0.5	0.5	-0.5					
0	0	0	Fe, Ni				Original atoms' positions

Figure 8-8. An input file named “Lat.in”.

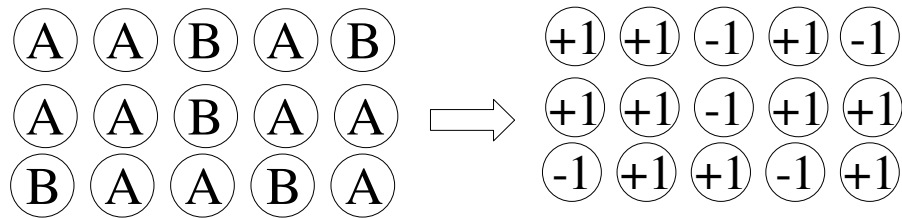


Figure 8-9. Ising-like model. A & B are atom species.

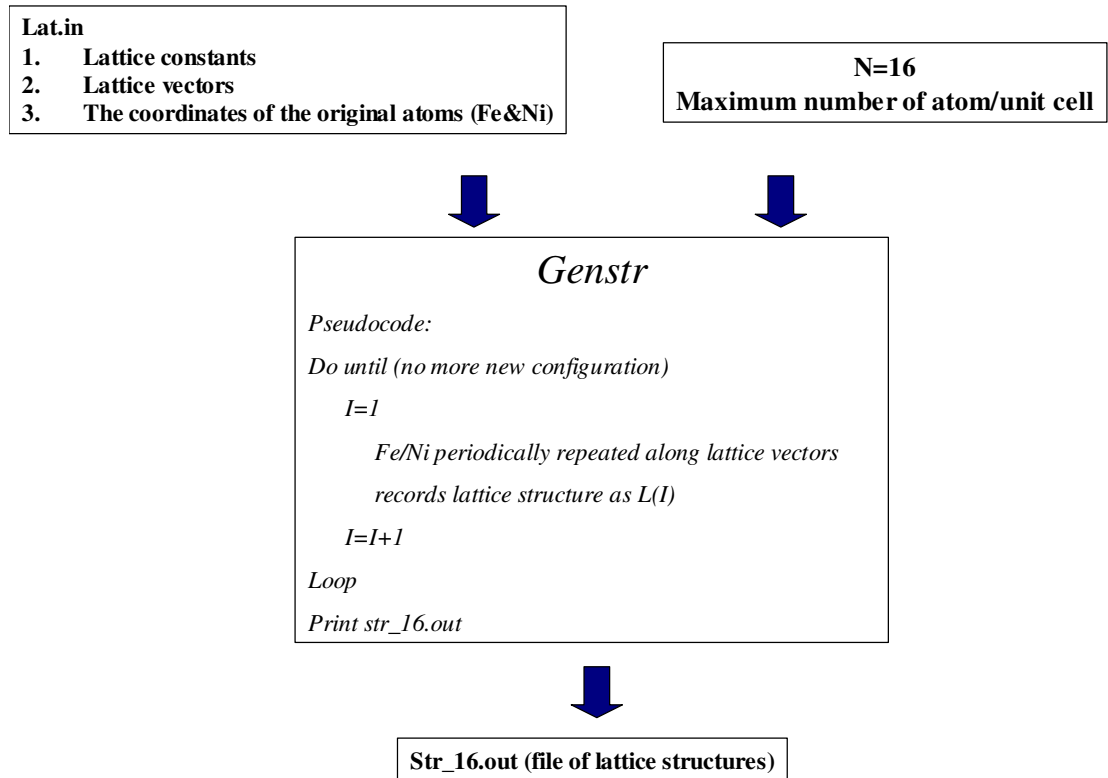


Figure 8-10. Procedures and pseudocode of genstr.

With all structures obtained, a structure A with desired concentration ($x=12.5\%$) is selected from the file str_16.out. The file str_A.out for structure A is shown in Figure 8-11. Two Nickel atoms are listed in the structure file, which means the desired concentration.

```

1.000000 0.000000 0.000000
0.000000 1.000000 0.000000
0.000000 0.000000 1.000000
-0.500000 2.500000 1.500000
-0.500000 -1.500000 -2.500000
-1.000000 -1.000000 1.000000
-1.500000 0.500000 0.500000 Ni
-1.000000 1.000000 1.000000 Ni
-1.000000 0.000000 1.000000 Fe
-1.000000 1.000000 -0.000000 Fe
-1.500000 0.500000 1.500000 Fe
-1.500000 -0.500000 -0.500000 Fe
-1.000000 -0.000000 -0.000000 Fe
-0.500000 0.500000 0.500000 Fe
-1.000000 -1.000000 0.000000 Fe
-1.500000 0.500000 -0.500000 Fe
-1.000000 -0.000000 -1.000000 Fe
-1.500000 -0.500000 0.500000 Fe
-1.000000 -1.000000 -1.000000 Fe
-0.500000 -0.500000 -0.500000 Fe
-2.000000 0.000000 0.000000 Fe
-1.500000 -1.500000 -0.500000 Fe

```

} Coordinate system
} Lattice vectors
} 2 Nickel atoms
(satisfy the desired concentration)
} 14 Iron atoms
(satisfy the desired concentration)

Figure 8-11. str_A.out to provide the atom information for structure A.

8.2.2 Corrdump

The step (2) in Figure 8-8 is to generate Clusters.out and Torr.out from *Corrdump* code. This code is to obtain the information of figures based on the structure A. That is to say, *corrdump* simply calculated the idea random correlation functions by $(1-2x)^k$, simultaneously gives the list of the cluster information of the structure A.

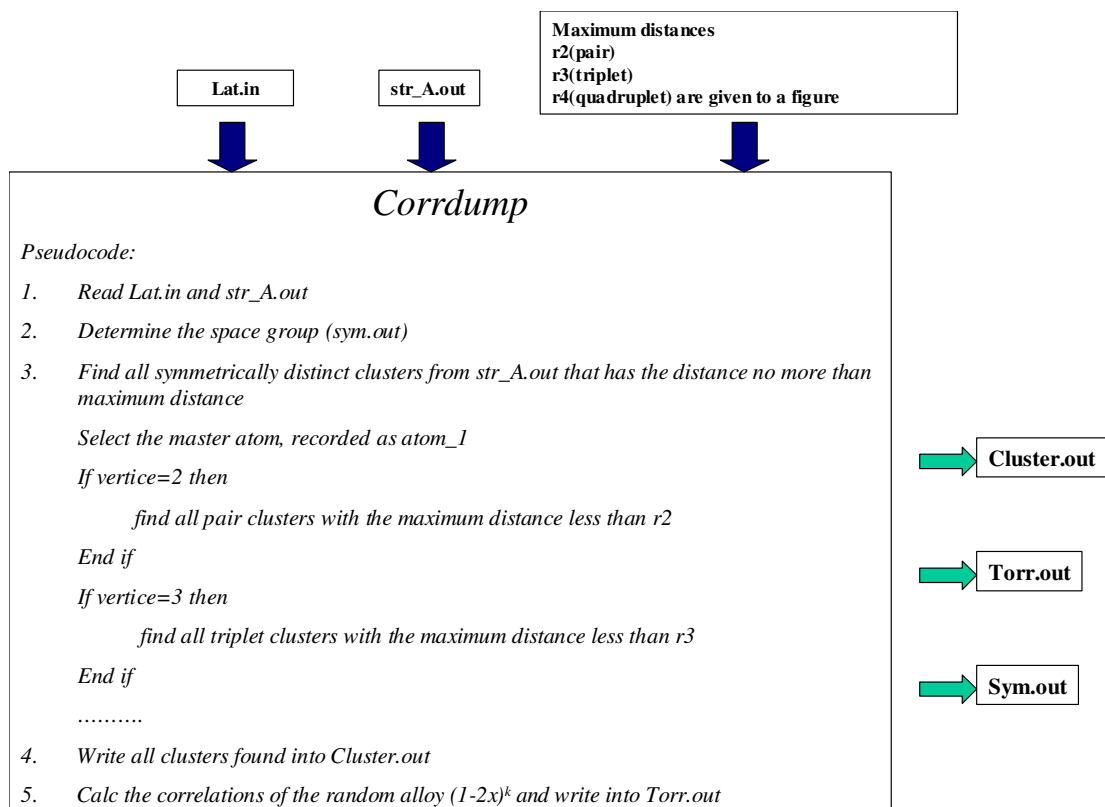


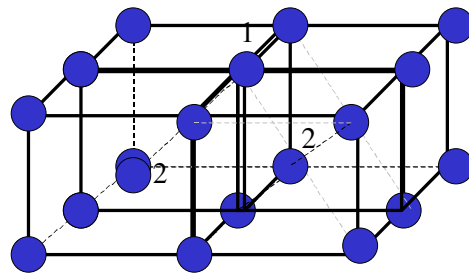
Figure 8-12. Procedures and Pseudocode of Corrdump.

$(2x-1)^1$	$(2x-1)^2$	$(2x-1)^2$	$(2x-1)^2$	$(2x-1)^2$	$(2x-1)^2$	$(2x-1)^2$
m=1	m=1	m=2	m=3	m=4	m=5	m=6
↓	↓	↓	↓	↓	↓	↓
-0.75000	0.56250	0.56250	0.56250	0.56250	0.56250	0.56250

Figure 8-13. The file Torr.out obtained from Corrdump.

Clusters.out is a very important file that has the desired cluster information. By restricting the maximum distance, some figures within the distance will be found and written into the file Clusters.out. If the distances are given at a large number, the alloy from the periodically repeated structures will better approximate the random alloy. The

procedures of finding clusters can be regarded as cases of searching for the neighbor. In Figure 8-14, if one stands at the atom position 1 looking for his first nearest neighbor, then the position of atom 2 will be desired. And this connection can be called figure-1. 1st vertex means the position 1 and 2nd vertex means the position 2. The distance between them is the ratio 0.866 of the lattice constant. It is easy to find such figure is not unique. Actually there are more figures that exactly repeat the figure-1. The number of the same figures is recorded as the integer 4 to the 16-atom supercell.



```

1
0.00000
1
0.50000 0.50000 -0.50000 0 0

4 ..... Numbers of the same figures
0.86603 ..... Distance between 2 atoms
2 ..... Vertex number
0.50000 0.50000 -0.50000 0 0
1.00000 1.00000 -1.00000 0 0
3
1.00000
2
0.50000 0.50000 -0.50000 0 0
-0.50000 0.50000 -0.50000 0 0

```

1st vertex

2nd vertex

Figure 8-14. The file Clusters.out from Corrdump.

8.2.3 Gensqs

Aimed at the correlations in Torr.out, The step (3) *Gensqs* code in Figure 8-8 is to obtain all structures with desired concentration and matching the Clusters.out.

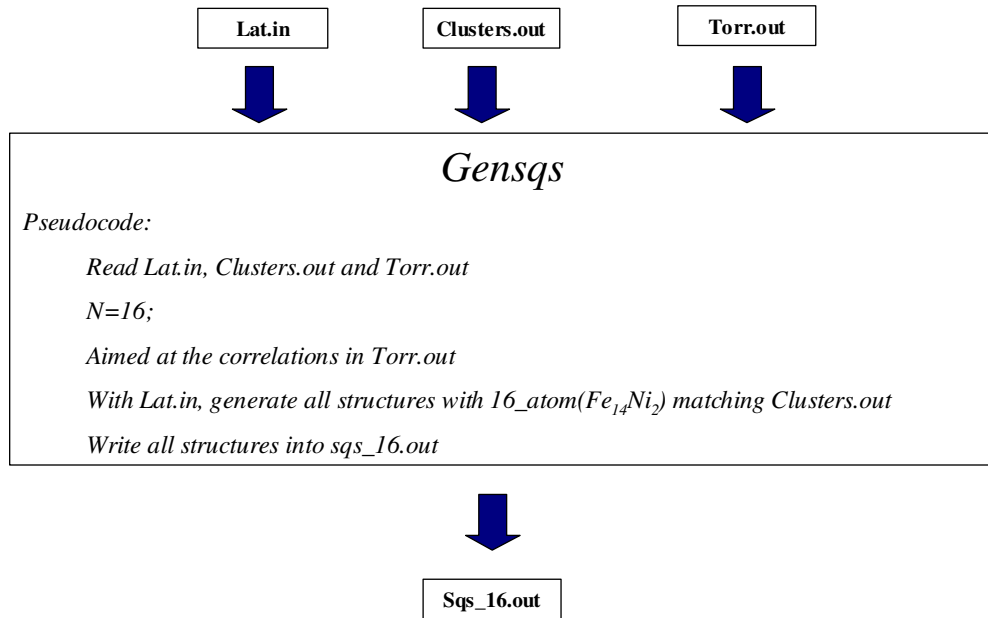


Figure 8-15. Special quasirandom structure is generated by Gensqs.

After the step (3), a set of structures with the desired concentration and clusters are obtained. *Corrdump* is applied to calculate the correlation functions to these structures.

-0.75000	0.56250	0.50000	0.50000	0.56250	0.75000	0.66667
-0.75000	0.50000	0.58333	0.58333	0.50000	0.75000	0.66667
-0.75000	0.50000	0.50000	0.54167	0.54167	0.75000	0.66667
-0.75000	0.50000	0.50000	0.50000	0.54167	0.87500	0.83333
-0.75000	0.50000	0.58333	0.58333	0.50000	0.75000	0.66667
-0.75000	0.56250	0.50000	0.50000	0.56250	0.75000	0.66667
-0.75000	0.50000	0.50000	0.54167	0.50000	0.87500	0.83333
-0.75000	0.50000	0.50000	0.50000	0.58333	0.75000	0.66667
-0.75000	0.56250	0.50000	0.50000	0.56250	0.75000	0.66667
-0.75000	0.50000	0.58333	0.58333	0.50000	0.75000	0.66667
-0.75000	0.50000	0.58333	0.50000	0.58333	0.50000	0.66667
-0.75000	0.56250	0.58333	0.50000	0.56250	0.50000	0.66667
-0.75000	0.50000	0.50000	0.54167	0.58333	0.62500	0.66667
-0.75000	0.56250	0.50000	0.54167	0.56250	0.50000	0.75000
-0.75000	0.50000	0.50000	0.58333	0.58333	0.50000	0.66667
-0.75000	0.56250	0.50000	0.58333	0.56250	0.50000	0.66667
-0.75000	0.56250	0.50000	0.50000	0.56250	0.62500	0.75000
-0.75000	0.50000	0.58333	0.50000	0.58333	0.50000	0.66667
-0.75000	0.56250	0.50000	0.50000	0.56250	0.62500	0.83333
-0.75000	0.56250	0.58333	0.50000	0.56250	0.50000	0.66667
-0.75000	0.56250	0.50000	0.54167	0.56250	0.50000	0.66667
-0.75000	0.50000	0.50000	0.58333	0.58333	0.50000	0.66667
-0.75000	0.56250	0.50000	0.58333	0.56250	0.50000	0.66667
-0.75000	0.56250	0.50000	0.50000	0.56250	0.50000	0.83333
-0.75000	0.50000	0.58333	0.50000	0.50000	0.75000	0.83333
-0.75000	0.50000	0.50000	0.66667	0.50000	0.50000	0.83333
-0.75000	0.50000	0.58333	0.58333	0.50000	0.50000	0.83333

⋮

Figure 8-16. All correlation functions from *Corrdump* on these structures with the desired figure of *Clusters.out*

This procedure compares these correlation functions with the *Torr.out* and find the minimum error from $\sum_{k,m} [(2x-1)^k - \bar{\Pi}_{k,m}(S)]$. The details about the correlation functions can be found in Chapter 2. Each row in Figure 8-16 represents the correlation functions of one structure.

Then, the best structure with the minimum error is obtained, which is plotted in Figure 8-17.

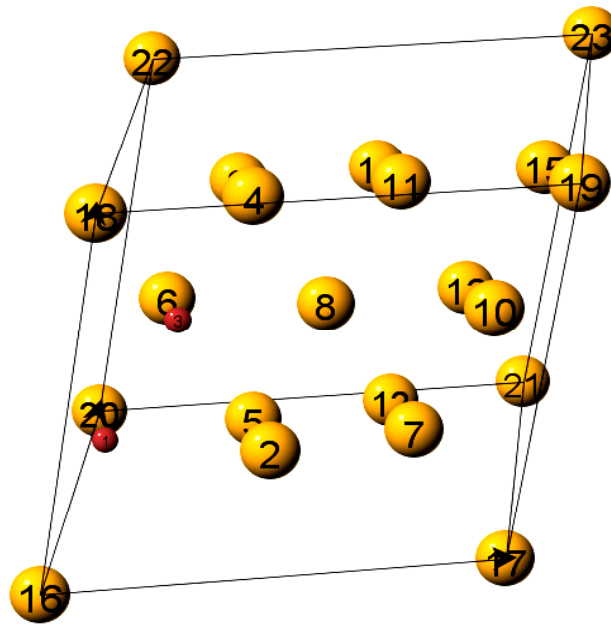


Figure 8-17. Substitutional Disordered Binary Alloy $\text{Fe}_{1-x}\text{Ni}_x$ ($x=12.5\%$).

8.3 Procedures For Cold Curve Calculation By Using VASP



Figure 8-18. Input files and output files for VASP calculations.

The input files which are needed for VASP calculations include four files: INCAR, POSCAR, POTCAR and KPOINTS.

8.3.1 For Iron calculations

For example, the INCAR and POSCAR files for FCC AFM Iron is shown:

INCAR:

```
SYSTEM =fcc AFM Fe mag-relax
ISTART =1;
ISM EAR=0; SIGMA=0.2
IBRION = 2; ISIF =3; NSW =20
EDIFF = 1E-04; EDIFFG = 1E-03
ISPIN=2
LORBIT=11
MAGMOM=8 8 -8 8
```

POSCAR:

```
For VASP. System= AFM100
1.0000000000000000
 3.4506824159598484 0.0000000000000000 0.0000000000000000
 0.0000000000000000 3.4508356266993685 0.0000000000000000
 0.0000000000000000 0.0000000000000000 3.4506824159598484
4
Direct
0.0000000000000000 0.0000000000000000 0.0000000000000000
0.0000000000000000 0.5000000000000000 0.5000000000000000
0.5000000000000000 0.0000000000000000 0.5000000000000000
0.5000000000000000 0.5000000000000000 0.0000000000000000
```

KPOINTS:

```
K-Points
0
Monkhorst Pack
6 6 6
0 0 0
```

8.3.2 For Fe₁₄Ni₂ calculations

For example, the INCAR and POSCAR files for BCC FM Fe₁₄Ni₂ SQS structure is shown:

INCAR:

```
SYSTEM =bcc FeNi mag-relax
ISTART =0;
ISM EAR=0; SIGMA=0.2
IBRION = 2; ISIF =2; NSW =1
EDIFF = 1E-04; EDIFFG = 1E-03
```

```
ISPIN=2
LORBIT=11
MAGMOM=8 8 8 8 8 8 8 8 8 8 8 8 8 8 8
```

POSCAR:

```
For VASP. System=      FeNiBcc
1.000000000
  4.0962628298562000    1.3701329641343900    -1.3629079135893700
  4.0927656744316100    -1.3610282535605700    4.0873130628400400
  2.7257012899368000    -5.4699703511152400    -2.7306686844660800
2 14
Direct
0.4446733481404150    0.1830148647092711    0.0596441105927825
0.3053266518595850    0.5669851352907289    0.1903558894072175
0.0178157424429061    0.9932261026626955    0.0018794587453868
0.0602713194111316    0.3114949407843430    0.4364549131325774
0.1768621651277385    0.9417129104445530    0.3188738555883314
0.6213609527194961    0.1296249873927634    0.3767252608630021
0.8750000000000000    0.3750000000000000    0.1250000000000000
0.2478312093361097    0.2501817011311108    0.7463457274365012
0.5021687906638904    0.4998182988688892    0.5036542725634988
0.7321842575570938    0.7567738973373045    0.2481205412546132
0.1286390472805039    0.6203750126072366    0.8732747391369979
0.3750000000000000    0.8750000000000000    0.6250000000000000
0.8104479557153212    0.0623250238162503    0.6923655371269909
0.6897286805888684    0.4385050592156570    0.8135450868674226
0.9395520442846788    0.6876749761837497    0.5576344628730091
0.5731378348722614    0.8082870895554470    0.9311261444116615
```

KPOINTS:

```
K-Points
0
Monkhorst Pack
6 6 6
0 0 0
```

8.3.3 For Fe₁₄Ni₂C₁ calculations

For example, the INCAR and POSCAR files for BCC NM Fe₁₄Ni₂C₁ lattice structure is shown:

INCAR:

```
SYSTEM =bcc FeNiC mag-relax
```

```
ISTART =0;
ISMEAR=0; SIGMA=0.2
IBRION = 2; ISIF =2; NSW =1
EDIFF = 1E-07; EDIFFG = 1E-06
```

POSCAR:

```
For VASP. System=      FeNiCBcc
2.8600000000000000
  1.3061788182753908      0.6064918098459504      -0.4369037712374954
  1.3072049205381804      -0.6042131796454265      1.3143474505997792
  0.8681815428978472      -2.4154647265556166      -0.8724063761352031
  2  14  1
Direct
0.4362078546930496  0.1868241660710614  0.0614783190554432
0.3158594831761549  0.5602410236718622  0.1852642674714486
0.0376842597254999  0.3167641653897234  0.4243244921927227
0.1913465262511413  0.9289025345462352  0.3146195756321288
0.6516567007474359  0.1098102848255570  0.3631293122806497
0.8758972891241250  0.3726973333235132  0.1196792388124447
0.2253854206813411  0.2594397064740794  0.7613012709757756
0.5113961147422029  0.5213315509476766  0.4971231236467904
0.7613815866812755  0.7414816515134015  0.2524717793549489
0.1046659328484867  0.6318705657973015  0.8693323928585790
0.3678421401478618  0.8547993532256304  0.6310242007669766
0.8350533129541740  0.0563220553740050  0.7014327729993317
0.6896532485460439  0.4502151375840711  0.8143597949846531
0.9390964623816149  0.6885558729597668  0.5628107857458042
0.5627349255539468  0.8132312494846943  0.9407227041850897
0.0051190769350558  0.0061172171000767  0.0026136937595272
0.4367578186807010  0.1888961317113442  0.5608122752776855
```

KPOINTS:

```
K-Points
0
Monkhorst Pack
6 6 6
1 0 0
```

8.4 Procedures For Lattice Thermal Calculation By Using PHONON

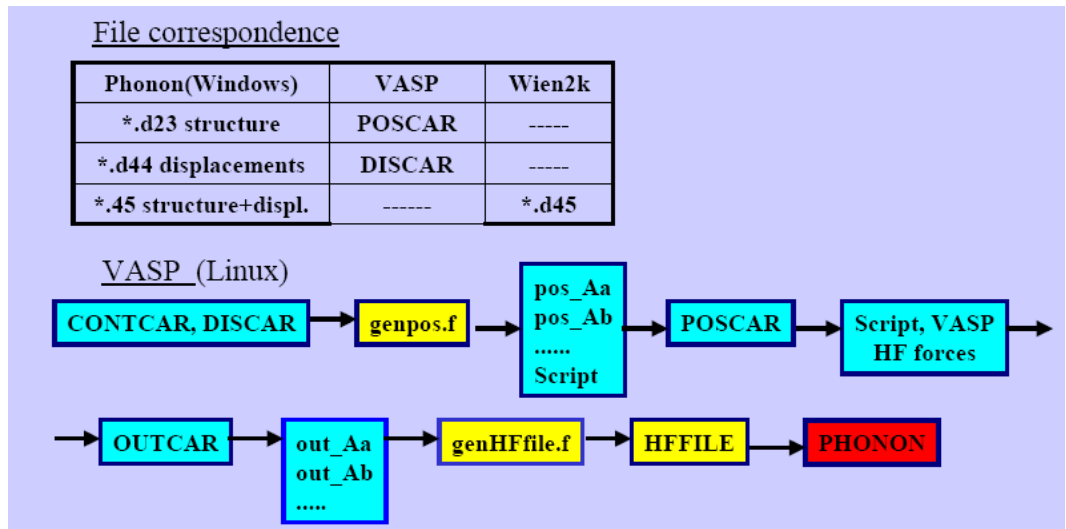


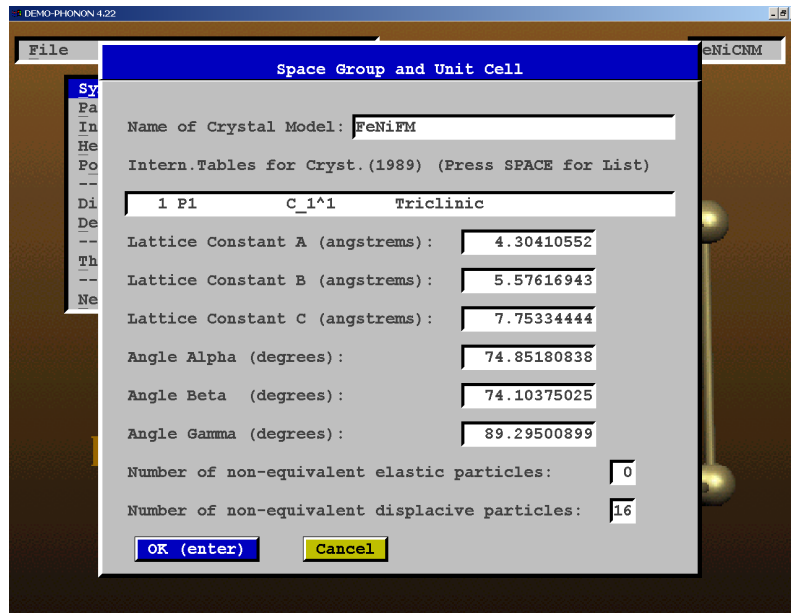
Figure 8-19. Procedure for PHONON calculation and interaction with VASP [Parlinski-2004].

The procedure for PHONON calculation and the interaction with VASP is shown above. Based on CONTCAR and DISCAR, generated from PHONON software, using genpos, we can obtain a series of POSCAR which include the information of displaced atoms. By using VASP, one can obtain OUTCAR files which contain HF force for each POSCAR. Then from all the relevant OUTCAR files, i.e. out_Aa, out_Ab, etc., using genHFfile, one can obtain HFFILE which includes HF forces. This HFFILE and all the lattice information as shown in the following steps are used in PHONON.

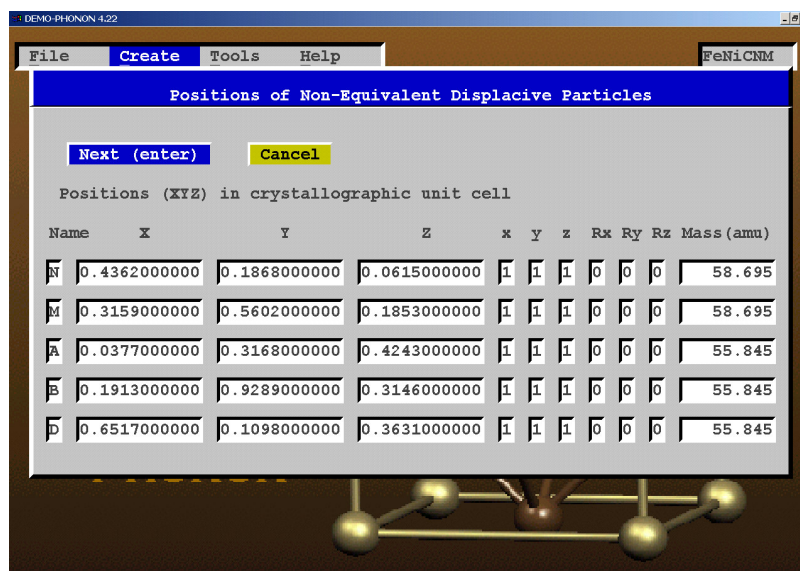
8.4.1 Steps for the PHONON calculations

We use $\text{Fe}_{14}\text{Ni}_2$ as an example.

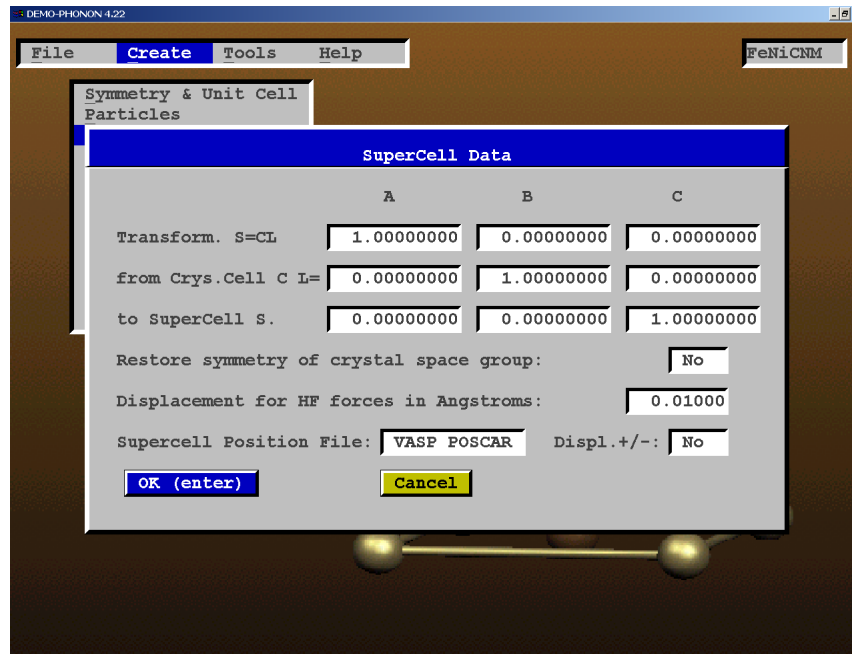
Step1: input for lattice information



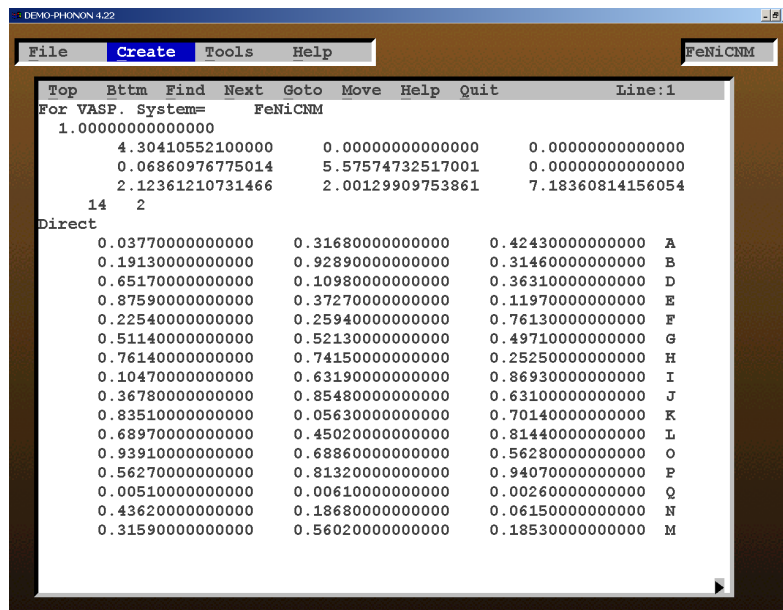
Step2: input for atom positions



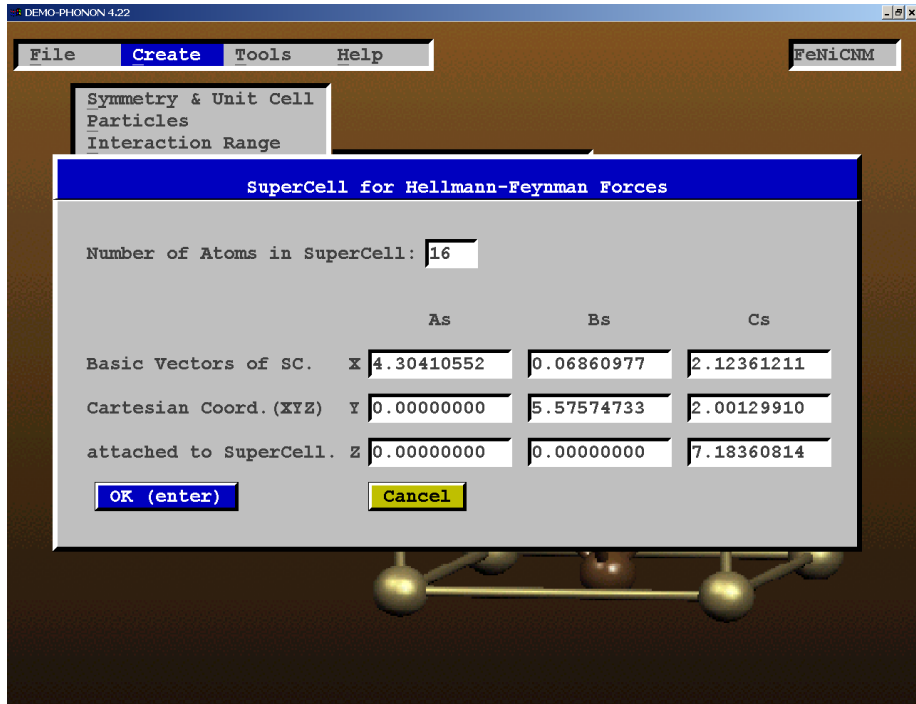
Step3: input for the supercell and the magnitude of displacement for perturbed atoms.



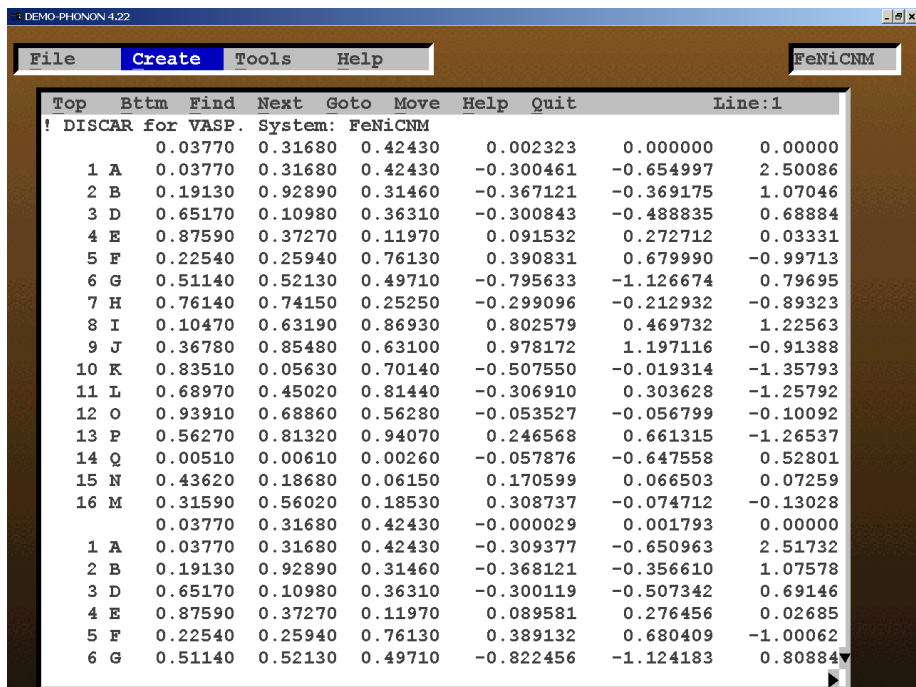
The generated POSCAR is listed:



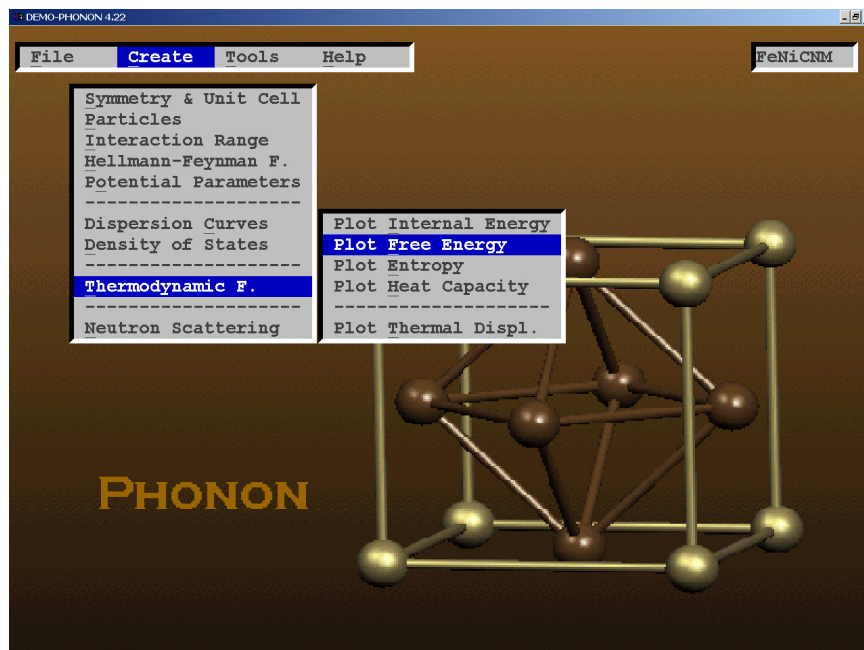
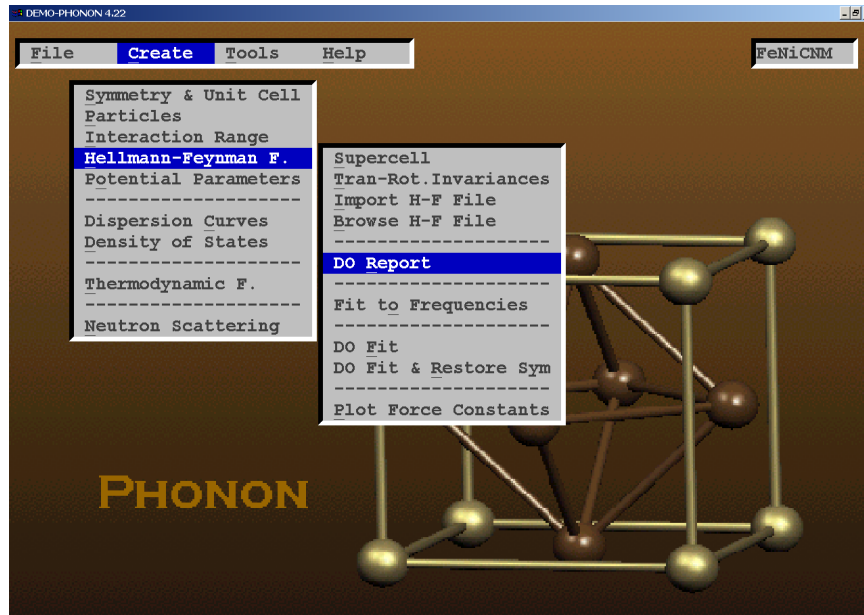
Step4: input for the supercell lattice vectors for HF forces



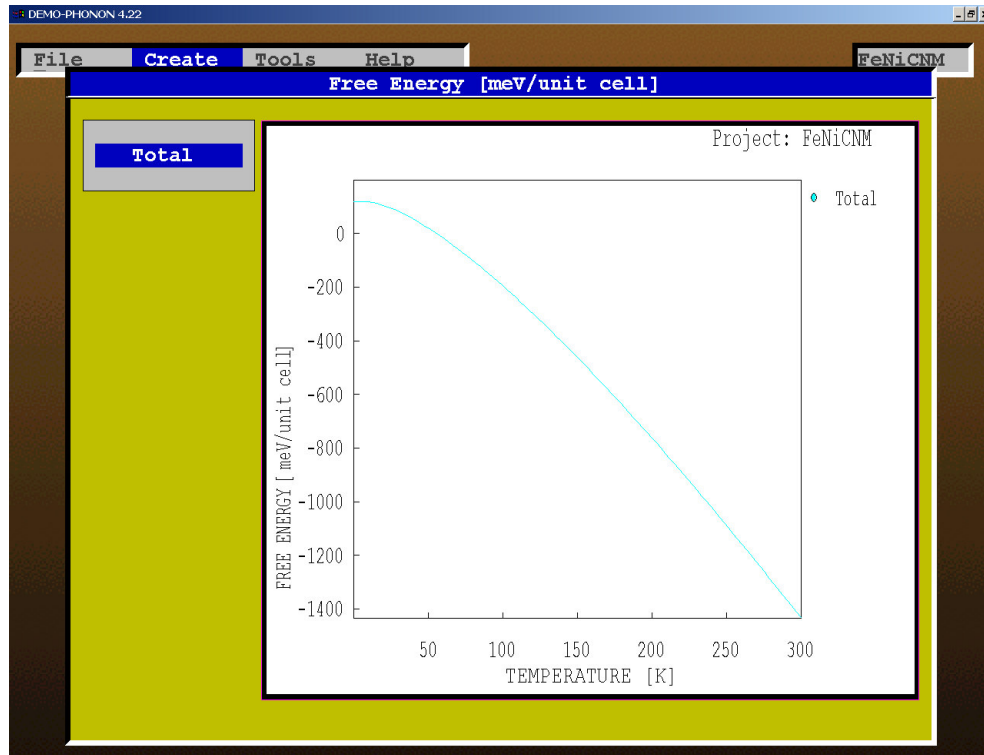
The imported HFFILE is



Step5: steps for phonon calculation



Step6: Calculate the free energy



REFERENCES

- A. C. Whiffin. The use of flat-ended projectiles for determining dynamic yield stress – II. Tests on various metallic materials. Proceedings of the Royal Society of London, Series A (Mathematical and Physical Sciences), v 194, n 1038, 1948, p 300-322.
- A. J. Freeman, J. H. Xu, T. Hong & W. Lin. In Ordered Intermetallics Physical Metallurgy and mechanical Behavior, Edited by C. T. Liu (Kluwer Academic, Dordrecht, 1992), pp.1-14.
- A. Mookerjee and R. Prasad. Generalized Augmented Space Theorem and Cluster Coherent Potential Approximation. Phys. Rev. B V48 P17724 1993.
- A. N. Larsen, A. B. Hansen, D. Reitze, J. J. Goubel, J. Fagepedersen & A. Mesli, Phys. Rev. B V64 P233202 2001.
- A. P. Jephcoat, H. K. Mao & P. M. Bell, J. Geophys. Res. V91 P4677 1986.
- A. Silverman, A. Zunger, R. Kalish & J. Adler. Atomic-scale structure of disordered $\text{Ga}_{1-x}\text{In}_x\text{P}$ alloys. Phys. Rev. B. V51 P10462 1995.
- A. Tate, A possible explanation for the hydrodynamic transition in high speed impact. Int. J. Mech. Science, V19, 121(1976).
- A. Tate, A theory for the deceleration of long rods after impact. J. Mech. Phys. Solids, V15, 287(1967).
- A. Tate, Long A simple estimate of the minimum target obliquity required for the ricochet of a high speed long rod projectile. J. Phys. D: Appl. Phys., V12,(1979).
- A. Tate, Long rod penetration models – Part I. A flow field model for high speed long rod penetration. Int. J. Mech. Sci., V28, No.8, pp535-548(1986).
- A. Tate, Long rod penetration models – Part II. Extensions to the hydrodynamic theory of penetration. Int. J. Mech. Sci., V28, No.9, pp599-612(1986).
- A. Van De Walle & G. Ceder. The effect of lattice vibrations on substitutional alloy thermodynamics. Rev. of Mod. Phy. V74, P11, 2002.
- A. Van de Walle and M. Asta. First principles modeling of phase equilibria. In S. Yip, Editor, Handbook of Materials Modeling, Volume I. Kluwer Academic Publishers, 2005.

- A. Van De Walle, M.Asta & G.Ceder. The Alloy Theoretic Automated Toolkit: A user Guide.
- A. Van de Walle, M.Asta, & G.Ceder. CALPHAD: Comput. Coupling Phase Diagrams Thermochem. V26 P539 2003.
- A. Zunger, S.H.Wei, L.G.Ferreira & J.E.Bernard. Special quasirandom structures. *Phy. Rev. Lett.* V65 P353 1990.
- Acet, M., Zahres, H., Wassermann, E.F., & Pepperhoff W. *Phy. Rev. B* V49 P6012 1994.
- Atman APF, and Claudin P. Numerical stress response functions of static granular layers. *Conds matt 1* (2003).
- B. Barbiellini, E.G.Moroni & T.Jarlborg. *J.Phys. Condens. Matter.* V2 P7597 1990.
- B. K. Godwal & R.Jeanloz. *Phys. Rev. B* V40 P7501 1989.
- B. K.Godwal, S.K.Sikka & R.Chidambaram. *Phys. Rev. B* V20 P2362 1979.
- B. K.Vainshtein. *Modern Crystallography I*, Springer-Verlag, 1981.
- B.L. Gyorffy, *Phys. Rev. B*, V5 P2382 1972.
- Bishop, R. F., Hill, R., and Mott, N. F., "The theory of indentation and hardness tests," *Proceedings, Physical Society of London*, v. 57, 1945, pp. 147 –159.
- Biswajit Banerjee. The mechanical threshold stress model for various temperatures of AISI4340 steel. Preprint submitted to Elsevier Science. Aug 2005.
- Bloch, P.E., *Phys. Rev. B*, 1994, 50(24), 17953-17979.
- Bylaska, E.J., Rustad, J.R., and Dupuis, m. *Environmental Dynamics and Simulation 1999 Annual Report*.
- C. Abrahams, L.Guttman & J.S.Kasper. *Phy. Rev.* V127 P2052 1962.
- C. Wolverton & A. Zunger. Ising-like description of structurally relaxed ordered and disordered alloys. *Phy Rev Lett.* V75 P3162 1995.
- C. Amador, W.R.L.Lambrecht & B.Segall. *Phys. Rev. B.* V46 P1870 1992.
- C. Colinet & A.Pasturel, *J.Alloys Compd.* V296 P6 2000.
- C. Domain, C.S.Becquart & J. Foct. Ab initio study of foreign interstitial atom (C,N) interactions with intrinsic point in α -Fe. *Phy. Rev. B* V69, P144112, 2004.
- C. Kittel, *Introduction to Solid State Physics*, 5th ed. (Wiley, New York, 1976).

- C. S.Wang, B.M.Klein & H.Krakauer. Theory of Magnetic and Structural Ordering in Iron. *Phy. Rev. Lett.* V54 N16 P1852 1985.
- Chang Gil Lee, Woo Jin Park, Sunghak Lee & Kwang Seon Shin. Microstructure development of adiabatic shear bands formed by ballistic impact in a WELDALITE 049 Alloy. V29A P477 1987.
- Chao Jiang, C.Wolverton, Jorge Sofo, Long-Qing Chen, & Zi-Kui Liu. First-principles study of binary bcc alloys using special quasirandom structures. *Phy Rev B*, V69, P214202, 2004.
- Chao Jiang. Theoretical studies of Aluminum and Aluminide alloys using CALPHAD and First principles approach. Ph.D. Thesis. 2004.
- Charles E. Anderson, Jr, Dennis L.Orphal, Roland R.Franzen, and J.D.Walker. On the hydrodynamic approximation for long-rod penetration. *Int. J. Impact Engng.* Vol.22, pp23-43, 1999.
- Charles E. Anderson, Jr, J.D.Walker, Stephan J.Bless, and T.R.Sharron. On the velocity dependence of the L/D effect for long-rod penetrators. *Int. J. Impact Engng.* Vol.17, pp13-24, 1995.
- Charles E. Anderson, Jr, J.D.Walker, Stephan J.Bless, and Yehuda Partom. On the L/D effect for long-rod penetrators. *Int. J. Impact Engng.* Vol.18, pp247-264, 1996.
- Charles E. Anderson, Jr, J.D.Walker. An examination of long-rod penetration. *Int. J. Impact Engng.* Vol.11, No.4, pp481-501, 1991.
- Charles E. Anderson, Jr, Volker Hohler, J.D.Walker and Alois J. Stilp. Time-resolved penetration of long rods into steel targets. *Int. J. Impact Engng.* Vol.16, No.1, pp1-18, 1995.
- Charles E. Anderson, Jr, Volker Hohler, J.D.Walker, Alois J.Stilp. The influence of projectile hardness on ballistic performance. *Int. J. Impact Engng.* Vol.22, pp619-632, 1999.
- Cort, G., Taylor, R.D. & Willis, J.O. *J. Appl. Phys.* V53 P2064 1982.
- D. B. Laks, S.Wei & A.Zunger. Evolution of alloy properties with long-range order. *Phy. Rev. Lett.* V69 P3766 1992.
- D. B.Laks, L.G.Ferreira, S. Froyen & A. Zunger. Efficient cluster expansion for substitutional systems. *Phy. Rev. B* V46, P12587 1992.
- D. C. Pack and W.M.Evans, *Proc. Phys. Soc., Lond.* B64, 298-302 (1951).
- D. C.Swift, G.J. Ackland, A.Hauer & G.A.Kyrala. *Phy. Rev. B* V64 P214107 N1 2001.

- D. D.Koelling & G.O.Arbman. J. Phys. F V5 P2041 1975.
- D. E.Jiang & Emily A. Carter. Carbon dissolution and diffusion in ferrite and austenite from first principle. Phy. Rev. B V67, P214103, 2003.
- D. J.Singh, W.E.Pickett & H.Krakauer. Phys. Rev. B V43 P11628 1991.
- D. M.Clatterbuck, D.C.Chrzan & J.W.Morris, Jr. The inherent tensile strength of iron. Philosophical magazine letters. V82 N3 P141 2002.
- D. R. Christman and J.W. Gehring, J.appl.Phys.37, 1579-1587 (1966).
- D. R.Hamann. Phys. Rev. Lett. V42 P662 1979.
- Dominik Marx and Jurg Hutter, Ab Initio molecular Dynamics: Theory and implementation. Modern methods and Algorithms of Quantum Chemistry, Proceedings, Second Edition, J.Grotendorst (Ed.), John Von Neumann Institute for Computing, Julich, NIC Series, Vol. 3, ISBN 3-00-005834-6, pp329-477, 2000.
- E. I.Kondorskii & V.L.Sedov, Ah.Eksp. Thor. Fiz. V35 P1579 1959.
- E. V.Monakhov, A.N.Larsen, and P.Kringhoj, J.Appl. Phys. V81 P1180 1997.
- E. Wimmer, H.Krakauer, M.Weinert & A.J.Freeman. Phys. Rev. B V24 P864 1981.
- F. Jing, Introduction to Experimental Equation of State. Ed. 2, (Science Press, Beijing, 1999), P.197. (in Chinese).
- F. Zhang, Y.A.Change, Y.Du, S.L.Chen & W.A.Oates, Acta Mater. V51 P207 2003.
- Field, Bash and karplus, j. Comp. Chem.
- Forrestal, M. J., Frew, D. J., Honchak, S. J., and Brar, N. S., "Penetration of ground and concrete targets with ogive-nose steel projectiles", Int. J. Impact Eng., 18, 5, pp. 465-476, 1996.
- Fracture toughness of high-strength steels at low temperatures. <http://www.key-to-steel.com/articles/art66.htm>.
- Frew, D.J., Hanchak, S.J., Green, M.L., and Forrestal, M.J., "Penetration of Concrete Targets with Ogive-Nose Steel Rods", International Journal of Impact Engineering, Vol. 21, No. 6, 1998, pp. 489-497.
- G. D.Garbulsky & G.Ceder. Phys. Rev. B V49 P6327 1994.
- G. Johanson, M.B.McGirr, & D.A.Wheeler. Phys. Rev. B V1 P3208 1970.
- G. Simmons & H.Wang, In Single Crystal Elastic Constants and Aggregate Properties (MIT Press, Cambridge, 1971).

- Geoffrey Taylor, The use of flat-ended projectiles for determining dynamic yield stress – I. Theoretical consideration, Proceedings of the Royal Society of London, Series A, Mathematical and Physical Sciences, V194, No. 1038 (Sep. 2, 1948), 289-299.
- Georg Kresse and Jurgen Furthmuller. Vienna Ab-initio Simulation Package. Wien, Austria 2005.
- Gerd Steinle-Neumann, Lars Stixrude & Ronald E.Cohen. Magnetism in dense hexagonal iron. PNAS, V101 N1 P33 2004.
- Gerd Steinle-Neumann, L. Stixrude, & R.E. Cohen. Phys. Rev. B. V60 P791 1999.
- Gong, Z, Dai F, Fei Y, Zhang L, and Jing F. “Equation of state, phase stability of $(\text{Mg}_{0.92}, \text{Fe}_{0.08})\text{SiO}_3$ perovskite from shock wave study and its geophysical implications.” Proc. Of APS on Shock Compression of Condensed Matter. Portland, Oregon, July 20 -25, 2003.
- Goodier, J.N., On the mechanics of indentation and cratering in solid targets of strain-hardening metal by impact of hard and soft spheres. TR002-64, July 1964, Poulter Laboratories, Stanford Research Institute, Menlo Park, CA
- H. Haas. S.Cottenier. Magnetization Changes induced by 4d/5sp impurities in iron. J. Magnetism. & Magnetic Mater. V226-230, P1035-1037, 2001.
- H. Haas. S.Cottenier. Magnetization Changes induced by 4d/5sp impurities in iron. J. Magnetism. & Magnetic Mater. V226-230, P1035-1037, 2001.
- H. Hasegawa & D.G.Pettifor. Microscopic Theory of the Temperature-Pressure Phase Diagram of Iron. Phy. Rev. Lett. V50 N2 P130 1983.
- H. J.F.Jansen, K.B.Hathaway & A. J.Freeman. Structural properties of ferromagnetic bcc iron: A failure of the local-spin-density approximation. Phy. Rev. B. V30 N10 P6177 1984.
- H. K.Mao. Y.Wu, L.C.Chen, J.F.Shu & A.P.Jephcoat. *et al.*, J.Geophys. Res. V95 N21 P737 1990.
- H. Y.Geng, M.H.F.Sluiser & N.X.Chen. Order-disorder effects on the equation of state for fcc Ni-Al alloys. Phy Rev B. V72 P014204 2005.
- H.Y.Geng, N.X.Chen & M.H.F.Sluiser. Shock-induced order-disorder transformation in Ni_3Al . Phy. Rev. B V71 P012105 2005.
- H.Y.Geng, N.X.Chen, & M.H.F.Sluiser, First-principles equation of state and phase stability for the Ni-Al system under high pressures. Phy. Rev. B V70, P094203, 2004.
- Hanagud, S., and Ross, B., Large deformation, deep penetration theory for a compressible strain-hardening target material. AIAA J., v. 9, n. 5, 1971, pp. 905-911.

- Hanagud, S., Finite amplitude spherical waves in a locking-relaxing solids. Invited Research Lecture, Proceedings, 5th U. S. National Congress of Applied Mechanics, America Society of Mechanical Engineers, 1966, pp. 63 – 77.
- Hemley, R.J. & Mao, H.K. *Int. Geol. Rev.* V43, P1 2001.
- Hirshfeld D, Radzyner Y and Rapaport DC. Molecular dynamics studies of granular flow through an aperture. *Phys Rev E* 56 (4), 1997, 4404.
- Hoover et al. *Cout. Phys.*, 1992, 6.
- Hopkins, H.G., Dynamic expansion of spherical cavities in metals. *Progress in Solid Mech.* Vol.1, edited by Hill, R. and Sneddon, I.N., Pergamon Press, Oxford, England, 1960, pp.84-164
- Hurd, C.M. Varieties of Magnetic order in Solids. *Contemp. Phys.* V23 P469 1982.
- Hutter, lecture notes. Introduction to ab initio molecular dynamics. 2002.
- J. C.Boettger & S.B.Trickey. *Phys. Rev. B* V53 P3007 1996.
- J. C.Mikkelsen & J.B.Boyce, *Phys. Rev. Lett.*, V49, P1412 1982.
- J. D.Walker and C.E. Anderson Jr, A Time-Dependent Model For Long-Rod Penetration. *Int. J. Impact Engng*, Vol.16, No.1, pp. 19-48, 1995.
- J. D.Walker, Charles E. Anderson, Jr. The influence of initial nose shape in eroding penetration. *Int. J. Impact Engng*. Vol.15, No.2, pp139-148, 1994.
- J. D.Walker, Donald J.Grosch, and Scott A.Mullin. Experimental impacts above 10km/s. *Int. J. Impact Engng*. Vol.17, pp903-914, 1995.
- J. D.Walker. A Hypervelocity penetration modeling: Momentum vs. energy and energy transfer mechanisms. *Int. J. Impact Engng*. Vol.26, pp809-822, 2001.
- J. D.Walker. A model for penetration by very low aspect ratio projectiles. *Int. J. Impact Engng*. Vol.23, pp957-966, 1999.
- J. D.Walker. Analytically modeling hypervelocity penetration of thick ceramic targets. *Int. J. Impact Engng*. Vol.29, pp747-755, 2003.
- J. D.Walker. New directions and new challenges in analytical modeling of penetration mechanics. CP620, Shock Compression of Condensed Matter – 2001.
- J. Haglund. *Phys. Rev. B*. V47 P566 1993.
- J. J.Rehr & R.Alben, *ibid.* V16 P2400 1977.

- J. P. Perdew, J. A. Chevary, S. H. Vosko, K. A. Jackson, M. R. Pederson & D. J. Singh. Phys. Rev. B V46 P6671 1992.
- J. W. D. Connolly & A. R. Williams. Phys. Rev. B. V27 P5169 1983.
- J. W. Otto, J. K. Vassiliou & G. Frommeyer. J. Mater. Res. V12(11) P3106 1997.
- J. Wright, Philos. Mag. V24 P217 1971
- J. Xie, S. P. Chen, H. V. Brand & R. L. Rabies. J. Phys: Condens. Matter V12 P8953 2000.
- James. H. Rose, John R. Smith, Francisco Guinea & John Ferrante. Phys. Rev. B V29 N6 P2963 1984.
- Jerome D., et al, "Proceedings of the Workshop on Thermomechanics of Impact and Penetration", 2000.
- Johnson, D. D., D. M. C. Nicholson, F. J. Pinski, and G. M. Stocks. Density Functional Theory for Random Alloys: Total Energy Within the Coherent Potential Approximation. Phys. Rev. Lett. V61 P3712 1987.
- Jonathan C. Boettger & Duane C. Wallace. Metastability and dynamics of the shock-induced phase transition in iron. Phys. Rev. B V55 N5 P 2840 1997.
- K. B. Hathaway, H. J. F. Jansen & A. J. Freeman. Phys. Rev. B V31 N12 P7603 1985.
- K. Binder, J. L. Lebowitz, m. K. Phani, & M. H. Kalos. Acta. Metall. V29 P1655 1981.
- K. Binder, Phys. Rev. Lett. V45 P811 1980.
- Kohloff et al. Phil. Mag. A, 1991, 64.
- Kubler. Phys. Lett. V81A P81 1981.
- L. C. Davis & H. Holloway. Solid State Commun. V64 P121 1987.
- L. C. Davis. Phys. Rev. B V28 P6961 1983.
- L. E. Ramos, J. Furthmuller, J. R. Leite, L. M. R. Scolfaro, & F. Bechstedt. Group-IV and group-V substitutional impurities in cubic group-III nitrides. Phys. Rev. B V68, P085209, 2003.
- M. Schroter, H. Ebert, H. Akai, P. Entel, E. Hoffmann & G. G. Reddy. First-principles investigations of atomic disorder effects on magnetic and structural instabilities in transition-metal alloys. Phys. Rev. B V52 N1 P188 1995.
- M. A. Meyers, Dynamic Behavior of Materials (Wiley, New York, 1994), P.135.

- M.G.Shelyapina, D.Fruchart, E.K.Hlil, N.Skryabina, J.Tobola, P.Wolfers. First principles study of induced magnetic moments in $\text{Fe}_{1-x}\text{M}_x$ disordered alloys and in $\text{Fe/M}(001)$ superlattices with $\text{M}=\text{V}, \text{Nb}, \text{Ta}, \text{Mo}$. *J. Alloys & Comp.* V383 P157 2004.
- M.I.Katsnelson, M.Sigalas, A.V.trefilov & K.Y.Khromov. *Phil. Mag. B* V75 P407 1997.
- M.J.Forrestal and V.K.Luk, Dynamic spherical cavity-expansion in a compressible elastic-plastic solid. *J. Appl. Mech.* 55, 1-5 (1988).
- M.Korling and J.Haglund. *Phys Rev. B* V45 P13293 1992.
- M.L.Wilkins, Mechanics of penetration and perforation. *Int. J. Engng Sci.* 16(11), 793-807 (1978).
- M.Nakajima, K.Tokaji, H.Itoga and H.-N. KO. Morphology of step-wise S-N curves depending on work-hardened layer and humidity in a high-strength steel. *Fatigue & racture of Eng. Mat. & Struct.* V26 I12 P1113 2003.
- M.Sluiteer & Y.Kawazoe, *Mater.Trans. JIM* V42 P2201 2001.
- M.Sluiteer, D. De Fontaine, X.Q.Guo, R.Podloucky, & A.J.Freeman. *Phys. Rev. B.* V42 P10460 1990.
- M.Sluiteer, Y.Watanabe, D.De Fontaine & Y.Kawazoe. *Phys. Rev. B* V53 P6137 1996.
- Marx and Hutter, *NIC Series*, 2000, 1, 301-449.
- Millett, J.F.C., Bourne, N.K. & Rosenberg, Z. *J.APpl. Phys.* V81, P2579 1997.
- Monard, et al. *Acc. Chem. Res.* 1999, 32, 904.
- Montgomery, "Friction and wear at high sliding speeds", *Wear*, 36, pp. 275-298, 1976.
- N.D.Mermin, *Phys. Rev.* V137 A 1441 1965.
- N.I. Kulikov, D.Fristot, J.Jugel & A.V.Postnikov. Interrelation between structural ordering and magnetic properties in bcc Fe-Si alloys. *Phy. Rev. B* V66 P014206 2002.
- N.I.Kulikov, D.Fristot, A.Postnikov, J.Hugel. Influence of disorder on electronic structure and magnetic properties in Fe-rich Fe-Si alloys. *Computational Materials Science.* V17 P196 2000.
- N.Martensson. Substitutional disorder described within the supercell model. *J.Phys. F: Metal Phys.* V8 N1 P27 1978.
- Nasu, S., Sasaki, T., Kawakami, T., Tsutsui, T. & Endo, S. *J.Phys. Condense Matter* V14 P11167 2002.

- O.Gunnarsson & B.I.Lundqvist. Phys. Rev. Lett. V54 P1852 1985.
- O.K.Andersen. Phys. Rev. B V12 P3060 1975.
- O.N.Mryasov, A.I.Liechtenstein, L.M.Sandratskii & V.A.Gubanov. Magnetic structure of Fcc iron. J.Phys: Condens. Matter. V3 P7683 1991.
- Octahedral Sites. <https://www.tf.uni-kiel.de/matwis/amat>.
- P. Mahadevan & A. Zunger. Ferromagnetism in Mn-doped GaAs due to substitutional-interstitial complexes. Phy. Rev. B V68 P075202 2003.
- P.Bagno, O.Jepsen & O.Gunnarsson. Phys. Rev. B V40 P1997 1989.
- P.H.Pidsley, A numerical study of long rod impact onto a large target. J. Mech. Phys. Solids 32(4), 315-333 (1984).
- P.Mahadevan & A. Zunger. First principles investigation of the assumptions underlying model-Hamiltonian approaches to ferromagnetism of 3d impurities in III-V semiconductors. Phy. Rev. B V69 P115211 2004.
- P.Venezuela, G.M.Dalpian, Antonio J.R.da Silva & A.Fazzio. Ab initio determination of the atomistic structure of $\text{Si}_x\text{Ge}_{1-x}$ alloy. Phy Rev B. V64 P193202 2001.
- P.Venezuela, R.H.Miwa, A.Fazzio. Carbon in $\text{Si}_x\text{Ge}_{1-x}$: An ab initio investigation. Phy. Rev. B V69 P115209 2004.
- Park, Karpov and Liu.
- Punkkinen, J. Phy. Cond. Matt. 1999.
- Q.Lizhi & C.Wai-Yim. J.American Ceramic Soc. V84 N4 P801 2001.
- Qiang Hong, Tsung-han Lin. J.Phys.: Conde. Matter. P1867-1871 V1 1989.
- R. Alben, M. Blume, H.Krakauer & L.Schwartz. Phy Rev B V12 P4090 1975.
- R. Magri, J.E.Bernard & A. Zunger. Predicting structural energies of atomic lattices. Phy. Rev. B V43, P1593, 1991.
- R. McCormack & D.De Fontaine. First-principles study of multiple order-disorder transitions in Cd_2AgAu Heusler alloys. Phy. Rev. B. V54 N14 P9746 1996.
- R.Alben, M.Blume & M.Mckewon, *ibid.* V16 P3829 1977.
- R.C.Batra, Effect of nose shape and strain-hardening on steady state penetration of viscoplastic targets. In Computational Plasticity, Models, Software and Applications (edited by D.R. J. Owen, E.Hinton and E.Onate) 463-475, Pineridge Press, Swansea, U.K. (1987).

- R.E.Cohen & O.Gulseren. Phys. Rev. B V63 P2241 2001.
- R.G.Greene, H.Luo & A.L.Ruoff. Phys. Rev. Lett. V73 P2075 1994.
- R.H.Parmenter. Energy Levels of a Disordered Alloy. Phy. Rev. V97 N3 P587 1955.
- R.Hill, Cavitation and the influence of headshape in attack of thick targets by non-deforming projectiles. J. Mech. Phys. Solids 28, 249-263 (1980).
- R.J. Eichelberger and J.W. Gehring, Am. Rocket Soc. J. 32, 1583-1591 (1962).
- R.Soderlind, J.A.Moriarty & J.M.Wills, Phys. Rev.B. V53 P14063 1996.
- Ravid M., Bodner SR. Dynamic perforation of viscoplastic plate by rigid projectiles. Int. J. impact. Eng. 1983; 21(6): 577-91.
- Rick L. Martineau, Michael B. Prime & Thomas Duffey. Penetration of HSLA-100 steel with tungsten carbide spheres at striking velocities between 0.8 and 2.5km/s. Int. J. impact. Eng. V30 P505 2004.
- Ryoichi Kikuchi. A Theory of Cooperative Phenomena. Phy Rev. V81 P988, 1951.
- S S A Razee and R Prasad. Cluster Coherent-potential Approximation in the Tight-binding Linear-muffin-tin-orbital formalism. Phys. Rev. B V48 P1361 1993.
- S S A Razee and R Prasad. Configuration averaged Green's function within Korringa-Kohn-Rostoker coherent-potential approximation. Phy Rev. B V45 P3265 1992.
- S S A Razee and R Prasad. Disordered Alloys with Short-range Order: Korringa-Kohn-Rostoker Formulation within Cluster Coherent-Potential Approximation. Phys. Rev. B V48 P1349 1993.
- S S A Razee, A Mookerjee and R Prasad. On the analyticity of the cluster coherent potential approximation. J. Phys: Condens. Matter V3 P3301 1991.
- S S A Razee, S S Rajput, R Prasad & A Mookerjeel Electronic structure of Disordered alloys: Korringa-Kohn-Rostoker cluster coherent potential approximation. Phy. Rev. B V42 P9391 1990.
- S. Akber-Knutson, M.S.T.Bukowinski & J.Matas. Geophys. Research Letts V29 N3 P1034 2002.
- S. Muller & A. Zunger. First-Principles Predictions of Yet-Unobserved Ordered Structures in the Ag-Pd Phase Diagram. Phy Rev Lett. V87 P165502 2001.
- S. Muller & A. Zunger. Structure of ordered and disordered alpha-brass. Phy Rev B V63. P094204 2001.
- S. Stassis, Phys. Status Solidi A V64 P335 1981.

- S.A.Mullin, J.P.Riegel, III, D. A. Tenenbaum and D.W.Erdley, Dynamic plasticity modeling of conical and blunt nosed projectile and dual layer armor. 1991 TACOM combat Vehicle Survivability Symposium, Gaithersburg, MD, April 15-17 (1991).
- S.Baroni, S.De Gironcoli & A.Dal Corso. Rev. Mod. Phys. V73 P516 2001.
- S.Chocron, C.E.Anderson Jr., J.D. Walker, M.Ravid, A unified model for long-rod penetration in multiple metallic plates. Int. J. Impact Engng. Vol 28, 2003, 391-411.
- S.H.Wei, L.G.Ferreira, James E.Bernard & Alex Zunger, Electronic Properties of random alloys: Special quasirandom structures. Phy. Rev. B, V42 N15 P9622 1990.
- S.K.Bose, V.Drchal, J.Kudrnovsky, O.Jepsen & O.K.Andersen. Theoretical study of ordering in Fe-Al alloys based on a density-functional generalized-perturbation method. Phy Rev B. V55 N13 P8184 1997.
- S.K.Sikka & V.Vijayakumar. Phys. Rev. B. V38 P10926 1988.
- S.S.Kushwah & J.Shanker. Physica B: Condens. Matter V253 P90 1998.
- Savvateev, AF, Budin, AV, Kolikov, VA, and Rutberg, PhG. High-speed penetration into sand. Int. J. Impact Engng. 26 (2001), 675-681.
- Sergii Khmelevskiy & Peter Mohn. Critical behavior of disordered fcc Fe₇₀Pt₃₀ alloy under high pressure. Phy Rev B V68 P214412 2003.
- Shixun Zhou, Quantum Mechanics. Higher Education Press, 1997.
- Special-Purpose Nickel Alloys. ASM Specialty Handbook: Nickel, Cobalt and their Alloys. Product Code: 06178G. P92.
- T.Asada & K.Terakura. Phys. Rev. B. V46 P13599 1992.
- T.C.Leung, C.T.Chan & B.N.Harmon. Phys. Rev. B V44 P2923 1991.
- T.C.Schulthess, W.H.Butler, G.M.Stocks, S.Maat & G.J.Mankey. Noncollinear magnetism in substitutionally disordered face-centered-cubic FeMn. J.App. Phy. V85 N8 P4842 1999.
- T.P.Leevad Pedersen and A.N.Larsen, Appl. Phys. Lett. V75 P4085 1999
- T.Sasaki, A.M.Rappe & S.G.Louie. Phys. Rev. B V52 P12760 1995.
- T.W.Wright, A survey of penetration mechanics for long rods, in Computational Aspects of Penetration Mechanics (edited by J.Chandra and J.E.Flaherty), Lecture Notes in Engineering, 3, pp. 85-106. Springer-Verlag, Berlin-Heidelberg(1983).
- Tadmor, Phillips and Ortiz. Langmuir, 1996, 12, 4529.

- Taylor, R.D., Cort, G. & Willis, J.O. J. appl. Phys. V53 P8199 1982.
- Taylor, R.D., Pasternak, M. P. & Jeanloz, R.J. J.APpl. Phys. V69 P6126 1991.
- Tianci Jiang, Xia Lu, S. Hanagud, Time-Dependent Penetration Model for High-Velocity Impact & Penetration: Phase Transition Studies, 46th AIAA/ASME/ASCE/AHS/ASC Structures, Structural Dynamics and Materials Conference, 13th AIAA/ASME/AHS Adaptive Structures Conference, Austin, TX, April 2005.
- Tsunoda Y. J.Phys: Condens. Matter V1 P10427 1989.
- Tsunoda, Y., Nishioka, Y. & Nicklow, R.M. J. Magn. Mater. V128 P133 1993.
- U. Gonser, K.Krischel & S.Nasu. J.Magn.Magn.Mater.V15-18 P1145 1980.
- U.Gradmann & H.O.Isbert, J.Magn.Magn.mater.V15-18 P1109 1980.
- U.Gradmann, W.Kummerle & P.Tillmans. Thin Solid Films. V34 P249 1976.
- V. Blum & A. Zunger. Structural complexity in binary bcc ground states: The case of bcc Mo-Ta. Phys. Rev B V69 P020103 2004.
- V. Blum and A. Zunger. Mixed-basis cluster expansion for thermodynamics of bcc alloys. Phy. Rev. B V70 P155108 2004.
- V. Ozolins & A. Zunger. First-principles theory of the evolution of vibrational properties with long-range order in GaInP₂. Phy Rev B V57, R9404-R9407, 1998.
- V. Ozolins, C. Wolverton & A. Zunger. First-Principles theory of vibrational effects on the phase stability of Cu-Au compounds and alloys. Phy Rev B V58 R5897-R5900, 1998.
- V.Blum & A.Zunger. Prediction of ordered structures in the bcc binary systems of Mo, Nb, Ta and W from first-principles search of approximately 3,000,000 possible configurations. Phy. Rev. B V72 P020104 2005.
- V.Hohler and A.Stilp, Influence of the length-diameter ratio in the range from 1 to 32 on the penetration performance of rod projectiles. Proc. 8th Int. Symp. On Ballistics, pp. IB12-IB19. Orlando, FL, Oct 23-25(1984).
- V.L.Moruzzi, J.F.Janak & A.R.Williams. Calculated Electronic Properties of Metals. Pergamon, New York, 1978.
- V.M.Garcia-Suarez, C.M.Newman, C.J.Lambert, J.M.Pruneda & J.Ferrer. J.Phys: Condens.Matter V16 P5453 2004.
- V.Milman & M.C.Warren. J. Phys. Condens. Matter. V13 N24 P5585 2001.

- Vocadlo, L., Brodholt, J., Alfe, D., Gillan, D. & Price, G.D. Phys. Earth Planet. Inter. V117, P123 2000.
- W. J. Nellis, J. A. Moriarty, A. C. Mitchell, M. Ross & G. R. Dandrea. Phys. Rev. Lett. V60 P1414 1998.
- W. B. Pearson, A Handbook of Lattice Spacing and Structures of Metals and Alloys (Pergamon, Oxford, 1958).
- W. Keune, R. Halbauer, U. Gonser, J. Lauer & D. L. Williamson. J. Appl. Phys V48 P2976 1977.
- W. Kohn, L. J. Sham. Phys. Rev. A140 P1133 1965.
- W. Rehwald. Anomalous temperature dependence of the shear modulus C_{44} in nickel-iodine boracite. J. Phys. C: Solid State Phys. V11 P.L157 1978.
- Warshel and Levitt, J. Mol. Biol.
- WIKIPEDIA, [wikipedia.org/wiki/Alloy](http://en.wikipedia.org/wiki/Alloy). <http://en.wikipedia.org/wiki/Alloy>.
- WIKIPEDIA, [wikipedia.org/wiki/Iron](http://en.wikipedia.org/wiki/Iron). <http://en.wikipedia.org/wiki/Iron>.
- Williamson, D. L., Bukshpan, S. & Ingalls, R. Phys. Rev. B V6 P4194 1972.
- Wolfram Koch, Max C. Holthausen, A Chemist's guide to Density Functional Theory. Wiley-Vch, 2nd Edition, 2001
- X. Xu & W. Zhang, Theoretical Introduction to Equation of State. (Science Press, Beijing, 1986), P235.
- Xia Lu & S. Hanagud, Nonequilibrium Thermodynamic Models for the Dynamic Behavior of Polycrystalline Solids, Technical report, Georgia Institute of Technology, 2002.
- Xia Lu and S. Hanagud, First principle equation of state for an energetic intermetallic mixture, Editors: R Armstrong, n Thadhani, W Wilson, j Gilman, and R Simpson, 2003 MRS Fall Meeting: Symposium AA Synthesis, Characterization, and Properties of E Energetic/Reactive nanomaterials, Dec. 1-5, Boston, MA.
- Xia Lu and S. Hanagud, to be submitted Phys. Rev. letts.
- Xia Lu, Sathya V hanagud, Structural Phase Transitions and Equation of State of Aluminum from First-Principles. (In process).
- Y. J. Zhao & A. Zunger. Site preference for Mn substitution in spintronic $\text{CuM}^{\text{III}}\text{X}^{\text{VI}}_2$ chalcopyrite semiconductors. Phy. Rev B V69 P075208 2004.
- Y. Chen, T. Atago & T. Mohri, J. Phys: Condens. Matter V14 P1903 2002.

Yamasaki, J. Phy. Soc. Of Japan, 2003.

Z. Rosenberg, E.Marmor and M.Mayseless, On the hydrodynamic theory of long-rod penetration. Int. J. Impact Engng 10, 483-486 (1990).

VITA

Tianci Jiang received her Bachelor degree from Tsinghua University in Mechanics in July 1999, Beijing, China. After that, she came to the United States to pursue Ph.D. studies. She received her Master degree in Aerospace Engineering from Georgia Institute of Technology in December 2001. For personal reasons, she started co-operating with General Electric, Inc in August 2001. During two years full-time co-operating with General Electric, Inc, her dearest father passed away on November 4th 2002, which was a huge loss in her life. Her father had a cherished desire that Tianci be the third Ph.D. from Georgia Tech in the family, where her eldest brother Tianyue Jiang and elder brother Tianji Jiang received their Ph.D. from Georgia Tech in Aerospace Engineering (1998) and in Computer Science (2000), respectively. To fulfill her father's will, from the spring of the year 2003, she began preparations to pursue her Ph.D. degree in Aerospace Engineering at Georgia Tech.

She re-enrolled in Georgia Tech in August 2003. Simultaneously she continued working in General Electric, Inc. With great financial and moral support from the entire GTAE group and Aerospace Engineering department, she was greatly encouraged, cherishing this study opportunity very much. She is very diligent in her GE work and Ph.D. study. With a tight schedule, eight months later, in April 2004, she successfully passed the qualification exam and became a Ph.D. candidate. From May 2004, without affecting GE work, under direction of her advisors, she utilized night hours and weekends to do outstanding Ph.D. research. During this time, she accepted a position with General

Electric, Inc. as a gas turbine application engineer. In December 2005, after one and half years, she successfully defended her Ph.D. thesis.